

A Stochastic Method for Automated Matching of Horizons across a Fault in 3D Seismic Data

Dissertation

zur Erlangung des akademischen Grades

Doktoringenieur (Dr.-Ing.)

angenommen durch die Fakultät für Informatik
der Otto-von-Guericke-Universität Magdeburg
von

M. Sc. Fitsum Admasu

geboren am 7.Mai 1978 in Dilla.

Gutachter: Prof. Dr. Klaus Tönnies
Prof. Dr. Peter Kukla
Prof. Dr. Hans du Buf

Ort und Datum des Promotionskolloquiums:
Magdeburg, 10. März 2008.

Abstract

ADMASU, FITSUM. A Stochastic Method for Automated Matching of Horizons across a Fault in 3D Seismic Data.

Seismic data are pictures showing subsurface seismic reflectivity. Seismic data interpretations concern with building geological models with the aim to describe relationship between the seismic data and a priori geological information. The models are used for hydrocarbon exploration or other geotechnical investigations.

This thesis work is motivated by a demand of computer-assisted interpretation of seismic data. Manual interpretations take too long and are almost always non-unique. The computer-assisted interpretation has advantages in that it provides a faster interpretation framework and a consistent workflow.

This thesis focuses on automating horizon matching across a fault surface. Horizons are visible boundaries between certain sediment layers in seismic data. Faults are discontinuity surfaces across which horizons are cut and displaced. Automation tools, such as auto-trackers, are widely being used to assist horizon interpretation. However, they fall short of tracking horizons across faults. Horizon matching across faults is done after defining the fault surface, and it is about establishing the pre-fault geological continuity of horizons. In order to define the fault surface, a new semi-automatic fault-tracking method has been developed. It involves fault enhancing through the use of a log-Gabor filter followed by fault tracking based on an active contour model.

The thesis proposes a new Bayesian-based fully automated method for horizon matching across a fault. The new method exploits the existing 3D spatial information and the multi-resolution nature of sediment layer structures in seismic images. A stochastic model has been defined under a marked point process framework. It models spatial data correlations and geological continuity constraints about sediment layers. The optimal matching solution has been found as a parameter which maximizes the stochastic model conditioned on seismic data. This is done by using a multi-resolution stochastic annealing algorithm.

Application of the proposed method is compared with real 3D seismic data interpretations. Tests were made for 20 different fault patches taken from 4 seismic data sets. Automated matching results on 16 faults were considered acceptable after comparing them with references obtained manually. The method works well for planar faults and relies on the correct definition of horizon geometries. Additional tests show that the new method is more robust than previous methods while providing coarse-fine scale horizon matching.

Abstract - deutsche Fassung

ADMASU, FITSUM. A Stochastic Method for Automated Matching of Horizons across a Fault in 3D Seismic Data.

Seismische Daten zeigen seismische Reflektionen unter der Erdoberfläche. Bei der Interpretation dieser Daten versucht man, Modelle zu konstruieren, die die Beziehung zwischen den gemessenen Daten und den schon zuvor bekannten geologischen Informationen beschreibt. Diese Modelle können dann für Kohlenwasserstoff-Untersuchungen oder andere geotechnische Erkundungen genutzt werden.

Diese Arbeit wird durch die Nachfrage nach computergestützter Interpretation seismischer Daten motiviert. Eine manuelle Interpretation der Daten ist oft zeitaufwendig und nicht eindeutig. Die Vorteile computergestützter Verfahren sind daher die schnellere Berechnung und ein konsistenter Arbeitsablauf.

Der Schwerpunkt dieser Arbeit ist die automatische Zuordnung von Erdschichten zu geologischen Bruchstellen. Erdschichten sind sichtbare Grenzen zwischen bestimmten Sedimentschichten in seismischen Daten, während Bruchstellen Diskontinuitätsflächen sind, an denen die Erdschichten gegeneinander verschoben werden. Automatische Werkzeuge wie etwa Auto-Tracker werden häufig bei der Interpretation von Erdschichten genutzt. Sie sind jedoch unzureichend, wenn es um die Verfolgung der Erdschichten über Bruchstellen hinaus geht. In diesem Fall ist es notwendig, die Fläche des Bruches genau zu definieren und die geologischen Zusammenhänge der Erdschichten vor dem Bruch zu ermitteln. In dieser Arbeit wird ein semi-automatischer Tracking-Ansatz benutzt, um Bruchstellen zu bestimmen. Dieser besteht aus einer Hervorhebung der Brüche und einer anschließenden modell-basierten Verfolgung.

In dieser Arbeit wird eine vollautomatische Methode für die Zuordnung von Erdschichten über Bruchstellen hinweg vorgestellt. Ziel ist es, ein robustes Werkzeug zur Verfügung zu stellen, das die räumlichen Informationen in den dreidimensionalen seismischen Daten nutzt. Die Methode nutzt ein Marked-Point-Prozess Framework. Ein Point-Prozess ist dabei über eine Menge einander zugeordneter Punkte definiert. Dieser Marked-Point-Prozess nutzt einen Energieterm, der sowohl grundlegend seismische Informationen der Szene als auch geologisches Wissen berücksichtigt. Optimale Lösungen werden mittels eines stochastischen Annealing-Algorithmus auf mehreren Auflösungsstufen gefunden.

Die Anwendung der vorgestellten Methode wird mit einer realen Interpretation der seismischen Daten in 3D verglichen. Es wurden Tests für 20 verschiedene Ausschnitte aus vier Datensätzen durchgeführt. Die Ergebnisse des automatischen Prozesses wurden in 16 Fällen als akzeptabel bewertet. Die Methode liefert gute Ergebnisse bei ebenen Brüchen und ist abhängig von einer korrekten Definition der Geometrie der Erdschichten. Zusätzliche Tests zeigen, dass die neue Methode robuster als zuvor vorgestellte Methoden ist. Ferner bietet sie eine grob-zu-fein Zuordnung von Erdschichten.

Acknowledgments

The author wishes to express his gratefulness to his supervisor Professor Klaus Tönnies for giving him the opportunity to do the research in this field and for his support during the writing. The author also likes to thank Professor Hans du Buf and Professor Peter Kukla for taking the time to review the thesis.

Special thanks to Dr. Stefan Back, for his expertise advices regarding geology and seismic interpretation, and to Phili Heron, for proofreading and correcting English errors.

The author would like to thank the Voice team at Rijswijk SHELL Research Center for stimulating discussions and providing seismic data.

The author would also like to express his gratefulness to Petra Specht for her continuous help during his stay in Magdeburg. Finally, the author extends his appreciations for Anduaem Dame-tew for his enormous help during the thesis submission.

Contents

List of Figures	V
List of Tables	VII
1 Introduction	1
1.1 Background	1
1.1.1 Seismic Imaging	1
1.1.2 Structural Interpretation of Seismic Images	1
1.2 Motivation	3
1.3 Scope of the Thesis	4
1.4 Thesis Outline	6
2 Geological Concept	9
2.1 Sedimentary Rock Layers	9
2.2 Faults	9
2.3 Geological Imaging of the Subsurface	13
2.4 Concluding Remarks	13
3 Seismic Imaging	15
3.1 Seismic Reflection	15
3.2 Seismic Acquisition	17
3.3 Seismic Data Processing	20
3.4 Structural Interpretation of Seismic Data	22
3.4.1 Fault Interpretation	23
3.4.2 Horizon Interpretation	25
3.4.3 Horizon Matching across Faults	26
3.5 Concluding Remarks	26
4 Research Issues of Seismic Data Analysis	27
4.1 Improving Data Quality	27

4.2	Data Enhancing	28
4.3	Automation	29
4.4	Previous Methods for Automated Horizon Matching across Faults	30
4.5	Concluding Remarks	31
5	Auto-tracking of Faults	33
5.1	Scope and Assumptions	33
5.2	Fault Highlighting	34
5.3	Fault Tracking	37
5.4	Results	42
5.5	Discussion	44
5.6	Conclusions	45
6	Automated Horizon Matching: Matching Model	47
6.1	Scope and Assumption	47
6.2	Knowledge Base to Match Horizons across Faults	50
6.3	Representations	51
6.4	Horizon Matching as Marked Point Process	52
6.4.1	Marked Point Process	53
6.4.2	Marked Point Process of Horizon Pairs	53
6.4.3	Fault Throw Energy, $S(m)$	55
6.4.4	Seismic Energy, $A(m)$	57
6.5	Optimal Matching Solution	62
6.6	Concluding Remarks	62
7	Automated Horizon Matching: Solution Searching	63
7.1	Global Search Optimization Methods	63
7.2	Stochastic Annealing	63
7.2.1	Acceleration of Convergence	66
7.2.2	Multi-resolution Representation and Search	67
7.3	Concluding Remarks	71
8	Automated Horizon Matching: Validations	73
8.1	Experimental Setup	73
8.1.1	Experimental Workflow	73
8.1.2	Test Data	75
8.1.3	Solution Definition	75

Contents	III
8.2 Parameter Estimations	81
8.3 Results and Discussions	88
8.3.1 Performance of Automated Horizon Matching across a Fault	88
8.3.2 Impact of considering 3D Spatial Relationship	93
8.3.3 Impacts of the Multi-resolution Search	95
8.3.4 Comparisons with Previous Methods	99
8.4 Concluding Remarks	103
8.4.1 Future Work	105
9 Conclusions	107
A Extension to Experiment Setup	111
A.1 Data Loading and Display	111
A.2 Fault Tracking and Fault Patch Extraction	111
A.3 Horizon Tracking and Features Computations	112
A.4 Horizon Matching	112
Bibliography	117

List of Figures

1.1	Example of 3D seismic data	2
1.2	Snapshot of interpreted inline seismic slice	3
1.3	Horizon matchings on a 2D inline slice.	5
2.1	Horizon configuration	10
2.2	Fault types.	11
2.3	Elliptical fault displacement model	12
3.1	Seismic ray path theory.	16
3.2	Snell's law.	17
3.3	Seismic data acquisition principle	18
3.4	Seismic acquisition geometry.	19
3.5	Seismic reflections.	20
3.6	Seismic processing.	21
3.7	Seismic migration.	22
3.8	Seismic stacking.	22
3.9	Seismic cube.	23
3.10	Seismic data preview.	24
3.11	Seismic coherency.	25
5.1	Gabor function	35
5.2	Log-Gabor Filter modulus and phase.	37
5.3	Modulus of log-Gabor filter.	38
5.4	Automated fault-tracking workflow.	41
5.5	Example of the sequential auto-tracking of a large-scale fault.	43
6.1	Fault patch.	48
6.2	Horizon tracking procedure.	49
6.3	Horizon tracking results.	49
6.4	Horizon matching as point process.	54

6.5	Fault throw attribute computation.	56
6.6	Seismic attribute computation.	59
6.7	Top view of seismic attribute.	60
6.8	Seismic similarity measure.	61
7.1	Birth and death moves.	65
7.2	Horizons do not cross each other.	67
7.3	Wavelet decomposition	69
7.4	Multi-resolution representation of horizons.	70
8.1	Workflow for automated horizons matching across a fault.	74
8.2	Preview of inline slices.	77
8.3	Preview of inline slices.	78
8.4	Preview of inline slices with seed fault lines.	79
8.5	Preview of inline slices with fault patch regions.	80
8.6	Fault model parameter estimations.	86
8.7	Stochastic annealing run.	87
8.8	Automated matching results.	90
8.9	Automated matching results.	91
8.10	Automated matching results.	92
8.11	Automated matching results.	93
8.12	Automated matching results.	94
8.13	Automated matching results.	97
8.14	Automated matching results.	98
8.15	Automated matching results.	100
8.16	Automated matching results.	101
8.17	Automated matching results.	102
A.1	Prototype software GUI interface for data loading.	113
A.2	Prototype software GUI interface for fault tracking.	114
A.3	Prototype software GUI interface for horizon tracking.	115
A.4	Prototype software GUI interface for horizon matching.	116

List of Tables

8.1	Characteristics of test data sets.	75
8.2	List of test fault patches.	76
8.3	Distance from the fault surface to compute attributes.	82
8.4	Summary of setting rules for energy parameters and the normalization constant.	84
8.5	Tuning rules for stochastic annealing parameters.	85
8.6	Automated matching results.	89
8.7	Single- and multi-resolution automated matching results.	96

1 Introduction

1.1 Background

1.1.1 Seismic Imaging

Seismic data produce images of subsurface structure by reflecting seismic waves off rock layers. By recording reflection time and amplitude of these waves, hypotheses about depth and properties of the boundaries between rock layers can be developed. This is important because drilling of wells is expensive. Seismic imaging methods of deep hydrocarbon accumulation are therefore economically mandatory.

Three-dimensional (3D) seismic data consist of numerous closely-spaced seismic lines that provide a high spatially sampled measure of subsurface reflectivity (Figure 1.1). It has dimensions of inline, cross-line and time. Its inline dimension is parallel to the direction in which the data were acquired while its cross-line dimension is perpendicular to the data acquisition direction. The time dimension represents depth of the imaged subsurface structures. It is measured in Two Way Travel (TWT) time unit. TWT is the time spent when the signals sent from the surface go down and return. Usually, time sampling in 2ms is done for the duration of 6 seconds resulting in approximately 3000 time slices. Seismic data resolution (bin spacing) ranges from 12.5 m to 25 m [59].

1.1.2 Structural Interpretation of Seismic Images

Seismic data is analyzed in order to produce a model of the (unseen) subsurface. The analysis (or the interpretation) encompasses different stages where underground rock layer properties are identified. The analysis results are crucial for underground prospect evaluation and influence the subsequent economic viability.

Structural interpretation of seismic images aims at extracting quantitative information. It builds a geometric structural framework that is used to constrain the subsurface. It involves the in-

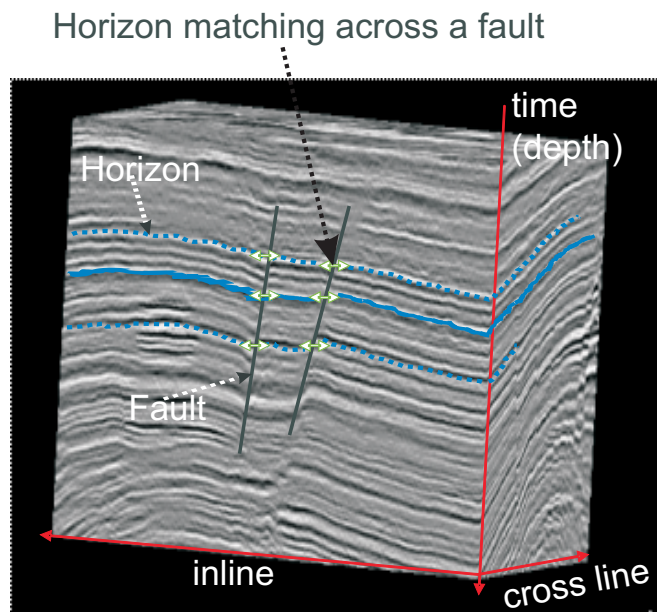


Figure 1.1: 3D seismic data with manually interpreted faults and horizon.

interpretation of horizons and faults. Horizons are characterized by strong reflections indicating large differences between rock layers. They are interpreted from seismic slices by following trends of similar seismic events such as peaks or troughs [53] (Figure 1.1). Faults are fractures across which there is a measurable displacement of rock layers. They are recognized by horizon discontinuities and usually interpreted as straight lines or connected line segments (see interpreted fault lines on Figure 1.1). Jump correlations (or matchings) of horizons across faults are attempted after identifying the fault lines.

The interpretation of the 3D seismic data still heavily depends on human interpretation capabilities. The manual interpretation is generally performed on 2D seismic slices and the interpreters move across sequences of slices in different directions to evaluate their interpretation. Figure 1.2 shows a manually interpreted seismic inline slice. In this figure, horizons which have been disconnected by a fault are matched. The 3D nature of the data set can only be appreciated if a sequence of slices is displayed. This is done frequently as the information from a single slice is often inconclusive. Many fault lines exist even on a single seismic slice, and a typical seismic survey may have thousands of slices. Therefore, performing matchings of horizons across every fault line is very time-consuming and prone to error.

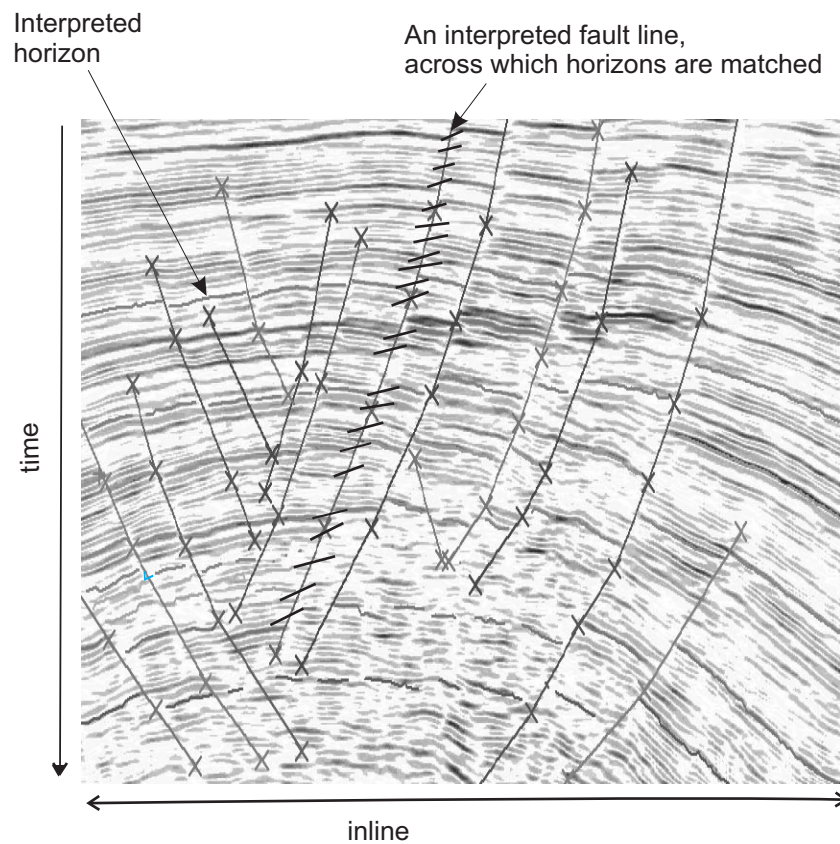


Figure 1.2: Kingdom Suite [91] snapshot showing manually interpreted seismic inline slice.

1.2 Motivation

The work of this thesis is motivated by the demands of computer-assisted interpretation of seismic data. At present most parts of seismic interpretation are done manually and require several interpretation cycles [83]. The sky-rocketing prices of oil and impending shortage require exploration in areas that were once avoided for technical reasons. Seismic surveys are being conducted on previously exploited areas in order to look for additional reservoirs. The area covered by a survey has grown and the sample density has become larger. Data sets can now be several hundred gigabytes in size, which means that it takes too long to build trusted models for reaching exploration decisions.

Since the true structures cannot be ascertained using solely seismic observations, a good interpretation is a consistent interpretation which is reasonable enough with a priori geological knowledge [156] [155]. Manual interpretations are always biased [121] [17] [155] and lack well specified reliability measures.

The computer-assisted interpretation has the advantage that it provides a faster interpretation framework and imposes a consistent work-flow. Its quantitative nature provides a repeatable data analysis tool and shows ways for continuously improving interpretation models. Existing three-dimensional spatial relationships in the data (such as continuity) may be directly exploited, whereas humans are only able to evaluate them from 2D projections or 2D slices of the data.

This thesis investigates image analysis tools to automate the structural interpretation of seismic data. Since the 1980s computer image analysis has evolved greatly and the application areas have widened to incorporate medicine [117][82] [86] [10], microscopy [90], remote sensing [94], astronomy [130], defense [62], manufacturing [71], robotics [92], and underwater navigation [127]. Each of these application areas has spawned separate subfields of digital image analysis, with a large collection of specialized algorithms and concepts. The demands for better image analysis methods are rising through advanced imaging technologies producing higher resolution spatial images. One of the current research directions is towards 3D structure representation in data.

1.3 Scope of the Thesis

This thesis deals with the problem of automating the task of horizon matching across faults in 3D seismic data. The scope of the horizon matching is restricted to a single fault patch. The fault patch is a subvolume of 3D seismic data and contains a fault surface together with uninterrupted seismic sections. It is also assumed that horizon geometries are defined within the seismic sections. The matching is restricted to the common normal fault, where one side of the fault block (hanging wall) moves down relative to the other (footwall). The automation problem is defined as the task to gather seismic features on the two sides of a fault and to find an optimal match between them. Figure 1.3 illustrates a schematic normal fault configuration and expressions of the matching problem on 2D seismic slices.

Within the fault patch, the fault surface is described through a set of coordinates in 3D. There are no readily available tools to define faults in 3D seismic data, and automated fault surface definition is still an active research area. The thesis presents a semi-automated method for tracking faults. The method consists of fault highlighting followed by a model-based fault tracking. The model-based approach provides a means for incorporating a priori knowledge about faults such as the orientation and plane-like geometry. The semi-automatic aspect utilizes judgements of the interpreters in areas of low signal to noise ratio.

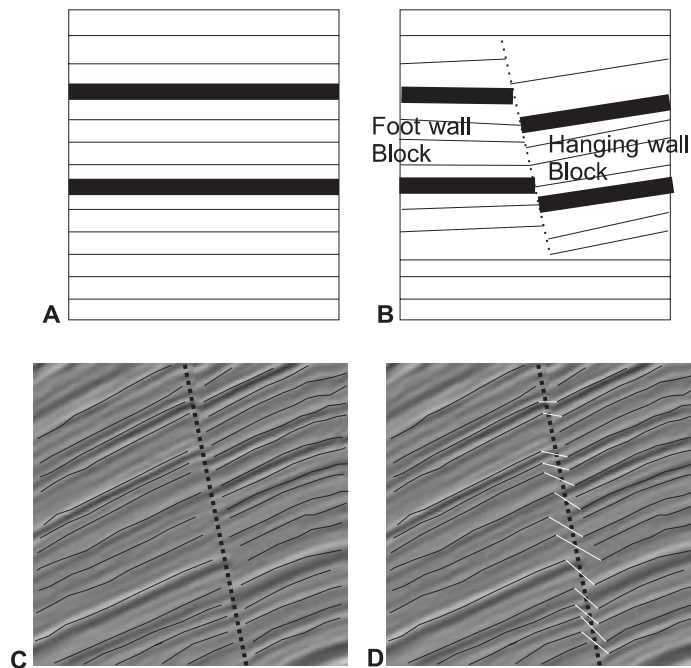


Figure 1.3: A. schematic representation of pre-fault configuration of rock layers. B. schematic representation of post-fault (normal fault) configuration of rock layers. C. seismic inline slice with manually interpreted horizon (black) curves. The dashed line indicates the normal fault which cuts and displaces the horizons. Only a single slice selected from 3D seismic data is shown. D. seismic inline slice from C but with horizons matched (using the white lines) across the fault.

Horizon definition in un-faulted regions is comparatively well automated with auto-tracker tools commercially available [53]. However, automated horizon matching across faults is still very challenging because of non-dense seismic information, local distortions, and the large number of possible solutions. Post-fault configurations imaged by the seismic data do not provide the complete information about the pre-fault configuration of horizons. Scale differences of horizons across the fault are expected, and some horizons on one side may not have matches on the other side of the fault. Matches are made with the aim to close the gap between observed data and to a prior geological knowledge. This thesis investigates a model-based approach for automated horizon matchings across faults, and the major research questions addressed are:

1. What are the relevant image features and prior geological knowledge for horizon matching? How can they be modeled for the automation task?
2. How can intensity and geometry features be computed?
3. How can the matching solution be represented? What is an optimal solution?
4. How can the optimal solution be searched?

The thesis aims to exploit the existing 3D spatial information for robust data analysis. The extension is not a mere adding of dimension to 2D methods [14], a new stochastic horizon matching model, which integrates data terms and prior geological constraints, is introduced. The data term incorporates seismic observations through statistical measures of local homogeneities in 3D space. The geological constraints are incorporated as statistical a priori model for capturing what is expected before data are seen. The stochastic nature of the model provides quality measures and sampling means to find the optimal matching solution.

Matching solutions are searched in multi-resolution fashion where results from ‘strong’ horizons give guidance to match ‘weaker’ horizons. This expects to increase the efficiency as well as the effectiveness of the matching. The terms ‘strong’ and ‘weaker’ are defined in a new semantic scale-space.

The hypothesis imposes the following additional questions:

1. How can 3D image features be represented?
2. How can multi-resolution up-scaling and down-scaling be decided ?
3. What are the impacts of the features for a successful matching decision?
 - a) What is the impact of considering 3D information?
 - b) What is the influence of the multi-resolution matching approach?

Answers to these research questions are made throughout the thesis. Prototype software is also implemented to show the applicability of the matching method.

1.4 Thesis Outline

All in all this thesis has 9 chapters.

Chapter 2 introduces basic geological concepts aiming to provide the foundation to understand the major tools introduced and to follow the argumentations.

Chapter 3 explains the seismic reflection method and the manual procedure of seismic interpretation.

Chapter 4 sets up the rationale for the new method with regard to research issues of the seismic data analysis and reviews related to research works.

Chapter 5 presents a semi-automatic fault tracking method for 3D seismic data and documents auto-interpretation results achieved on a 3D seismic volume.

Chapter 6 and 7 present the algorithm for performing horizon matchings across faults in seismic data. Chapter 6 introduces the stochastic horizon matching model of the algorithm, while Chapter 7 describes the search strategy to find the optimal matching solution.

Chapter 8 compiles and interprets the results that have been gathered from the application of the matching method.

Finally, Chapter 9 presents the conclusions detailing the major contributions of the thesis.

2 Geological Concept

This chapter gives basic introductions to the necessary geological concepts. In the first two sections, concepts of sedimentary rocks and faults are introduced. Emphasis is placed on their geometrical definition rather than their lithological properties. In the third section, different geological imaging techniques to study the subsurface are listed. Concluding remarks are given at the transition to the next chapter.

2.1 Sedimentary Rock Layers

Sedimentary rocks are the most studied rock types. Amongst others, they are of economic interest, as a source and reservoir for hydrocarbons.

These rocks are formed by long-time depositional processes. The depositional process produces layered geometric configurations where the oldest and the youngest layers are in most circumstances respectively found at the deepest and the shallowest locations. Due to the nature of depositional processes the layers are more homogenous horizontally than vertically. As the sedimentary package thickens, the pressure exerted on layered sedimentary rocks also increases. The pressure changes are reflected in changes of the rock density, porosity, permeability and acoustic impedance. Ideally, the rock layers have parallel to subparallel geometric configurations. However, in reality, the configurations are quite complex evolving from various geological events such as non-uniform deposition, erosion, and faulting. Thus, the subsurface configuration often shows a bent, broken up, and rotated configuration [125] (Figure 2.1). Sedimentary rock layers at the surface often provide detailed information about subsurface geometries.

2.2 Faults

Faulting is the most common deformation event affecting layered rocks. The faulting process creates a surface along which one side of rock layers has moved relative to the other side in a

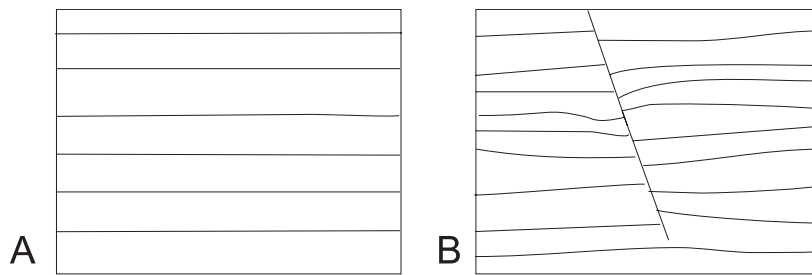


Figure 2.1: Horizon configuration A. Ideal B. Complex. Modified from [125].

direction parallel to the surface. The fault block that has moved is called the hanging wall, while the fault block that stays is called the footwall.

Depending on the relative direction of displacement between the rocks on either side of the fault surface, faults are classified as normal, reverse or strike-slip [175]. A normal fault drops the rock on one side of the fault down relative to the other side while in a reverse fault, one rock block is pushed up relative to the rock on the other side. The rock blocks on either side of strike-slip faults, on the other hand, slide along side-by-side. Figure 2.2 illustrates the different fault types.

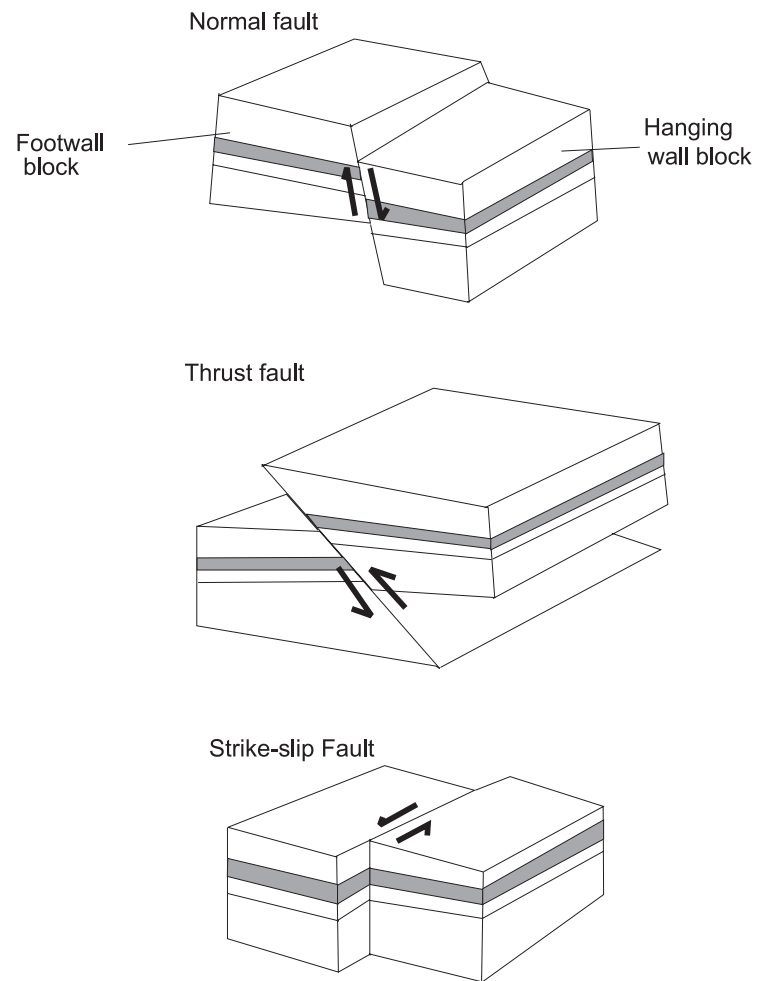


Figure 2.2: Fault types.

Many studies have been conducted in the past in order to find the relationship between rock displacements and a fault geometry. A fault displacement is the offset of segments or points that were once continuous or adjacent. A relation $D \propto L^c$ for $1 \leq c \leq 2$ between maximum displacement D and fault length L has been reported in many geological studies (for example, [47], [51], [182], [181]). The vertical component of a fault displacement is called fault throw. A fault throw profile on a fault trace reaches its maximum typically near the center point of the trace and decreases to zero towards the tips (Figure 2.3).

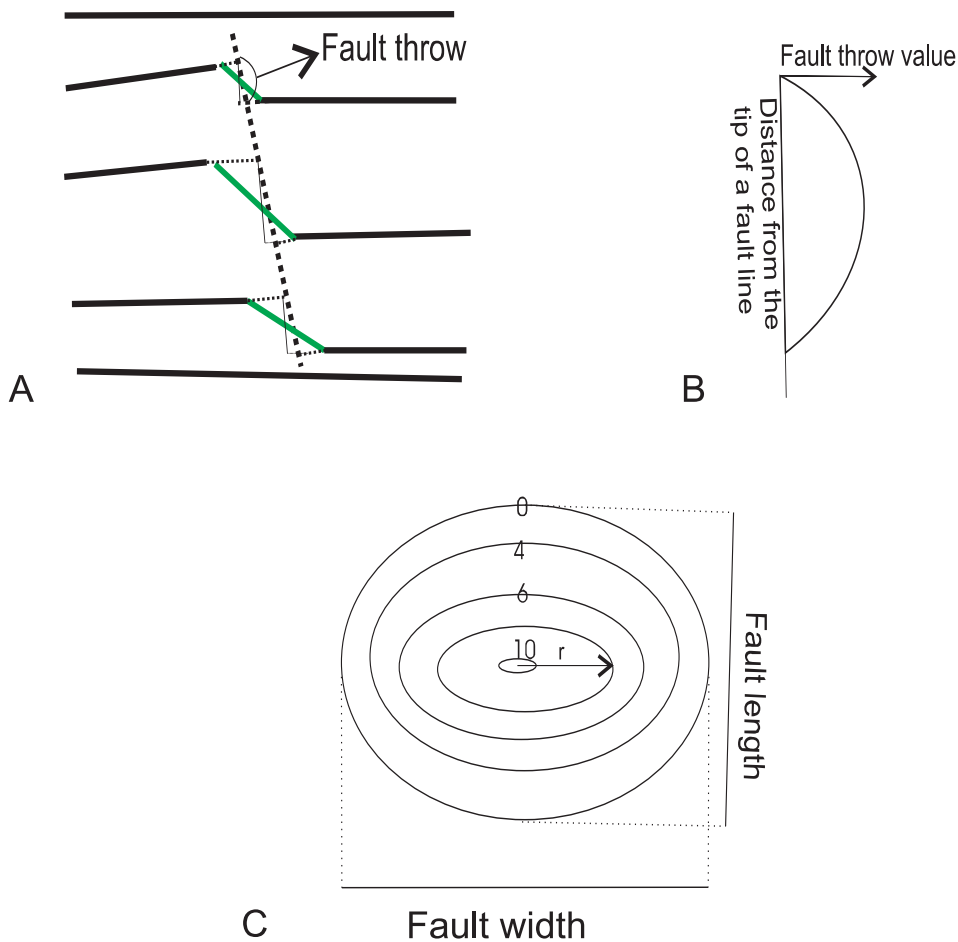


Figure 2.3: Schematic representation of fault patterns. A. Shows the faulted rocks. Interfaces between rocks are indicated by black line segments and connections across the dashed fault indicate the continuations after the faulting. B. 1D ideal fault throw profile on fault line. C. 2D ideal fault throw profile on a fault surface. The concentric ellipses are fault throw contours (according to [181]).

Faults generally affect fluid mobility in the reservoir. They act as seals or conduits of fluids by deforming and juxtaposing rock layers. Therefore, the understanding of faults and related structures is very important in many cases.

2.3 Geological Imaging of the Subsurface

Subsurface imaging is conducted in various ways and forms. However, the most detailed and indispensable way for hydrocarbon exploration is seismic imaging. Seismic imaging is applied at or near the earth's surface to measure the elastic properties of the subsurface and to detect variations in those properties. The detected variations appear in seismic data and are used to create a hypothesis about underground rocks or fluids. It is capable of picturing as deep as ten kilometers and spatially resolving features at scales as small as tens of meters [149] [59].

Well data also provide an imaging of the subsurface at a smaller range. They are collected by drilling a well and measuring the rock properties at different depths.

2.4 Concluding Remarks

In this chapter, the application background of the thesis has been introduced. Sedimentary rocks have distinct characteristics resulting from different rock and fluid properties. Faults are explained as surfaces along which rock layers are displaced. Since they influence the path of subsurface fluid flow, an understanding of their geometry and displacement profile is important. Seismic imaging provides the most detailed image of a subsurface and is widely used. The next chapter discusses details of seismic imaging.

3 Seismic Imaging

This chapter starts with the basic theory of the seismic reflection method, and describes current techniques of seismic data acquisition, processing and interpretation. Detailed discussions are given for the structural interpretation, since it is the scope of the thesis.

3.1 Seismic Reflection

The theory of seismic wave propagation is the basis for seismic imaging. Seismic waves are generated when a stress is applied near or at the earth's surface. The generated seismic waves propagate in all directions from the stress source, and they are governed by the mechanical properties of the rocks, such as incompressibility, rigidity, and density. Wave characteristics are also affected by the layering of the rocks and physical properties of the surface soil.

The seismic reflection method deals with seismic waves that propagate through the earth's interior. Seismic waves are divided into: compressional (P-) waves and shear (S-) waves. Compressional waves propagate by moving the particles in the medium parallel to the propagation direction while shear waves propagate by moving the medium particles perpendicular to the propagation direction. The thesis deals exclusively with seismic data acquired by using P-waves, thus subsequent explanations are only given for P-waves.

The velocity of the seismic ray is described as a function of the elasticity of the medium in which the ray is travelling. Any medium that can support wave propagation may be described as having an impedance. Mathematically, the velocity V_p of a P-wave travelling through a homogeneous and isotropic medium is given by

$$V_p = \sqrt{\frac{(\frac{4}{3})\mu + K}{\rho}} \quad (3.1)$$

where μ is the shear modulus, K is the bulk modulus and ρ is the density of the medium [184]. The shear modulus is proportional to the shear strength of the medium, while the bulk modulus

describes the incompressibility of the medium. Then, the impedance Z of a medium is defined as

$$Z = \frac{K}{V_p}. \quad (3.2)$$

A propagating seismic wave is understood by using principles from optics:

- . Fermat's principle: a seismic ray travels along the shortest possible path between two points (Figure 3.1A).
- . Huygen's principle: each point on a wave front (a seismic wave front is a constant phase surface) produces secondary spherical waves (called wavelets). After time t the spherical radius of each is $V * t$ (Figure 3.1B).

These principles help to locate a wave front after a certain time interval.

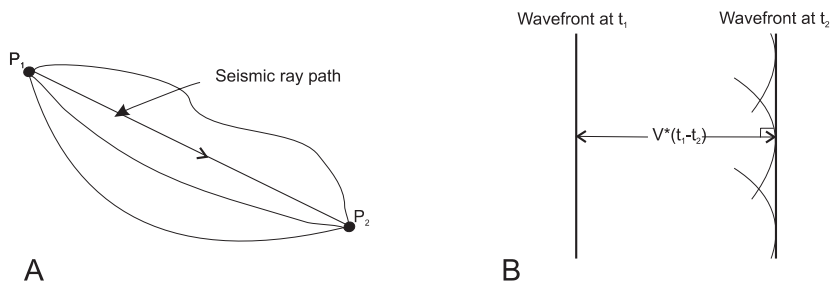


Figure 3.1: A. shows Fermat's principle. A seismic ray travels along the shortest possible path between two points. B. presents Huygen's principle. Each point on a wave front produces secondary spherical waves. After time t the spherical radius of each wave front is $V * t$.

A change in velocity while a wave traverses through different media results in reflection and refraction (Figure 3.2). These events are governed by Snell's reflection and refraction laws.

- . The law of reflection states that the angle of reflection equals the angle of incidence.
- . The law of refraction relates velocity to the angle of incidence and to the angle of refraction,

$$\frac{\sin(i)}{\sin(r)} = \frac{V_i}{V_r}. \quad (3.3)$$

where i and r are angles of incidence and refraction respectively. V_i and V_r are seismic wave velocities respectively in rock layers where the incidence and the refracted wave front passes.

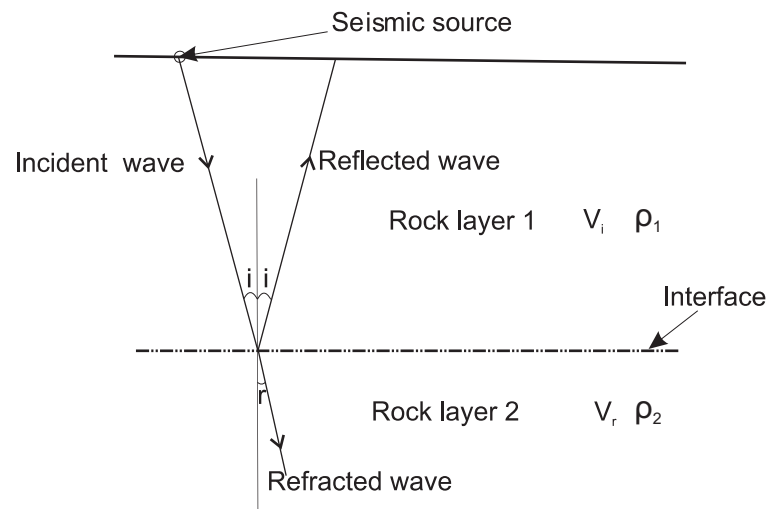


Figure 3.2: Snell's law. Reflection and refraction occurs when a seismic wave passes through two media having different acoustic impedance. The angle of reflection is the same as the angle of incidence, while the angle of refraction is related to the angle of incidence through Snell's law.

In the seismic imaging theory, the subsurface geology is viewed as a stack of homogeneous rock layers with planar upper and lower surfaces. Each homogeneous layer supports wave propagation with different impedances. Seismic waves are generated from sources put on the surface, and structures are estimated by using travel times of seismic waves which get reflected at the boundaries between the layers. The reflections are recorded by recorder instruments put on the earth's surface close to the sources. After the recorder measured the precise arrival time of the wave, its velocity is calculated and used to determine the properties of the rock layer in which it travels. Details of the seismic imaging theory are found in [155]. For details of the seismic wave propagation refer to [11] [40] [173]. Figure 3.3 illustrates a seismic data acquisition principle.

3.2 Seismic Acquisition

The essential features of seismic data acquisition are [149]:

- Sources of seismic energy
- Illumination of a subsurface target area with downward propagating waves
- Reflection and refraction of the seismic waves by subsurface heterogeneities
- Detection of the reflected seismic energy on recorders on the earth's surface.

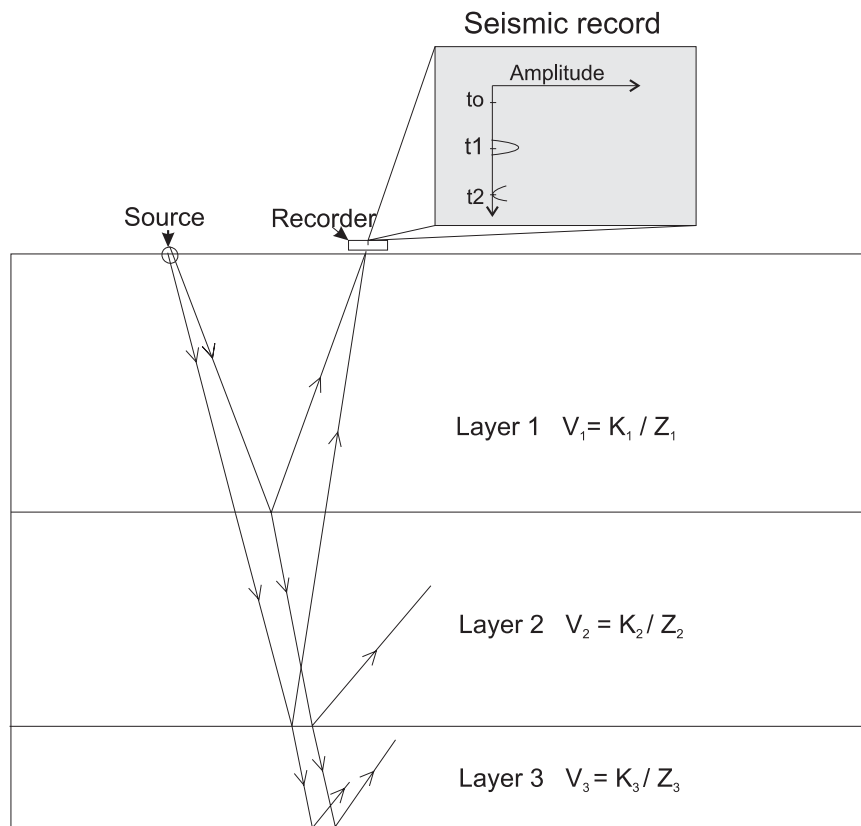


Figure 3.3: Schematic representation of seismic data acquisition principle. A seismic wave originated from a source gets reflected and refracted while going down. The amplitude and the arrival time of the reflected waves are recorded by recorder put on the surface.

Geophones are used as recorders on land, and work by measuring the motion of a magnet hanged on a coil attached to a base implanted in the earth. This motion produces a voltage which is proportional to the movement of the surface. For marine work, hydrophones are used to sense the instantaneous pressure in the water due to the seismic waves.

Seismic sources come in different shapes and sizes. Sources such as dynamite, vibrioses, weight drop, large caliber guns and vibrators are used on land, while vibrator, air guns, electric sparkers and confined propane-oxygen explosions are the most common sources for a marine survey [149].

For surveys related to the exploration of oil and gas, several sources and receivers are placed close to each other in order to illuminate the subsurface significantly. Their arrangement is guided by geometric and signal processing rules. The typical distance between the sources is 50-100 meters (m) and the distances between sources and recorders are within the range of 25 m [153]. Figure 3.4 shows an example of seismic acquisition geometry. In this figure, the recorders

are put in stations with separation of 3 m. The distance of the first recorder from a shot source is 15 m. Additional acquisition geometries are discussed in [26] [44].

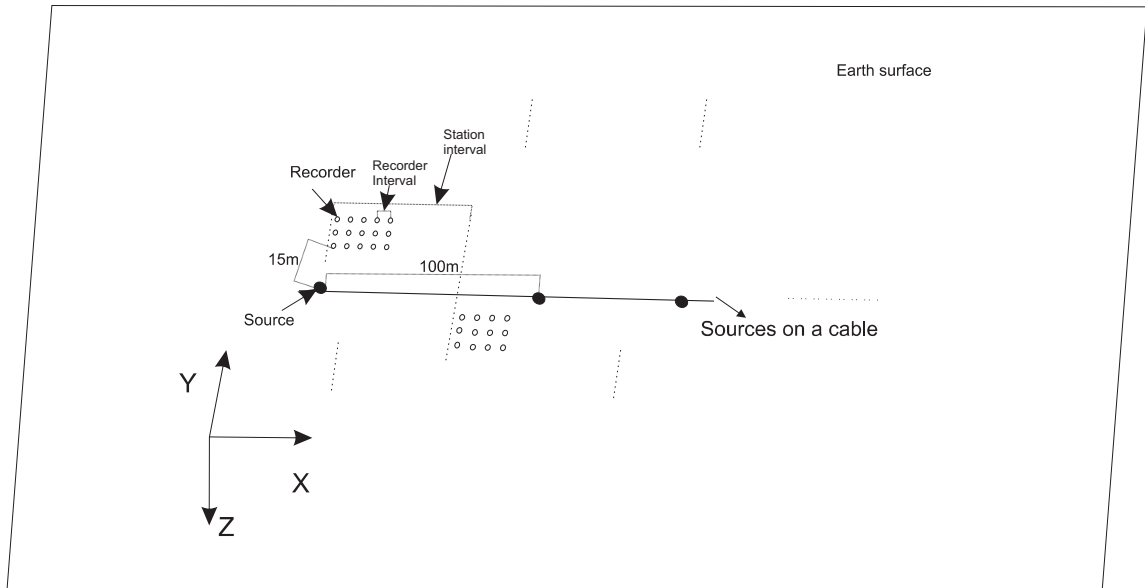


Figure 3.4: an example of 3D seismic acquisition geometry [83]. The group of recorders (stations) are placed in interval distances of 25 meters. Within the station, recorders are placed at distance of 3 meters from each other. The sources are aligned on a cable at distances of 100 meters apart.

Seismic recordings store geophone's impulses as functions of time and positions of the source and the recorder. Figure 3.5 shows reflections at different layers and their corresponding recorded reflection section. Each line of the reflection section is called a seismic trace and shows a time varying seismic signal recorded by a single receiver. The x-coordinate measures the distances of the receivers from the source. Time increases in units of milliseconds downwards. The horizontal coordinate for each line represents the amplitude of the recorded signal (voltage, in principle). The amplitude provides the change in velocity perturbation at the reflector while moving from one media to another. It oscillates indicating changes from a lower acoustic impedance to higher and vice versa.

Seismic traces are sampled in interval time. The sampling interval affects the quality and size of the resulting data. A lower sampling interval results in a higher resolution, but also in a larger data size. A typical sampling interval is 2 milliseconds for the duration of 6 seconds. A seismic survey (eg. from [25]) may have 2^{10} records, each record having 256 traces, resulting in about 2^{30} time samples. For more details of the seismic data acquisition refer to [179] [162] [128].

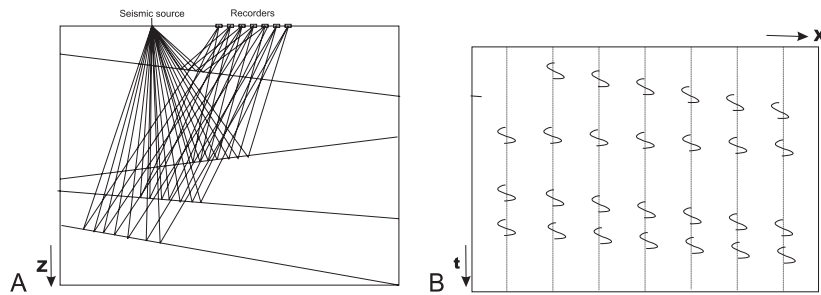


Figure 3.5: A. seismic reflections at different layers. B. recorded seismic reflection section.

3.3 Seismic Data Processing

Seismic data processing aims at productions of interpretable data volumes by noise attenuation and data migration. At the first processing step, the area of the seismic survey is divided into bins, which are commonly in order of 25 meters length and 25 meters width [153]. Seismic traces are usually assigned to bins according to the common midpoint (CMP) between the source and the receiver, reflection point or conversion point (see Figure 3.6A&B). A more sophisticated seismic processing, such as [158], [103] allows for other types of binning. In part, the data quality depends on the number of traces per bin. A lower bin size means a higher resolution; however, a higher bin size also increases the signal-noise ratio.

Seismic traces are seismic responses recorded by a single recorder as a function of time. Distances between the seismic sources and recorders induce a delay in the arrival time of reflections from the same reflectors (see Figure 3.6C). If the traces lie along hyperbolas (plots of arrival times versus distances between sources and recorders), a single velocity function for each reflector can be derived. Then, using the velocity function, the effects of the distances between seismic sources and receivers are compensated. This procedure is called normal moveout (NMO) correction. If the correction is accurate, a given reflection is moved up the trace to the position where it would have been, if source and receiver were coincident (zero-offset trace). Figure 3.6D shows NMO-corrected traces. NMO corrected traces are added together to form one stacked trace (Figure 3.6E). The stacking procedure improves the signal-to-noise ratio and reduces the data significantly.

Seismic sections are stacked assuming horizontal reflectors; however, in reality, reflectors are inclined in a direction or dip. The migration processing step ‘migrates’ stacked sections to their true subsurface position (Figure 3.7), and recovers the true orientation of reflectors. It is done by deconvolution with spatial wavelets representing downward and upward effects. There are numerous methods of migration, such as dip moveout (DMO), frequency domain, ray-trace and

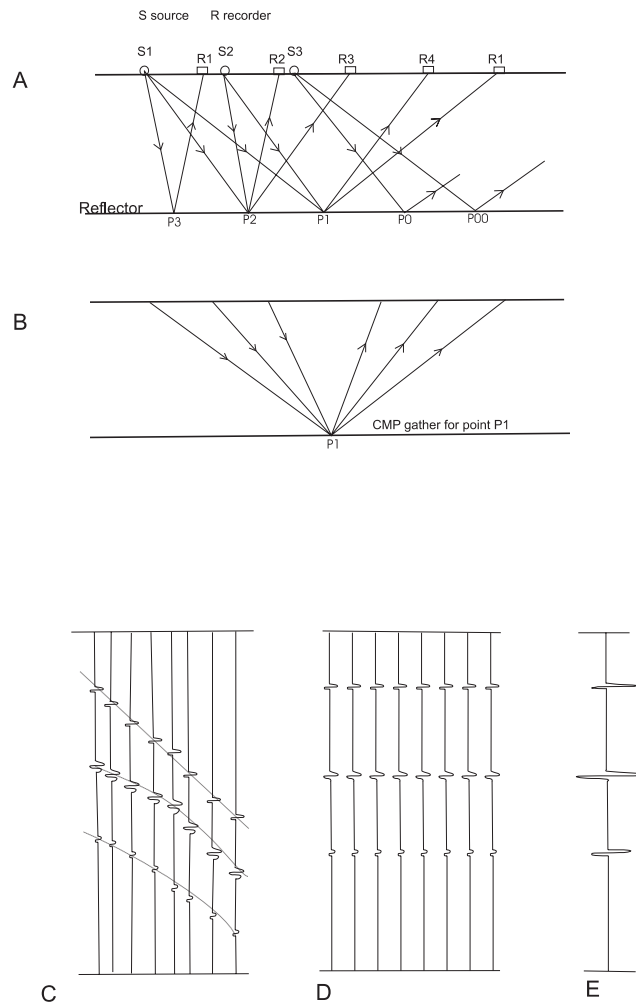


Figure 3.6: A. various raypaths from successive shot locations to the recorders. B. common reflection or depth point on horizontal reflector. C. recorded seismic traces. D. moveout corrected traces. E. stacked or summed traces.

wave-equation migrations. For details of the seismic migration procedure refer to [126] [64] [122]. Figure 3.8 shows a closely spaced stacked seismic section and its migrated section.

Additional processing such as

1. removing surface waves which coexist with the recorded P-waves,
2. attenuation of multiple reflections at reflection boundaries,
3. compensations for a layer of low seismic velocity material near the surface of the earth (static corrections),
4. corrections to compensate for differences in positions of the sources and receivers

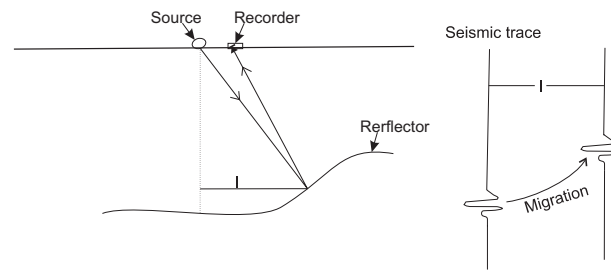


Figure 3.7: illustrates the concept of migrations. Migration adjusts the location of events in seismic traces to compensate for dipping reflectors. Modified from [153].

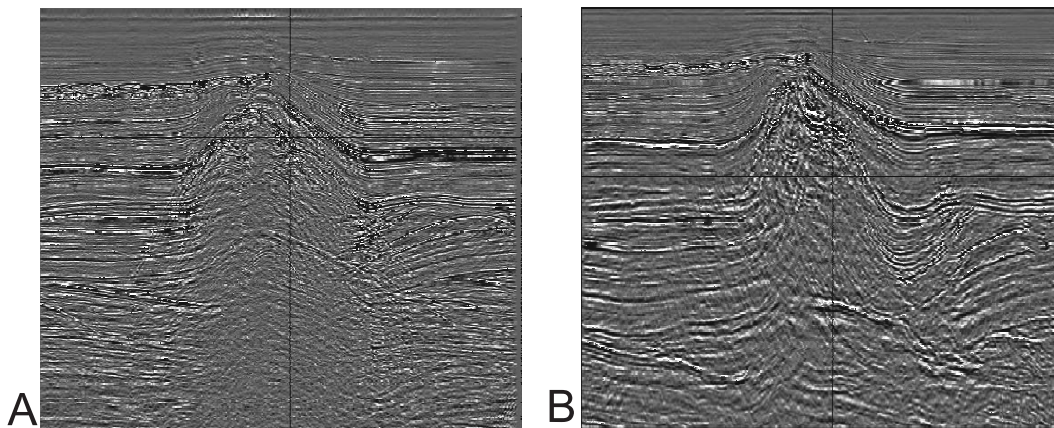


Figure 3.8: A. zero-offset stacked section. B. migrated section. (Courtesy of Stanford Exploration Project)

are done at different stages of the seismic processing. For details of seismic processing see [189]. Methods for removing undesired wave types and multiples are reported in [118] [169]. After the processing steps, seismic images that may be interpreted as geologic section, are produced.

3.4 Structural Interpretation of Seismic Data

Seismic interpretation is the analysis of seismic data to generate reasonable models and predictions about structures and properties of subsurfaces[153]. There are several stages of seismic interpretation, each dealing with different aspects of the subsurface. Models resulting from each stage are integrated to form a detailed geological subsurface model. Seismic interpretation stages are well discussed and illustrated in [29]. Additional reviews on 3D seismic interpretation can be found in [27] [30]. Automation efforts are focused on the structural interpretation stage. It was reported that the structural interpretation tasks take up to 70% of the interpreter's time in interpretation projects [78].

During the structural interpretation of seismic data, interpreters preview the data in order to identify subsurface structures, such as rock layers and faults. Rock layers are the result of long-time sedimentation processes, and consequently, each layer forms a surface that approximately corresponds to the earth's surface at a certain time in the past. Discontinuities in the layered surfaces often reveal faults or channels.

Interpretive processes are now being done using modern interpretation software packages, such as the Kingdom Suite of Seismic Micro [91] or the Interpret2000 package of the Landmark Cooperation [46]. The seismic data volume is previewed in the dimensions of inline, cross-line, and time (Figure 3.9 and Figure 3.10). Image planes in any direction through the seismic volume can also be displayed. By convention, surface reflection from an increase in acoustic impedance is stored as a negative number, while surface reflection from a decrease in acoustic impedance is stored as positive number. The actual range of seismic data displayed on a workstation depends on the software used. Furthermore, the optimal color scheme depends on the information that is needed to be highlighted. The interpreter has the option to choose a color map accordingly.

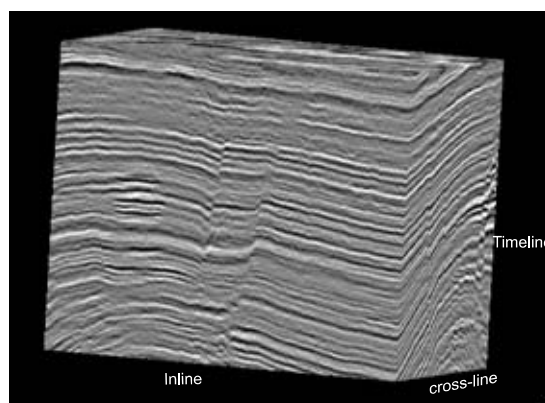


Figure 3.9: Seismic cube.

Given the seismic volume and software packages, the primary challenges for the interpreters are to fill in the areas of poor data and to characterize structural features, such as faults and horizons. The interpretation procedures for faults and horizons are described in the next subsections.

3.4.1 Fault Interpretation

Fault interpretation is about defining fault surfaces, along which rock layers are displaced relative to each other. Fault surfaces are identified by finding terminations in otherwise continuous horizons [29]. As the major terminations are only visible when viewed at higher angle, faults are interpreted at high angle (above 45 degree) to the fault plane.

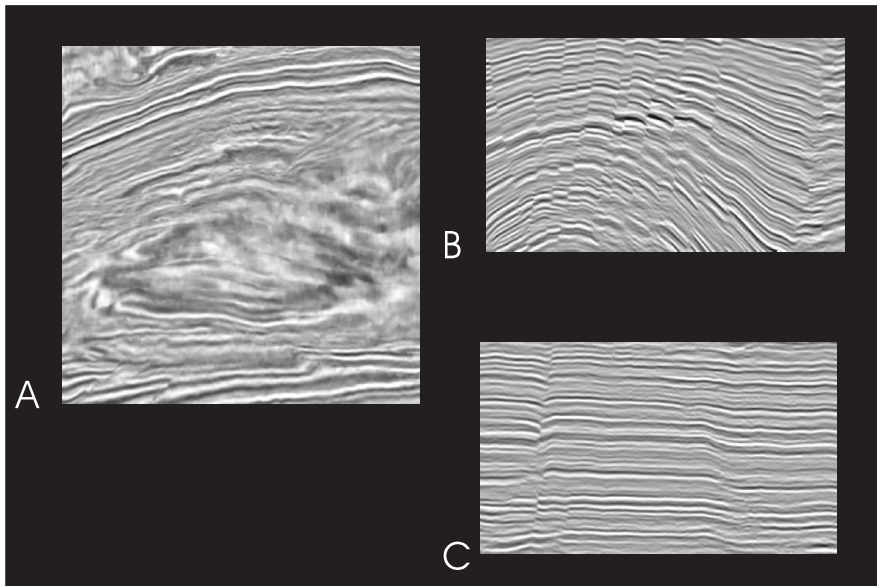


Figure 3.10: Seismic data preview in 2D A. time slice B. inline slice C. crossline slice.

Interpreters examine vertical sections (or slices) for horizon discontinuities and specify a line segment regressing through the discontinuities. If a single line segment does not interpolate well, multiple line segments are specified. The interpreters navigate through a sequence of slices to map the entire fault. A 3D fault plane is fitted to the mapped fault lines. The fault planes are examined for smoothness translation and for a geologically feasible interconnection with other faults. Some faults can be finalized only after interpreting a few horizons, whilst the fault termination is dependent on the seismic resolution [156].

Discontinuity highlighting tools such as coherency, dip-magnitude, and dip-azimuth assist fault interpretation. The coherence cube [21] is a measure of lateral change between neighboring traces. It enhances fault features making them easier to identify. Extensions to coherence cube are reported in [36] [116] [39] [37]. Figure 3.11 illustrates the coherency-based fault interpretation on 3D seismic volume.

The fault interpretation procedure is still a very time-consuming task. Interpreters often need to define a few hundreds up to several thousands of points within a 3D seismic volume in order to track the accurate spatial position of faults. A detailed interpretation is usually restricted to interesting locations, such as big faults and reservoirs.

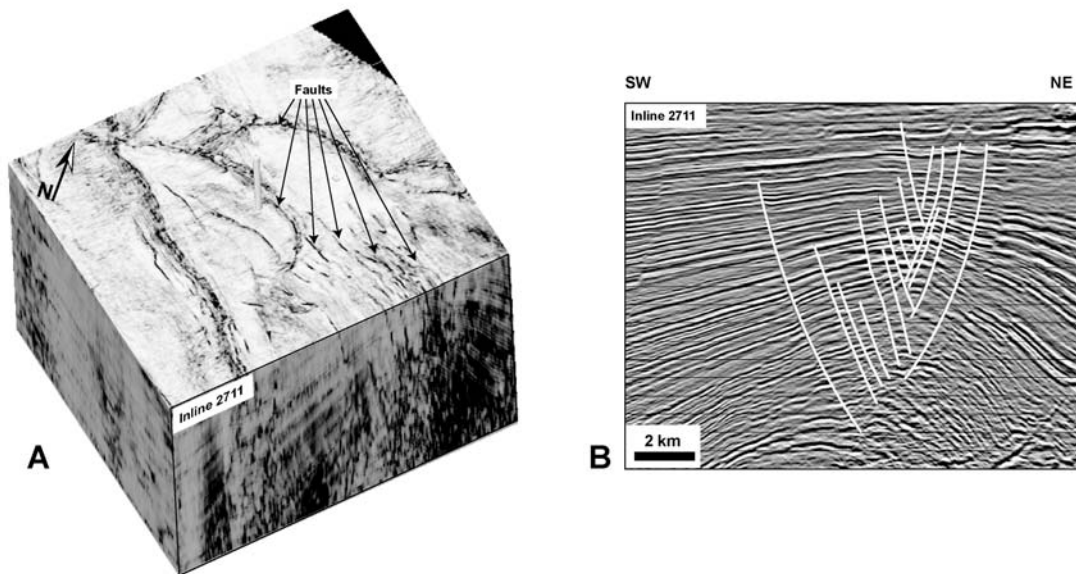


Figure 3.11: A: seismic coherency of 3D seismic volume. High-coherence values in white, low-coherence values in black. B: seismic reflectivity image of inline slice, and interpreted faults (white lines).

3.4.2 Horizon Interpretation

Horizon interpretation deals with identifying maximum flooding surfaces (horizons) of individual rock layers. The major events to be selected for horizon interpretation are discontinuity surfaces between sequence boundaries and continuity surfaces with a good impedance contrast. Horizons are tracked with regular patterns of seed lines to approximate the small portion of local data continuity.

Autotrackers [53] widely assist horizon interpretation. They start from manually supplied seed points and track horizon surfaces in 3D data volume. The tracking is performed by following similar features in neighboring traces in 2D seismic sections. Details of the tracking algorithm are found in [80]. Advanced techniques such as 3D voxel tracking [53], surface tracking [58] or neural networks [120] [106] have also been introduced. Nevertheless, 2D trackers are still widely used because of their easiness for interactive editing.

Autotrackers fail in areas of data discontinuities, such as a fault surface. Incorrect jump tracking may happen unless the appropriate matches of horizons across faults are found.

3.4.3 Horizon Matching across Faults

Horizon matching across faults is complicated due to the nature of the faulting process. First, faults displace horizons nonlinearly. Unless the full extent of the faults is observed in the data, it is difficult or impossible to accurately establish the continuity for each horizon. Second, a faulting process creates damage zones where the seismic data are distorted significantly, and misleading hydrocarbon indicators may lead to a wrong interpretation. Finally, the geological fate of the two sides of the fault may be different. Independently occurred deposition and erosion events produce scaling differences between former continuous horizons. Some horizons may not have matches on either side, due to long-time erosions that wash them away and make them fall short of seismic observation.

Single matching of horizons across faults is possible if there are strong features, such as a strong stable reflection from channels, unconformities, isolated sands or shales. However, in most cases, sequence characteristics of several horizons are considered for matching decisions. The decisions are started with tentative matchings for horizons at low-fault offset regions or with stronger reflection events. The tentative matchings are then examined to get an idea about the fault offset distributions. If the distributions are acceptable, then matchings at deeper or less strong horizons are found.

3.5 Concluding Remarks

Seismic imaging uses the principles of seismic wave propagation. Artificially created seismic waves are reflected between rock layers which have different velocities because of their variation in density and elastic properties. In order to cover the details of the 3D nature of the subsurface, the area under the seismic survey needs to be properly illuminated by using seismic sources and recorders. The interpretable seismic data are the result of several processing stages.

Interpreters view seismic data and use their expertise to identify rock layer structures. Interpretation results are crucial for underground prospect investigations and influence the subsequent economic gain. Data enhancing and automation tools facilitate interpretations of faults and horizons. Automation tools fall short of tracking faults and matching horizons across faults. In the next chapter, the research issues of the seismic data analysis are discussed.

4 Research Issues of Seismic Data Analysis

This chapter describes major research issues of the seismic data analysis. The quality of seismic data affects the interpretation results. High data quality reduces the risks associated with misinterpretations. The oil industry is constantly looking for better data acquisition and processing methods. The size of seismic data sets has also increased tremendously over the last three decades, leading to an increasing demand for efficient interpretation procedures. Therefore, the major research issues of seismic data analysis are :

1. Improving data quality
2. Information presentation with data enhancing tools
3. Information extractions with automation tools.

In the following sections, these research issues are discussed, and new approaches for an automated seismic data analysis are outlined.

4.1 Improving Data Quality

An improved data quality is achieved through maximization of signal-to-noise ratio and optimization of data resolution. Each step in the data acquisition and processing determines the resulting data quality. Attempts to increase the signal-to-noise ratio start from the advancement of the wave propagation theory [16] [186]. Recent works in [179] [180] [178] [26] discuss the optimization of a seismic survey design in order to acquire better quality seismic data at lower costs. Common mid-point processing and post-stack migration are still the most popular routes in seismic processing but current research dedicated to partial and full pre-stack migration techniques, such as those in [141, 190, 43] are catching up.

Vertical and lateral resolution limits in seismic data are dependent on wavelet characteristics and elastic parameters of subsurface layers. Research works in deconvolution [139, 140] attempt to

increase the spatial data resolution with new wavelet estimates and optimization strategies. The work in [183] attempts to remove the earth attenuation to produce high-resolution data. Up to date research work in the seismic data acquisition and processing are published in SEG journals [154].

4.2 Data Enhancing

In recent years, seismic surveys have provided clearer subsurface images with finer details. The developments have contributed to an increase of the total amount of data per survey. In order to make use of these advancements, the classical interpretation procedures are being improved.

Data enhancing tools aim to create an intuitive display that allows an interpretation task to be performed both more efficiently and more effectively. They are analysis methods applied to seismic volumes or slices to highlight structures.

Many analysis methods have been introduced in the past. The complex trace analysis [167] [95] [166] treats seismic amplitudes as analytical signals. Then, the amplitude function, the instantaneous phase, and the frequency are used to measure and detect local features of the signal. These features can be displayed in a color-encoded manner, which helps an interpreter to see their interrelationship and spatial changes or be further analyzed to enhance particular structures.

3D filters are also popular data enhancing methods producing attribute volumes depending on the filter kernel. The coherence cube, dip and azimuth volumes are examples of volume attributes. The coherence cube highlights data discontinuities, while the dip and azimuth volumes estimate the local dominating orientation angle [49]. Advanced methods for computing dip and azimuth volumes are introduced in [110] [114]. 3D texture attributes [152] [38] [143] are also gaining popularity. They are computed by choosing a cubic texture element from the seismic data to generate a grey-level co-occurrence matrix, which in turn is used to compute second order statistical measures of textural characteristics. The cubic element is propagated through the 3D seismic volume to transform it to texture attributes. The texture attributes have been used to identify local structural variations and rock stratigraphic.

Common post-stack or post-migration seismic noise filtering techniques work on the basis of frequency or amplitude. More sophisticated noise filter methods are being developed. For example, [84] introduces a fast structural interpretation with structure-oriented filtering. Edge preserving seismic data enhancing methods [109] [108] and 3D structure tensors [23] are also used to en-

hance various structures including faults and to isolate structures of interest in the data. Structure tensors are orientation-adaptive Gaussian filters, which preserve local structures by elongating the filter window along the dominant structural orientation.

Volume rendering tools are now part of most seismic interpretation packages. The interactive faster animation of seismic slices provides the sense of structural changes. Direct-volume rendering of the volume data is also accomplished by providing a transfer function and camera location. 3D seismic volume visualization tools, such as SVI Pro of the ffA [60], have improved the interpretation process. Current research, aiming at creating a virtual environment to visualize well paths or channels through a dense 3D volume, is reported in [28].

Detections of certain geological features, such as faults and horizons, are facilitated by data enhancing tools. Rendering of interpreted surface helps an interpreter to capture the 3D nature of the subsurface.

4.3 Automation

Automation-where it is possible-provides the best efficiency. Besides reducing the time of interpreters, computer-assisted solutions, based on a quantitative model, provide a repeatable data analysis tool.

The automated interpretation of horizons is one of the areas where the tools of modern interactive interpretation systems have made the most significant impact. Auto-picking or auto-trackers (reviewed in [53]) have been commonly used to assist horizon tracking. Autopicking tools are aimed at extending manually selected seismic traces based on local similarity measures. They perform well if there are uninterrupted horizon features. But horizon interruptions are very common.

Approaches for the automatic fault-surface extraction from 3D seismic data often follow a data-driven strategy with potential fault locations being combined using local continuity constraints. The method from [142] uses ‘artificial ants’ to suppress noise from fault attributes computed from spatial discontinuities. Further technical developments of this method are published in [136] and [137]. The fault extraction method of [66] uses a coherency measure to detect points of significant discontinuities, and applies a highest confidence first merging strategy with a flexible fault-surface model. The automated fault extraction (AFE) method of [54] combines signal processing technology with geological knowledge based on 3D seismic coherency volumes, whereas [168] uses a technique based on the structural oriented filtering of reflectance data and

subsequent fault extraction. Fault enhancement is the goal of the method of [171], where semi-automatically extracted directive attributes are enhanced by a trained neural network. In [170], an artificial neural network produces a fault probability cube from integrating different fault enhancing attributes (e.g. similarity, frequency, curvature). However, the 3D interpretation of geological features lacking seismic similarity, i.e. faults, still remains a manual task.

4.4 Previous Methods for Automated Horizon Matching across Faults

There are two works that deal with the automation of horizon matchings across faults. The work in [13] introduces a horizon mapping strategy that matches horizons across discontinuities. The strategy employs a pattern classification algorithm followed by a decision-making procedure. The pattern classification step employs artificial neural networks using resilient propagation. The training is achieved by using patterns constructed from a suite of seismic attributes. A decision tree is constructed by extending a single-horizon binary tree to a multi-horizon n-tree. Matching solutions are searched in the tree using a branch-and-bound search optimization method. The solution search is conducted mainly in order to establish horizon continuities across simple discontinuities such as those caused by noise or small fault offsets. The classification algorithm requires training samples, which are tedious to generate. Automated matching results of this method were only given for three selected horizons making it difficult to judge its performance.

Claiming that the previous method suffered from using exclusively local image information, the second work in [14] uses a model-based scheme for correlation of horizons at normal faults in 2D seismic images. Well-defined horizon segments on both sides of the fault were extracted and matched based on the local correlation of seismic intensity and geological knowledge. Since the exhaustive search for an optimal solution of correlation is unfeasible, [14] suggests the genetic algorithm as optimization technique. However, a pure two-dimensional approach lacks efficiency and is only suitable if the information of the 2D seismic slice is sufficient for the evaluation of the geological constraints.

This thesis presents a new automated method for horizon matching across a fault. The method is aimed to provide a more robust and plausible interpretation at faults.

It extends previous approaches to exploit existing 3D spatial relationships in the data and adopts a well established probability theory to find the most likely configuration or the optimal matching solution. The prior knowledge about horizon offset distributions is integrated through the

functional approximation of a fault throw function. Seismic data features are mapped to a Gaussian process which allows to specify a priori smoothness.

Optimal matching solutions are found in multi-resolution fashion. At the coarse scale, few prominent horizons are selected and matched. At the finer scales, more subtle horizons are matched guided by results from the coarser scales.

4.5 Concluding Remarks

In this chapter, the research issues of the seismic data analysis have been discussed. More sophisticated data acquisition and processing methods are being researched to improve the quality of seismic data. New data enhancing and automating methods are still part of active research. A partial success is reported in horizon tracking; however, the structural interpretation is still largely manual.

In the next chapter, a new semi-automatic fault-tracking approach is presented. It provides a computationally inexpensive alternative to routine fault highlighter (e.g. coherency, semblance) through the use of log-Gabor filters, and adopts an active contour to fault tracking. It is capable of searching for smooth fault curves in noisy 3D seismic data with partially missing signal. Interpreter interactions are needed only to specify the seed line and the fault's orientation range. The necessity for subsequent interaction is then reduced by letting the automated fault interpretation proceed independently in three dimensions into the seismic volume of interest.

An automated method for horizon matching across faults is described in Chapters 6 to 8. In Chapter 6, a novel horizon matching model is defined under a stochastic framework by a marked point process. The framework integrates the prior knowledge of faults and horizon with seismic data observation. Fault surfaces are extracted by using the semi-automated fault tracking tool. Horizon geometries are defined within the fault patch sections. Each horizon geometry was treated as an object in the stochastic configuration and its seismic features are modelled as a gaussian random process. Interactions are defined among different objects to impose prior geological constraints. Chapter 7 develops an efficient search strategy to sample from the stochastic matching model and to find the optimal matching solution. The semantic scale space representation of horizons is also defined. Validation results of the matching algorithm are reported in Chapter 8.

5 Auto-tracking of Faults

This chapter describes a new method for auto-tracking of faults in 3D seismic data. Since there is no readily available tool for fault tracking, this auto-tracking method is researched and developed in order to support the automating of horizon matching across faults. The method has been published in the Geophysics journal [2]. In the first section of the chapter the scope of the method and basic assumptions are explained. In Section 5.2 and 5.3, details of the method are presented. Auto-interpretation results achieved on a 3D seismic volume are presented and discussed in Section 5.4 and 5.5. The final section presents conclusions and directions to future works.

5.1 Scope and Assumptions

In 3D seismic data, faults rarely give rise to reflection events. They are recognized by reflection discontinuities. A fault auto-tracking method is proposed to track such discontinuities in order to build a single fault surface. A planar fault structure is assumed. A sequence of slices is given from adjacent areas of the subsurface, and the distance interval between the sequences is not big enough to change the fault orientations and size. Auto-tracking stops at fault interconnections or branching. Examples of auto-tracking results are shown on Figure 5.4C.

The proposed method consists of two steps: fault highlighting and tracking. At the fault highlight step, fault attribute slices highlighting discontinuities orthogonal to the reflection events (horizons) are produced. The log-Gabor filter is utilized to generate the attribute slices. A user specifies a seed fault line as well as the range of the fault's orientation. The subsequent fault tracking step fits an active contour to the fault highlighted voxels. The active contour searches for a connected smooth curve which fits the data. These steps are described in the next two sections.

5.2 Fault Highlighting

Fault highlighting is used as a term for enhancing lateral discontinuities of seismic reflections. Fault highlighting can be considered as the computation of fault probabilities for each voxel of a 3D seismic data volume. Techniques such as coherency [22], semblance [115], or the use of the eigenstructure of the data covariance matrix [65] are already introduced for discontinuity-enhancing in seismic data. These techniques are designed to emphasize spatial discontinuities computed at every data point. Consequently, they are very sensitive to random structures and known to be computationally expensive.

The new fault tracking procedure adopts log-Gabor filters for a robust and fast fault highlighting. A Gabor filter [185] is a bandpass filter whose impulse response is defined by a harmonic function multiplied by a Gaussian function. Suppose x and y are spatial image coordinates, the impulse response of a Gabor filter $\mathbf{g}(x, y)$ is then given by [75],

$$\mathbf{g}(x, y; \lambda, \theta, \psi, \sigma, \gamma) = \exp\left(-\frac{x'^2 + \gamma^2 y'^2}{2\sigma^2}\right) \cos\left(2\pi \frac{x'}{\lambda} + \varphi\right), \quad (5.1)$$

where

$$x' = x \cos \theta + y \sin \theta, \text{ and } y' = -x \sin \theta + y \cos \theta.$$

In this equation, λ represents the wavelength of the cosine factor, θ represents the orientation of the normal to the parallel stripes of a Gabor function, φ is the phase offset, and γ is the spatial aspect ratio and specifies the ellipticity of the support of the Gabor function. Figure 5.1 displays the Gabor function image. For details of the Gabor function refer to [75] and the references therein.

Gabor filters are directionally sensitive, linear filters with local support in the frequency domain and have long been used for enhancing local and directed structures in various data. They are well suited for highlighting fault systems because of the local, anisotropic nature of the discontinuity of the seismic signal at faults. However, their main disadvantage is that they cannot be constructed with an arbitrary bandwidth without making the filter output dependent on the input data intensity.

The log-Gabor filter, a variant of the Gabor filter, is chosen to enhance the discontinuities at a particular orientation of a fault of interest. It was first introduced by [61] to model visual cortex cells, and has since been used for image processing particularly for feature extractions [42] [113] [157] [188]. Log-Gabor filters are defined as follows on the frequency domain [100],

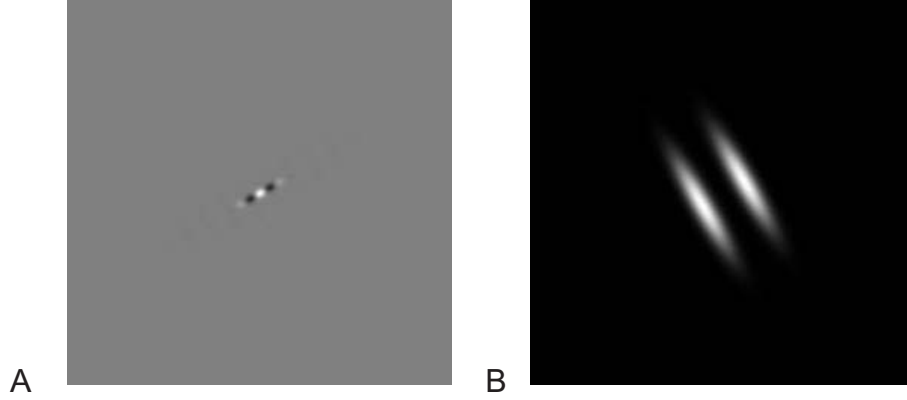


Figure 5.1: A. 2D Gabor function with wavelength=16, orientation=30, Phase offset=0, Aspect ratio=0.5 and bandwidth =1. The bandwidth specifies the spatial-frequency bandwidth of the Gabor filter kernel. B. power spectrum of the 2D Gabor function.

$$G(u, v) = S(u, v)g(u, v). \quad (5.2)$$

$S(u, v)$ is a band-pass filter and defined as

$$S(u, v) = \exp \left[-\frac{\ln\left(\frac{k(u, v)}{k_o}\right)^2}{2\ln\left(\frac{\sigma}{k_o}\right)^2} \right], \quad (5.3)$$

where $k(u, v) = \sqrt{u^2 + v^2}$, k_o is the center frequency, and σ is varied to hold $\frac{\sigma}{k_o}$ constant for various scales. The filter response of $S(u, v)$ is a Gaussian curve in the logarithmic frequency scale. The orientation sensitivity of the log-Gabor filter is achieved by setting

$$g(u, v) = \exp \left[-\frac{(\Delta\theta(u, v))^2}{2\sigma_\theta^2} \right], \quad (5.4)$$

where σ_θ is the standard deviation of the angular Gaussian function, and $\Delta\theta(u, v)$ is computed as

$$\Delta\theta(u, v) = \tan^{-1} \left[\frac{\sin\theta\cos\theta_s - \cos\theta\sin\theta_s}{\cos\theta\cos\theta_s + \sin\theta\sin\theta_s} \right], \quad (5.5)$$

where $\theta = \tan^{-1}(v/u)$ and θ_s is the mean orientation of the faults to be highlighted. Then, the log-Gabor function is

$$G(u, v) = \exp \left[-\left(\frac{\ln\left(\frac{k(u, v)}{k_o}\right)^2}{2\ln\left(\frac{\sigma}{k_o}\right)^2} \right) - \left(\frac{(\Delta\theta(u, v))^2}{2\sigma_\theta^2} \right) \right]. \quad (5.6)$$

Different to the Gabor filter, the log-Gabor filter, by definition, has no DC component and comprises an arbitrary bandwidth in the frequency domain. This means that all edge information of the input signal is used for the filter response while still being independent of the input amplitude. It is an appropriate choice for a fault highlighter, since the property of a voxel of being part of a fault surface does not depend on the strength of the seismic signal on its two sides.

The filter is applied to 2D images, $I(x, y)$, i.e. 2D reflectivity sections extracted from the 3D seismic volume, and x and y are time and crossline position coordinates, respectively. As $G(u, v)$ is defined in the frequency space, the input image is converted from the spatial domain into the frequency domain by using a 2D discrete Fast Fourier Transform (FFT) function

$$I_f(u, v) = FFT\{I(x, y)\}. \quad (5.7)$$

Then the fault highlighted image in the frequency space is computed as

$$F(u, v) = I_f(u, v)G(u, v). \quad (5.8)$$

$$f(x, y) = |(FFT^{-1}\{F(u, v)\})|, \quad (5.9)$$

where $|\cdot|$ computes the modulus of the complex number resulting from inverse FFT. Figure 5.2B shows the modulus of the log-Gabor filter response after convolving it with the seismic inline slice on A. Figure 5.2 C shows the phase image of the log-Gabor filter response and Figure 5.2 D shows the orientation image in which the local energy is a maximum in degrees (0-180), angles positive anti-clockwise. To compute the orientation image, the log-Gabor is applied in 20 different directions. As shown on this figure, compared to the phase and the orientation image, the modulus provides a better fault highlight and suits the active contour-based fault tracking approach. Therefore, $f(x, y)$ represents the modulus of the log-Gabor filter response that clearly enhances oriented amplitude discontinuities at faults, and it serves as input for the fault tracking in the next step. An example showing the modulus of the log-Gabor filter enhancing faults is shown in Figure 5.3.

Previous works in feature extractions [56][55] [187] and face recognition [191] indicate the existence of additional information in the phase of the Gabor filter. Therefore, further investigation of the phase is necessary to exploit the additional information in the phase so that it can be combined with the modulus for a better fault highlight.

The values for orientation and scale parameters depend on the fault of interest to be highlighted. Different responses for ranges of values around the orientation of fault can also be combined

for a better fault highlight. Figure 5.4A shows an example of medium-scale, normal faults highlighted by applying a set of log-Gabor filters at different orientations and scales.

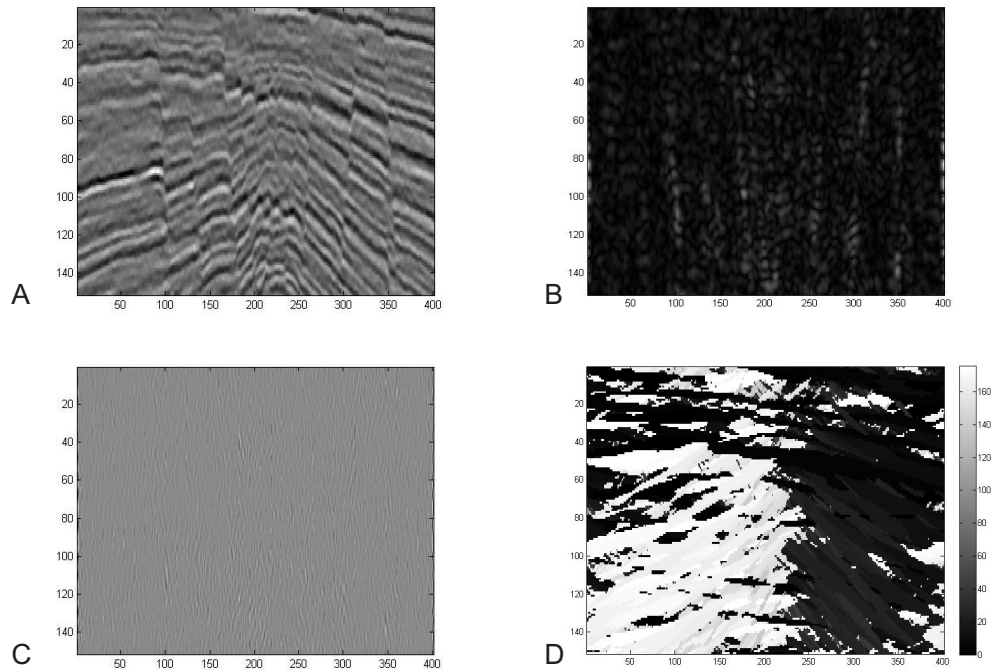


Figure 5.2: A. seismic inline slices. Faults are visible as discontinuities of horizontal reflection events. B. modulus of the log-Gabor filter response with orientation=120 and standard deviation ratio=0.65. C. phase of the log-Gabor filter response. D. orientation image in which the modulus is a maximum in degrees (0-180), angles positive anti-clockwise.

5.3 Fault Tracking

The problem of fault tracking is treated as the search for a group of fault lines that define the maximum probability of the location of one target fault on adjacent, log-Gabor filtered 2D seismic images. Instead of exclusively working on the log-Gabor filter output, any other tightly defined discontinuity attribute, e.g the recently presented attributes in [168], and [54] may possibly be used as alternate database. The fault-tracking prototype operates as active contours [97]. Active contours were presented as a means to integrate geometric continuity information, such as connectedness or smoothness, into the image analysis. An active contour is a deformable curve whose deformation is governed by a model component ensuring smoothness and connectedness, and a data component which lets the contour attach itself to the object during the search in the data. As such they are well suited to describe objects in data with noise or artifacts.

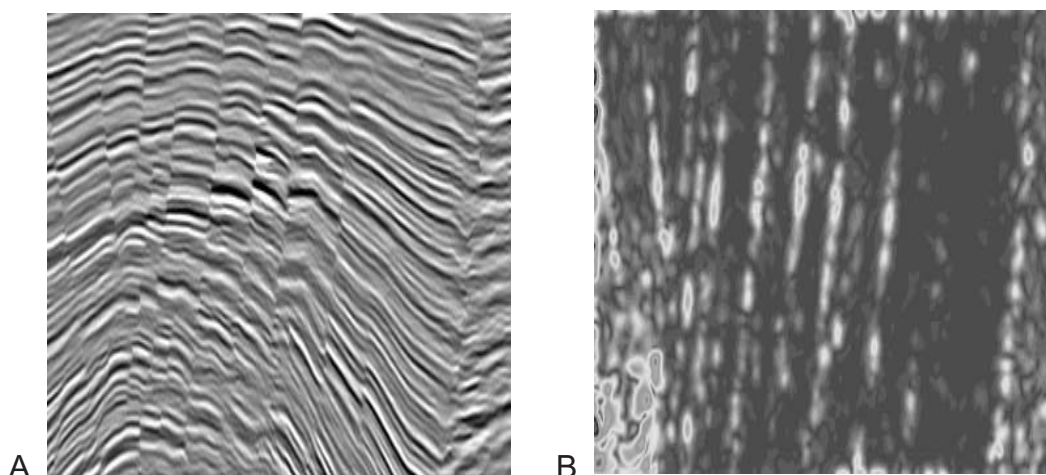


Figure 5.3: A. Seismic inline slices. B. The modulus of the log-Gabor filter response with inputs orientation=60 and standard deviation ratio =3. Fault areas shows higher response (white regions).

Ideally, the data component of the active contour prevails in parts of the curve where the data quality is good, while the model component prevails where the data are distorted or missing. The main application of active contours is to extract geometric objects in data with a low signal to noise ratio or regions of missing signal. An active contour is an appropriate tool to deal with the ambiguities arising when a fault line should be extracted from the fault highlighter output. Because of its ability to attach itself to the geometric structure in the data that it models, the optimal location of a fault on a seismic inline can be searched in a neighborhood of an initial guess for the solution.

A geometric line model for a fault line L_i in a seismic inline S_i of a consecutive sequence of inlines $S_1, \dots, S_i, \dots, S_n$ is represented by an active contour consisting of a set of control-nodes $N_i = \{\mathbf{n}_{i1}, \dots, \mathbf{n}_{im}\}$ that provide the coordinates for a sequence of points on the fault line. Each node or point \mathbf{n}_{ij} for $1 \leq j \leq m$ represents the depth position in time and crossline coordinates, and the nodes are ordered from shallow to deep, i.e. in increasing time steps (or depth). The tracking procedure starts from a seed pick provided by the interpreter as a first guess for a fault on one selected seismic section (see Figure 5.4A). The pick places the active contour N_1^{init} close to the fault line on the first inline S_1 . Then it deforms to the closest amplitude discontinuity highlighted, optimizing the initial interpreter guess by using both its data and model component (Figure 5.4B). A resulting optimum fault track N_i^{final} is subsequently projected forward into the next inline (in this case 25 m apart, see Figure 5.4C), providing an initial pick N_{i+1}^{init} on the next inline, which is again optimized by the active contour. The optimality (or the likelihood) of

the nodes that represent the location of the fault of interest is measured using an energy function shown in equation 5.10.

$$E(N_i) = w_p * E_p(N_i) + w_d * E_d(N_i), \quad (5.10)$$

where w_p and w_d are weights to balance the two components: E_p and E_d . $E_p(N_i)$ is the model component of the active contour. On a given inline S_i , it measures the current deviation of the active contour N_i from its initial position N_i^{init} .

$$E_p(N_i) = \sum_{j=1}^m \|\mathbf{n}_{ij}^{init} - \mathbf{n}_{ij}\|, \quad (5.11)$$

where $\|\cdot\|$ indicates the Euclidean distance between nodes. The weight w_p has a negative value so that the model component restricts the variation of fault line positions in the subsequent sections.

In contrast to the model component, $E_d(N_i)$ is the data component and represents the likelihood energy of the nodes to be the part of a fault (see equation 5.12). It is determined according to the argument that fault locations exhibit a higher log-Gabor filter response compared to the surrounding, un-faulted regions.

$$E_d(N_i) = \sum_j^m \sum_W f(\mathbf{n}_{ij}). \quad (5.12)$$

In equation 5.12, $f(\mathbf{n}_{ij})$ denotes the modulus of the log-Gabor filter response value at node location \mathbf{n}_{ij} . The inner sum averages the filter response over a small window W around \mathbf{n}_{ij} .

The optimum fault line N_i^{final} is then

$$N_i^{final} = \operatorname{argmax}\{E(N_i)\}. \quad (5.13)$$

Since a first-try detection of an optimum fault line is difficult, a dynamic programming [45] is used. It is an iterative algorithm that continuously moves the fault nodes until an optimum fault line solution is found. The tracking of the fault continues on the next inline using the solution from the previous slice as initialization (Figure 5.4C). Automated tracking stops when for a given inline S_i the energy $E(N_i^{final})$ falls below a given threshold indicating a result of low reliability. This threshold is set up a priori to constrain the fault line to a certain range of orientation, and to the required minimum data support. After finding the optimal solution, the tracker adds additional nodes at the top and bottom positions to find out if the fault can grow.

The auto-tracking generally stopped when fault probabilities were very low, which occurred in particular in areas of fault branching, or if the tips of faults were reached (e.g., Figure 5.5). In the case of fault branching, further tracking was only possible by loosening the threshold constraints, or by providing a new initial guess of the solution.

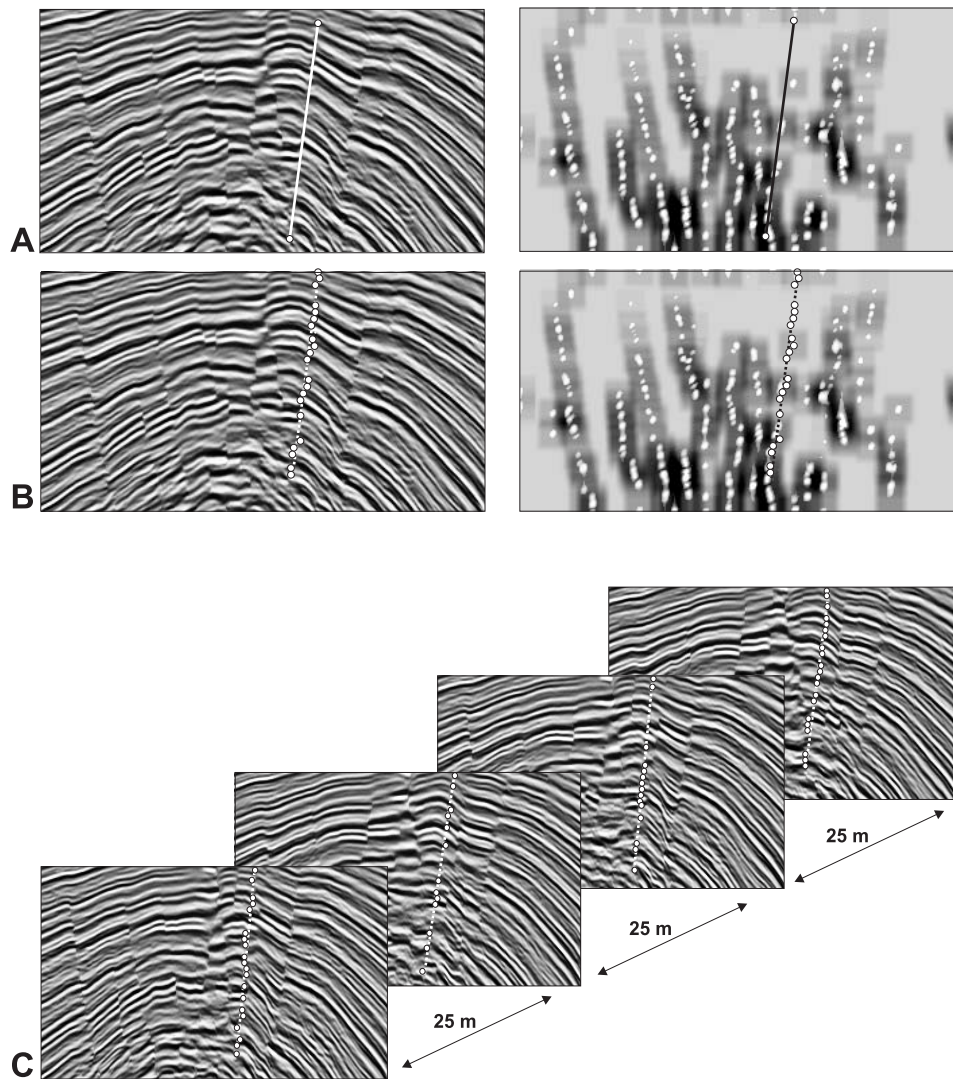


Figure 5.4: Automated fault-tracking workflow. A: Initial seed interpretation of the fault line on the 2D inline seismic slice (left), and reflectivity-based fault pick viewed on the corresponding log-Gabor filtered image (right). B: Deformation of the active contour on reflectivity (left) and the log-Gabor section (right). Position of nodes constrained by data and model component of active contour. Note sensitivity of optimization method at base of fault, where target fault connects to the deeper fault of opposite dip. C: Representative auto-tracking result on series of successive reflectivity sections.

5.4 Results

The workflow for automated fault detection and mapping was developed and tested on series of successive 2D reflectivity sections extracted from a 3D seismic volume from the shallow offshore Niger Delta. The first workstep comprised the application of the log-Gabor filter. The orientation of the log-Gabor filters was specified according to a fast-track estimate of the approximate dip of the fault of interest. The filter response for one selected inline is shown in Figure 5.4A.

For each fault of interest, an initial fault line was mapped on one log-Gabor filtered reflectivity image oriented at a high angle to the selected fault. Then, sample points or nodes were generated on this fault line. The nodes moved iteratively until $N_i^{final} = \operatorname{argmax}\{E(N_i)\}$. The search for the local maxima of the filters response was initiated in the immediate vicinity of the initial interpretation input. Values for w_p and w_d (see equation 5.10) were varied between -0.25 and -0.1 (w_p), and between 0.8 and 1 (w_d) for an optimum solution. These bounding values were found to be robust, generally generating satisfactory results.

Fault lines on the succeeding seismic inline slices were tracked by using the solution from the previous inline as initial guess for the iterative algorithm. Then, the tracking prototype automatically extended the target fault into every following seismic inline slice, canceling the tracking procedure in areas of insufficient data control (loss of filter contrast) or orientation/dip changes. Tracking results for a succession of 25 inlines were generated within a few seconds. In this way, 18 different faults were tracked within a few minutes. In areas of deteriorating seismic information, the tracking procedure encountered problems such as early stopping, which was also the case in areas of fault interconnection or fault branching. In a few of cases of fault branching, apparent misinterpretations (jump-interpretation to adjacent faults) were observed. As solution, the tracking threshold was tightened in order to stop the tracker at branching locations, ultimately forcing user interference to continue fault mapping. However, in comparison with the manual mapping of the same fault surfaces, the auto-tracked faults are valued as higher quality surfaces that comprise up to 21 control nodes per fault on every inline, thus providing far more mapping details than their manually picked counterparts (ultimately interpreted on every 4th inline with up to 8 control nodes). This increase in interpretation density strongly supports subsequent data gridding, which, in turn, supports the construction of tightly constrained 3D fault surfaces. Besides the significant increase in control node density, the auto interpretation in this case study reduced the fault interpretation time to less than 1 hour, compared to around 1 day interpretation time needed for the manual interpretation of the studied fault zone.

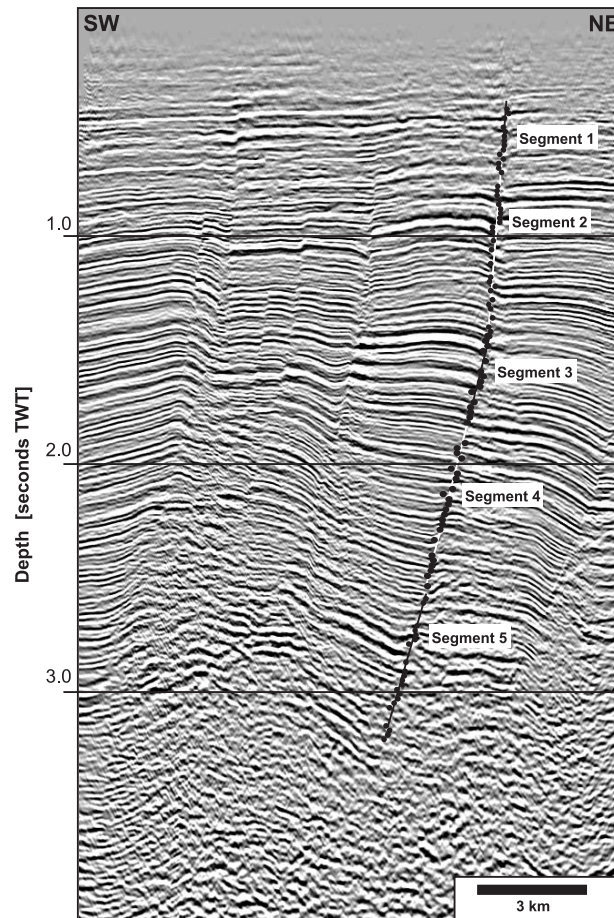


Figure 5.5: Example of the sequential auto-tracking of a large-scale, fault characterized by an apparently curved geometry (display in two-way-time [TWT]). Fault control nodes are indicated as black dots. Successful fault picking in variable dip domains orientation results from the integration of five individually tracked fault segments. Note tracker sensitivity to data limitations at top of segment 1 and bottom of segment 5 (loss of filter contrast).

5.5 Discussion

Fault tracking using an explicit model of the geometric appearance of the fault has the advantage that the model substantially reduces ambiguities in the localization of a (possibly curved) fault line. It essentially treats fault tracking as a regression task of distorted data to a given line of unknown location, orientation and curvedness. Instead of extracting entire fault networks as in [54], and [168], the tracker prototype of this study manages the automatic mapping of single, hand selected faults, thus focusing the interpretation onto the target of interest similarly to the behaviour of horizon autotrackers. The fault tracking framework developed comprises an interactive software component to guide and edit fault detection. It intentionally integrates user knowledge into the fault tracking procedure. The model component serves as a representation for simple geometric assumptions about faults. It can be corrected or superseded by an interpreter's knowledge in cases where the model is insufficient to explain the data. The accuracy of the automated mapping can be immediately checked by the interpreter. The interpreter has access to edit, direct, or vary a priori constraints such as tracker sensitivity or dip range on the autotracker. The mapping of curved fault planes, if present in the studied volume, can be achieved in sequential tracking steps controlled by the chosen orientation sensitivity of the tracker (Figure 5.5). The dependency of the fault tracker on a possibly oversimplistic 2D fault model restricts the geometrical constraints included in the tracking procedure to information relating to one fault line mapped on one seismic inline (preferentially oriented perpendicular to the target fault). However, the first success of this strategy indicates that an extension of the approach towards a full 3D application or towards the tracking of fault networks should be investigated. Various 3D versions of the active contour geometric model exist and their application will enable the exploitation of geometric continuity constraints between inlines. This could lead to a further optimization of the tracking procedure while retaining the ability for user intervention in cases where superior knowledge on fault interpretation is needed. An extension of the approach on certain types of faults systems, on the other hand, would allow the user to specify properties pertaining to groups of faults such as average distance or change of dip angle between adjacent faults to be integrated in the model. In summary, model-based fault tracking is intended as a strategy to provide a better computer-based representation for user input in the interactive seismic data interpretation compared to conventional manual fault-mapping techniques. As such, it can reduce repetitive and tedious tasks in seismic data interpretation significantly. It may even enable structural interpreters to guide interpretation decisions in cases of tectonic ambiguity. As fault interpretation is an iterative process of many cycles, the inclusion of an automated-fault tracking process in standard interpretation tasks will support a more rapid convergence to the final interpretation result.

5.6 Conclusions

The fault highlighting and tracking functionality developed is a prototype and works on series of successive bitmap images of seismic reflectivity data. Testing results on inline extractions from a 3D seismic volume from shallow-offshore Nigeria are promising, since they show 1) a high potential of the log-Gabor filter technique for fault visualization, and 2) robust fault auto-tracking results generated within a fraction of time normally spent by a seismic interpreter.

The semi-automatic fault-tracking approach provides a computationally inexpensive alternative to routine fault highlighters (e.g. coherency, semblance) through the use of the modulus of log-Gabor filters.

The auto-tracking is implemented with the aim to track only single faults; however, the success of this strategy indicates that an extension of the approach towards the tracking of fault networks (simultaneous tracking of multiple faults) should be investigated. In addition, the fault-highlighting component applied could be fused with other similarity measurements to further optimize estimates of fault probabilities.

This chapter about the auto-tracking method provides the necessary fault surface definition for the automated horizon matching method described in the next two chapters.

6 Automated Horizon Matching: Matching Model

This chapter deals with automating the task of horizon matchings across the fault surface. The first section of the chapter explains the scope of the matching problem and the basic assumptions. In Section 6.2, the knowledge base to match horizons across faults is described and Section 6.3 provides the abstraction of the problem. Section 6.4 develops a stochastic matching model to map a set of matching pairs into a similarity measure real value, and explains techniques to compute features for the matching decision. Section 6.5 describes the density and energy measures derived for the marked point process. Section 6.7 explains how optimal matching solutions can be inferred from the matching model.

6.1 Scope and Assumption

The problem to automate horizon matching across a fault is defined as designing an algorithm which automatically gathers seismic features on the two sides of a fault and finds an optimal match between them.

The scope of the matching is restricted to fault patch regions. A fault patch is a subset of 3D seismic data and contains a fault surface with uninterrupted (un-faulted) seismic sections (see Figure 6.1A). Within the fault patch, topologies of a fault and horizons are defined as surfaces through a set of coordinates in 3D. A fault auto-tracking method, previously introduced in Chapter 5, is utilized to define the fault surface. The sections on the two sides of the fault surface are considered to be displaced only under the influence of this single fault surface.

A semi-automatic horizon tracking procedure is utilized to track horizons in the un-faulted regions. The procedure builds a 3D horizon surface by merging ridges from the same horizon. Starting from some seed ridge segments, the procedure tracks fragmented horizon segments in a sequence of slices in attempt to form layers of horizon surfaces. However, it does not attempt to match the ridges across the fault. The tracking works in a multi-resolution fashion, where

first complete horizon segments are identified as reference. Then, for each fragmented segment, average distances from the closest complete segments are computed. These distances are used as clues to locate and merge fragmented horizon segments (see Figure 6.2). Figure 6.3 demonstrates the result of the horizon tracking procedure. Using this procedure, horizon surfaces are defined within each block of the fault patch (that is, in foot- and hanging-wall blocks, see Figure 6.1B), and are given unique labels so that they can be identified for the matching task. Horizon surfaces can also be defined by using horizon auto-tracking tools (for example using 2D horizon picking [129], auto-trackers [53], and 3D picking tools [58]).

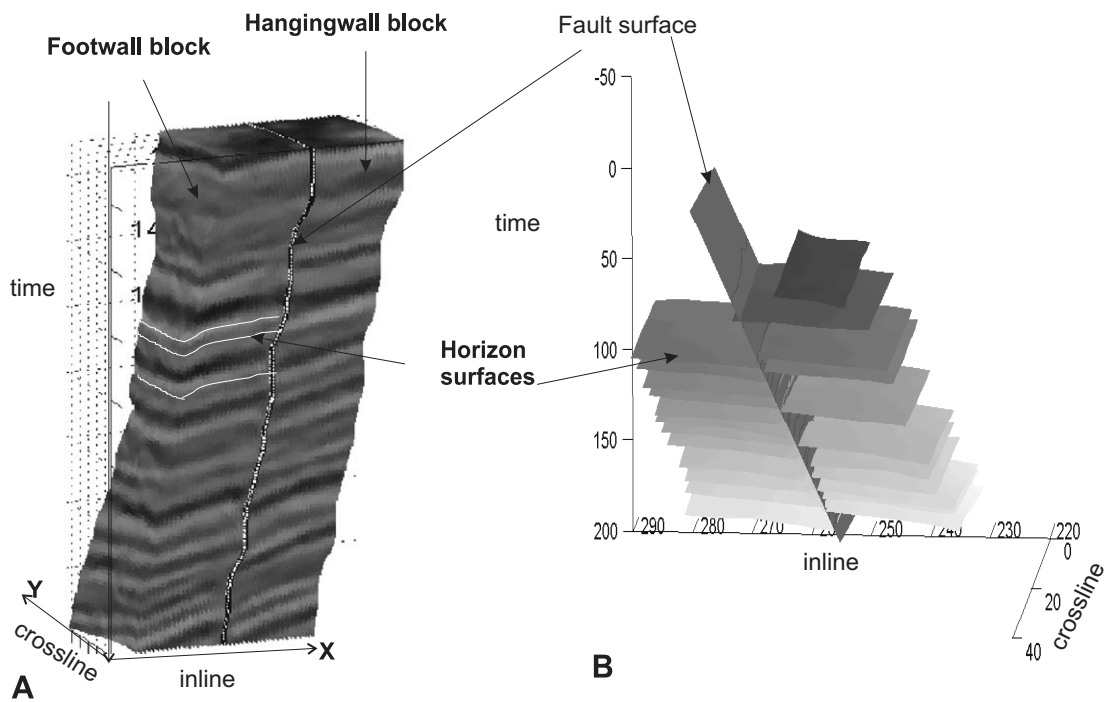


Figure 6.1: A. a fault patch with definition of a fault surface and two horizon surfaces. Each block of the fault patch is also identified as footwall or hanging-wall. B. a geometric scene of a fault patch illustrating extracted geometries of the fault and the horizons.

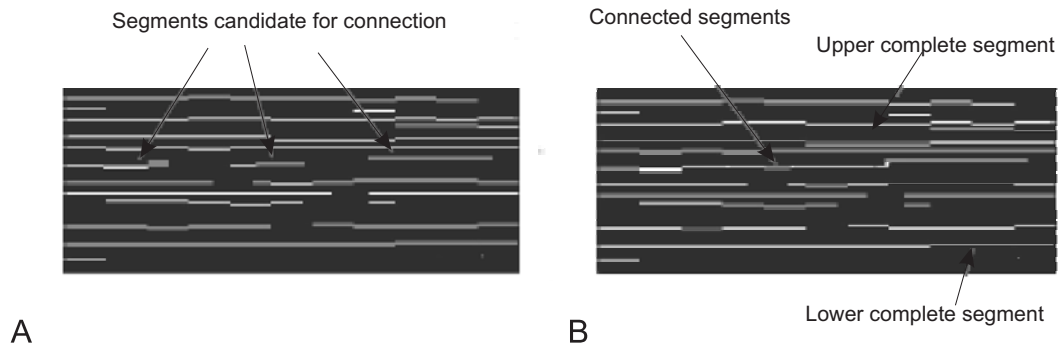


Figure 6.2: Horizon tracking procedure. A. segments resulting from the application of a ridge detection algorithm. B. disconnected ridges of the same horizon are merged using the clue from the distances from upper and lower complete segments.

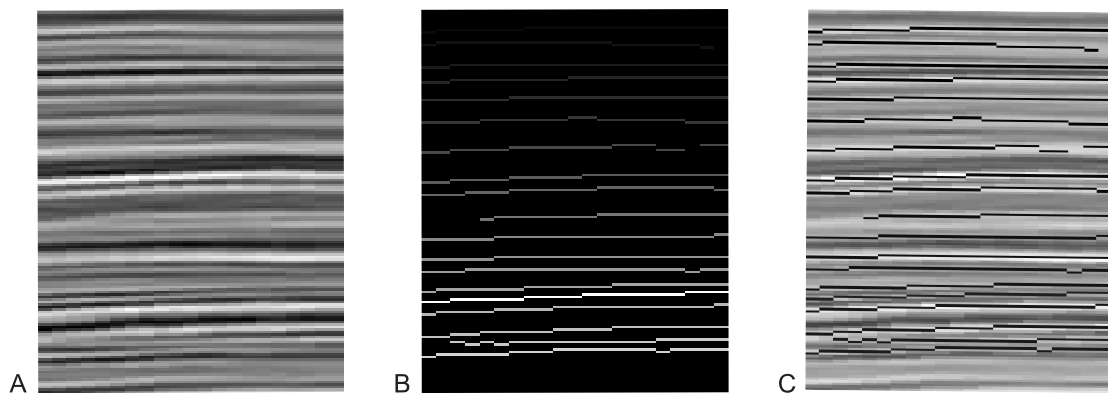


Figure 6.3: A. a seismic inline slice taken from the footwall block of a fault patch. B. labelled horizon segments resulting from the horizon tracking procedure. Note that the contrasts of the segments reflect the different labels. C. horizon segments from B are embedded into the seismic inline slice from A.

6.2 Knowledge Base to Match Horizons across Faults

Horizon matching is a visual perception problem [67], where the correspondence analysis between the two sides of a fault is supported by visual seismic features. The correspondence analysis is actively researched in image analysis. Various automation methods are introduced for problems such as stereo matching [131] [81] [33] [104][150], optical flow computation [87] [24], and image registration [48] [107] [31]). Nevertheless, a direct application of these methods for horizon matching is impractical. The stereo-matching and the rigid image registration algorithms are not applicable due to the non-linear nature of the fault displacements and local distortions. Nonrigid transformation approaches, such as polynomial wrapping [192] and thin-plate splines [159], do not accurately describe the fault deformations. The seismic intensity information is not dense enough to guide the utilization of optical flow.

Post-fault configurations imaged by the seismic data do not provide the complete information about the pre-fault configuration of horizons [14] [5] [6]. As true matching solutions can never be determined directly from seismic data (unless the faulting produces zero offsets of horizons), different solutions are possible. Seismic data interpreters select the optimal matching solution based on geological reasoning, in addition to similarities of the observed seismic amplitude features. Therefore, any automation algorithm should consider additional non-observed geological information.

The additional non-observed geological knowledge consists of general knowledge about rock layers and their mapping into 3D seismic data, and patterns of fault offset distributions. The knowledge is :

- Horizons must not cross at faults.
- Some horizons may not have matches in either side.
- Scale differences between horizons on either side are expected.
- A functional approximation of the fault throw function can be derived from the empirical fault throw model of [181].

From the previous work [14] [4] [5] [6] and manual interpretation procedures, the following observations are made :

- Matching horizons show similar amplitudes; however, it should not be used alone to make matching decisions. Several rock structures could give rise to a similar seismic observation.

- The search for an optimal solution should employ a multi-resolution strategy on a semantic scale space. On a coarse scale only very prominent signals should be matched that provide initial conditions for matching at finer scales.
- The matching decision should be made by evaluating the information on several seismic slices (3D).
- Exhaustive search among all possible solutions is impractical.

Regarding horizons, the trace line for each horizon is defined as the intersection of the horizon surface with the fault surface. However, the horizon surfaces are not well defined near the fault plane for the following reasons :

- The fault surface is just an approximation of the potentially curved fault damage zone.
- The geological nature of the fault (which could be a 3D) rises to the seismic data distortion.
- Usually, the horizons show a bent near to the fault surface, which could mislead the fault throw computations. That means that the apparent separation of the horizon surfaces could lead to errors in fault throw computation.

In the following section, the horizon matching problem is posed as optimization-based vision problem, and the relevant knowledge is integrated in a stochastic framework. Inferences about candidate matchings are obtained by sampling from this model conditioned on seismic feature gathered from both sides of a fault.

6.3 Representations

We can represent a fault patch as a 3D scene $S_d = (V, F)$, where $V \subseteq \mathbb{R}^3$ indicates the space covered by the seismic survey and F is a real-valued scalar field, such that

$$F : V \rightarrow \mathbb{R}. \quad (6.1)$$

For $v \in V$, $v = (x, y, z)$ denotes a position in seismic data of seismic inline (x), cross-line (y) and time line (z). F assigns to v a seismic amplitude value $F(v)$. Additionally, to represent the geometries of the fault and the horizons, we can define another space $S_p = (V, \Gamma)$, such that

$$\Gamma : V \rightarrow L, \quad (6.2)$$

where $\Gamma(c) = \tau$, for $\tau \in L = \{F_p\} \cup H_f \cup H_h \cup \{0\}$. Here, L is the set of labels, where F_p is a label for fault surface voxels, and $H_f = \{H_{f1}, H_{f2}, \dots, H_{fn_f}\}$ and $H_h = \{H_{h1}, H_{h2}, \dots, H_{hn_h}\}$ are respectively a set of labels for horizon surfaces from foot- and hanging-walls blocks. Horizon labels are sorted in ascending order of their time coordinates, such that $0 < H_{f1} < H_{f2} < \dots < H_{fn_f}$ and $0 < H_{h1} < H_{h2} < \dots < H_{hn_h}$. For a voxel c , which does not belong to either the fault or the horizon surface, $T(c) = 0$. For simplicity, it is also assumed that the labels are integers so that $L \subseteq \mathbb{Z}$.

The matching problem is defined as finding m , such that

$$m = \{m_1, \dots, m_i, \dots, m_k\}, \quad (6.3)$$

where $m_i = (H_{fp_i}, H_{hq_i})$ with $1 \leq p_i \leq n_f$ and $1 \leq q_i \leq n_h$ represent a matching pair, which joins horizons which would have been continuous had the fault not been present. Searching is conducted to find an optimal matching solution, which correlates to the observed seismic information and prior geological knowledge. Reasonable geological expressions are obtained only after the global matching has been determined. This complicates the matching problem, as local matching decisions do not necessarily lead to the optimal solution.

6.4 Horizon Matching as Marked Point Process

In order to select the optimal matching solution, we need to define a function which maps a set of matching pairs into measures of optimality. This function is designed under a stochastic framework defined by a marked point process (MPP) [163]. The object model properties of marked point processes make it a favorable choice for modeling matching horizons. Its stochastic nature allows us:

- to model the knowledge we have on the patterns of fault displacements on the fault surface.
- to sample and to optimize a density of configurations of matching pairs with a Markov Chain Monte Carlo Sampler and a stochastic annealing.

The Marked point process (MPP) is an approach of the Bayesian-based image analysis [19] [148]. The MPP framework has been previously applied for crater detection in remote sensing images [102], clustering [161], building outline extraction from digital elevation models [133], and object recognition [148].

6.4.1 Marked Point Process

A point process X on K is defined as a measure map

$$X(\xi) = \{x_1, \dots, x_i, \dots, x_1\}, x_i \in K, \xi \in \Omega, \quad (6.4)$$

from a probability space (Ω, F, P) to the measure space of a bounded set K . Let Y be a point process on $T \subseteq \mathbb{R}^d$, given some space M , if a random mark or attribute $m_\xi \in M$ is attached to each point $\xi \in Y$. Then

$$X = \{(\xi, m_\xi) : \xi \in Y\}, \quad (6.5)$$

is called a marked point process with points in T and marks space M . For detailed reference of marked point process, see [72][124] and the references therein.

This thesis deals with Poisson point processes. Poisson point processes are the basic tool of the spatial point processes theory and popular in image analysis [124][79] [20]. The advantage of them are their suitability in modeling natural scenes, and they provide tractable model classes. A Poisson point process is defined on a space $T \subseteq \mathbb{R}^d$ and specified by a so-called intensity function $\mu \rightarrow [0, \infty]$ which is locally integrable. Under some conditions detailed in [124], it is possible to define a point process X by specifying its probability distribution by a density with respect to a reference Poisson Process. Suppose a reference Poisson Process is defined by intensity function $\mu(\cdot) \rightarrow [0, \infty]$, and a point process X is defined by a density $f(\cdot)$, then for a real parameter Z , we can set

$$Z = \int_{\xi} \beta^{n(\xi)} f(\xi) d\mu(\xi). \quad (6.6)$$

Here, β is a scale factor and $n(\xi)$ is the size of ξ . It is possible to build a Markov Chain that converges to the distribution of X which can be written in its Gibbs form as

$$f(\xi) = \frac{1}{Z} \beta^{n(\xi)} e^{-U(\xi)}, \quad (6.7)$$

where $U(\xi)$ is the energy of a configuration [177] [132]. The lower the energy $U(\xi)$, the more probable the configuration. The estimator for the maximum density of $f(\xi)$ can be obtained under a stochastic annealing framework [73] [177][102].

6.4.2 Marked Point Process of Horizon Pairs

Let us consider a set of the matching pairs as a realization of a point process defined on the set $C = \{(H_{fi}, H_{hj}) | H_{fi} \in H_f, H_{hj} \in H_h\}$ (See Figure 6.4). Recall that H_f and H_h respectively

represent horizons from the foot- and hanging wall side of the fault. The points are ordered according to the locations given by labels of the footwall side of the matching pair. Suppose M stands for a set of marks (or attributes) associated with each matching pair, then

$$X = \{(m_1, \{T(m_1), S(m_1)\}), \dots, (m_p, \{T(m_p), S(m_p)\}), \dots, (m_k, \{T(m_k), S(m_k)\})\}, \quad (6.8)$$

$m_p \in C, \{T(m_p), S(m_p)\} \in M$, is a marked point process with points in C and mark space M . The functions T and S respectively are computation functions for fault throws and seismic features.

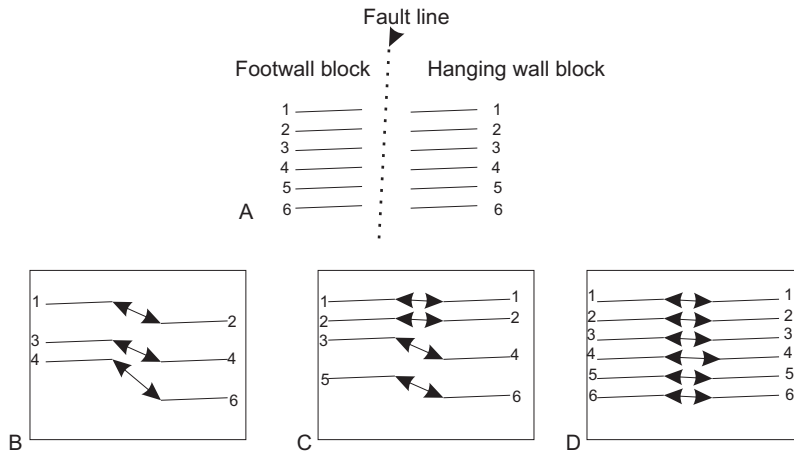


Figure 6.4: Illustration of the modelling of horizon matching as a point process. A. schematic representation of horizons defined from each side of a fault line. B. $\{(1, 2), (3, 4), (4, 6)\}$, C., $\{(1, 1), (2, 2), (3, 4), (5, 6)\}$, and D. $\{(1, 1), (2, 2), (3, 3), (4, 4), (5, 5), (6, 6)\}$ represent realizations of the point process defined on a set of horizon pairs. Each pair constitutes horizons matched across the fault line.

The match function f is defined as an unnormalized posterior density function for the marked point process. Following Equation 6.8 and Equation 6.7, the match function for marked point process m is

$$f(m) = \exp(-U(m)). \quad (6.9)$$

The energy U is defined as

$$U(m) = S(m) + A(m). \quad (6.10)$$

Here the functions $S(m)$ and $A(m)$ respectively represent energies defined for the fault throw and seismic attributes. They are described in the following sections.

6.4.3 Fault Throw Energy, $S(m)$

The fault throw energy, $S(m)$, measures the fit between computed fault throws and ideal fault throws. For a configuration $m = \{m_1, \dots, m_k\}$, the fault throw energy $S(m)$ is defined as

$$S(m) = \omega_s \frac{1}{N_F(m)} \sum_{p=1}^K \sum_{v \in T(m_p)} \left(\frac{F_{computed}(v) - F_{ideal}(v, w, D)}{\sigma} \right)^2, \quad (6.11)$$

where ω_s is a scaling factor, σ is a standard deviation, $N_F(m)$ is a normalization factor, $F_{ideal}(v, w)$ is the ideal fault throw value at voxel v , and $F_{computed}(v)$ is the computed fault throw value at voxel v . The function $T(m_p)$ is an operator to compute fault throw values for a matching pair.

Suppose $m_p = (H_{fi}, H_{hj})$, the computation of the fault throw is done as follows. Initially, the intersections of the horizon surfaces with the fault surface are computed. Horizon surfaces are dragged or bent near the fault surface locations, consequently the surfaces are extrapolated at a certain distance from the fault surface. This distance has to be determined experimentally. The voxel v is a fault surface voxel at which horizon H_{fi} intersects the fault surface. The computed fault throw $F_{computed}(v)$ is then the perpendicular separation distance (i.e, in z direction) of the voxel v from its corresponding matching voxel which is the intersection of H_{hj} with the fault surface. Figure 6.5 illustrates the computation of fault throws in 2D and 3D.

The function $F_{ideal}(v, w, D)$ is a theoretical fault throw function taken from [181] and it has the form

$$F_{ideal}(v, w, D) = 2D(((1 + r(v, w))/2)^2 - r(v, w)^2)(1 - r(v, w)), \quad (6.12)$$

where $r(v, w)$ is a normalized radial distance from the fault center and D is the maximum displacement on a fault surface. In this model, the parameter w is a vector and consists of a fault width and its center. The parameters D and w are approximated from least square minimization of an objective function

$$(\hat{w}, \hat{D}) = \min_{w, D} \sum_{p=1}^k \sum_{v \in T(m_p)} |F_{ideal}(v, w, D) - F_{computed}(v)|, \quad (6.13)$$

with respect to w and D . Then, Equation 6.11 is measured as

$$S(m) = \omega_s \frac{1}{N_F(m)} \sum_{p=1}^K \sum_{v \in T(m_p)} \left(\frac{F_{computed}(v) - F_{ideal}(v, \hat{w}, \hat{D})}{\sigma} \right)^2. \quad (6.14)$$

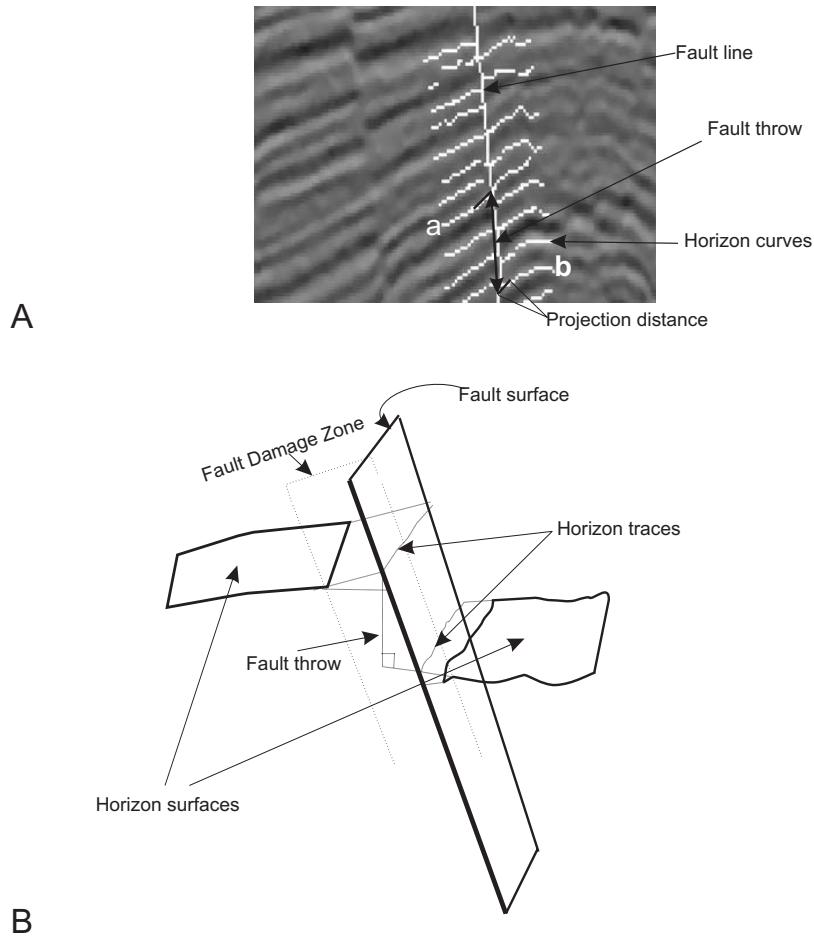


Figure 6.5: A. illustration of the computation of fault throw attribute for a matching pair (horizon a and horizon b) on a seismic inline slice. Horizon curves are extrapolated at some distance from the fault line and intersected with it. The fault throw is the perpendicular distance between the intersection points of the extrapolated horizon curves and the fault line. B. schematic illustration of fault throw attributes computation in 3D. Here the horizon surfaces are extrapolated at some distance from the fault surface (to avoid the fault damage zone). The intersection points of the extrapolated horizon surface to the fault surface form a curve, which is called the trace of the horizon or simply horizon trace.

6.4.4 Seismic Energy, $A(m)$

The seismic energy measure $A(m)$ quantifies seismic similarities between matching horizon pairs. Matching horizons represent homogenous sedimentary rock layers. The homogeneity is usually characterized in the seismic data by similar amplitude values. Horizon surfaces are not iso-surfaces [101] [146] as seismic amplitudes of horizons are not constant or exhibit constant variations. However, the strong seismic similarities on horizon surfaces should be conceived for a robust data analysis [8] [8]. The automated horizon matching approaches introduced in [15] and [3] respectively use a 1D and 2D correlation coefficient to measure the seismic similarity between two matching horizon segments. The correlation coefficient approach requires testing with different scaling and lag options. Therefore, it results in a large number of possible measuring functions and becomes intractable. A Gaussian process allows us to avoid this problem. It provides a framework for tractability and consistency.

Given a matching solution $m = \{m_1, \dots, m_k\}$, the seismic energy $A(m)$ is derived as

$$A(m) = \omega_a \frac{1}{N_F(m)} \sum_{p=1}^k -\log(u(S(m_p))), \quad (6.15)$$

where ω_a is a scale factor, N_F is a normalization factor, and u is a probability density of the Gaussian process defined on seismic attributes. The function $S(m_p)$ computes seismic features for the matching pair. It consists of two functions $s_{fp}(v_{fi})$ and $s_{hp}(v_{hj})$. These two functions are averaged seismic amplitudes along horizon surfaces H_{fi} and H_{hj} . The arguments v_{fi} and v_{hj} are, respectively, fault surface voxels at which horizons H_{fi} and H_{hj} intersect the fault surface. The seismic information is distorted at locations close to the fault because of the geological process of fault creation. To correct for this data distortion, averaging along the surfaces starts at a certain distance from the fault surface. The average features are projected to the intersection points obtained by extrapolating the horizons surface to intersect the fault surface. Figure 6.6 illustrates the computation procedure.

The maximum likelihood estimate of u with zero mean is obtained as,

$$u(S(m_p)) = u(s_{fp}(v), s_{hp}(v)|l_{min}, l_{max}) \simeq \exp\left(-\sum_{l=l_{min}}^{l_{max}} Var_{avg}(l)\rho(l)\right), \quad (6.16)$$

where $Var_{avg}(l)$ is an average variance for lag l , $\rho(l)$ is an exponential weighting function, and l is a distance between points of the seismic attributes. The parameters l_{min} and l_{max} specify

the range of the lag distance and spatial dependence. More complex likelihood estimators of the Gaussian process are found in [76] [144].

The lag distance is required to impose the spatial correlation of the Gaussian process, and it is computed as a block distance on the hanging wall horizons. Figure 6.7 illustrates how the lag distance is estimated. Mathematically, the lag distance is

$$l = \|v_{fi_z} - v_{hj_z}\| - T_p(v_{fi}), \quad (6.17)$$

where v_{fi_z} and v_{hj_z} are the z -coordinates of v_{fi} and v_{hj} . Recall that for $m_p = (H_{fi}, H_{hj})$, v_{fi} and v_{hj} are fault surface voxels at which horizons H_{fi} and H_{hj} intersect the fault surface. The subtraction by the fault throw function, $T_p(v_{fi})$, is to remove the effects of the fault throw on spatial correlation.

The exponential weighting function $\rho(l)$ in Equation 6.16 imposes a priori smoothness, and has the form

$$\rho(l) = \frac{1}{c} e^{-|l|^a}, \quad (6.18)$$

where a and c are positive real values and respectively specify the correlation length and scale. These parameters are estimated by experimenting (through simple guess and check). Additional works using the exponential weighting function for heterogenetic media modeling are found in [1] [89] [68] [69] [57].

Figure 6.8 illustrates how the seismic energy is measured. On this figure, A shows an inline slice with fault patch regions. The white curves indicate the fault line and horizons tracked within the fault patch region. The dark lines connect matching horizon pairs. Figure 6.8B-E illustrates plots for different values of the parameters length (a) and scale (c). The blue (1) curves are plots for average variance versus lag distance for the matching pairs shown in Figure 6.8A. The red (3) curves are plots of the exponential correlation function for different parameters. Note that the function decays with larger lag distance, since less smoothness is expected as the lag increases. The green (2) curves represent the product of the red and blue curves. The seismic energy measure is derived as the sum of the area under the green (2) curve for a given lag range.

Combining Equation 6.15 and Equation 6.16, the seismic energy is calculated as,

$$A(m) = \omega_a \sum_{p=1}^k \sum_{l=l_{min}}^{l_{max}} Var_{avg}(l) \rho(l). \quad (6.19)$$

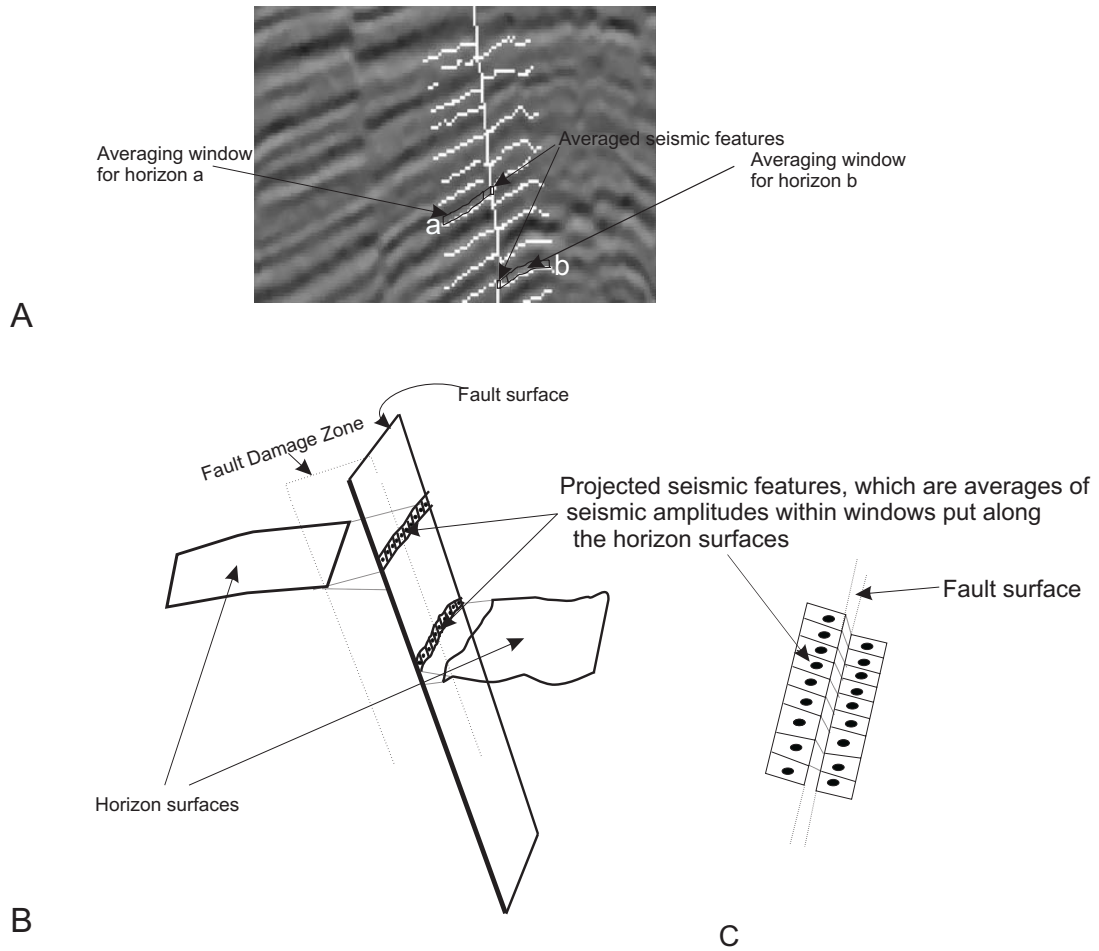


Figure 6.6: A. illustration of seismic attribute computation for a matching pair on a seismic inline slice. Seismic amplitudes are averaged within a window put along horizon curves at a distance from the fault line. The averaged seismic features are stored at the intersections of the projected horizon curves and the fault line. B. schematic illustration of the computation of seismic features in 3D. The averaging windows are put at some distances from the fault surface in order to avoid the fault damage zone. C. top view of the projected seismic features from each horizon forming the matching pair.

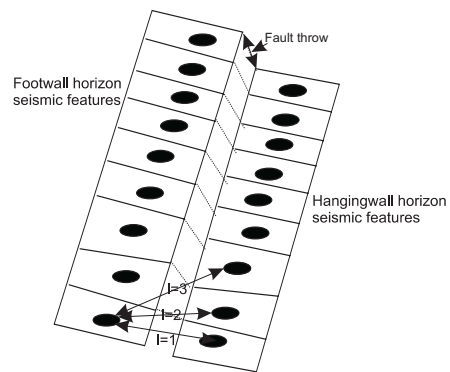


Figure 6.7: Top view of a schematic representation of a seismic attribute associated with a matching pair. The matching pair is formed by horizons defined from the footwall and the hang-wall side, and its seismic attribute consists of their combined seismic features. The seismic attribute is a realization of a Gaussian process with spatial correlation defined anisotropically with a lag distance. The lag distance is the horizontal block distance ignoring the vertical separation. The symbol l on the arrows stands for a lag distance.

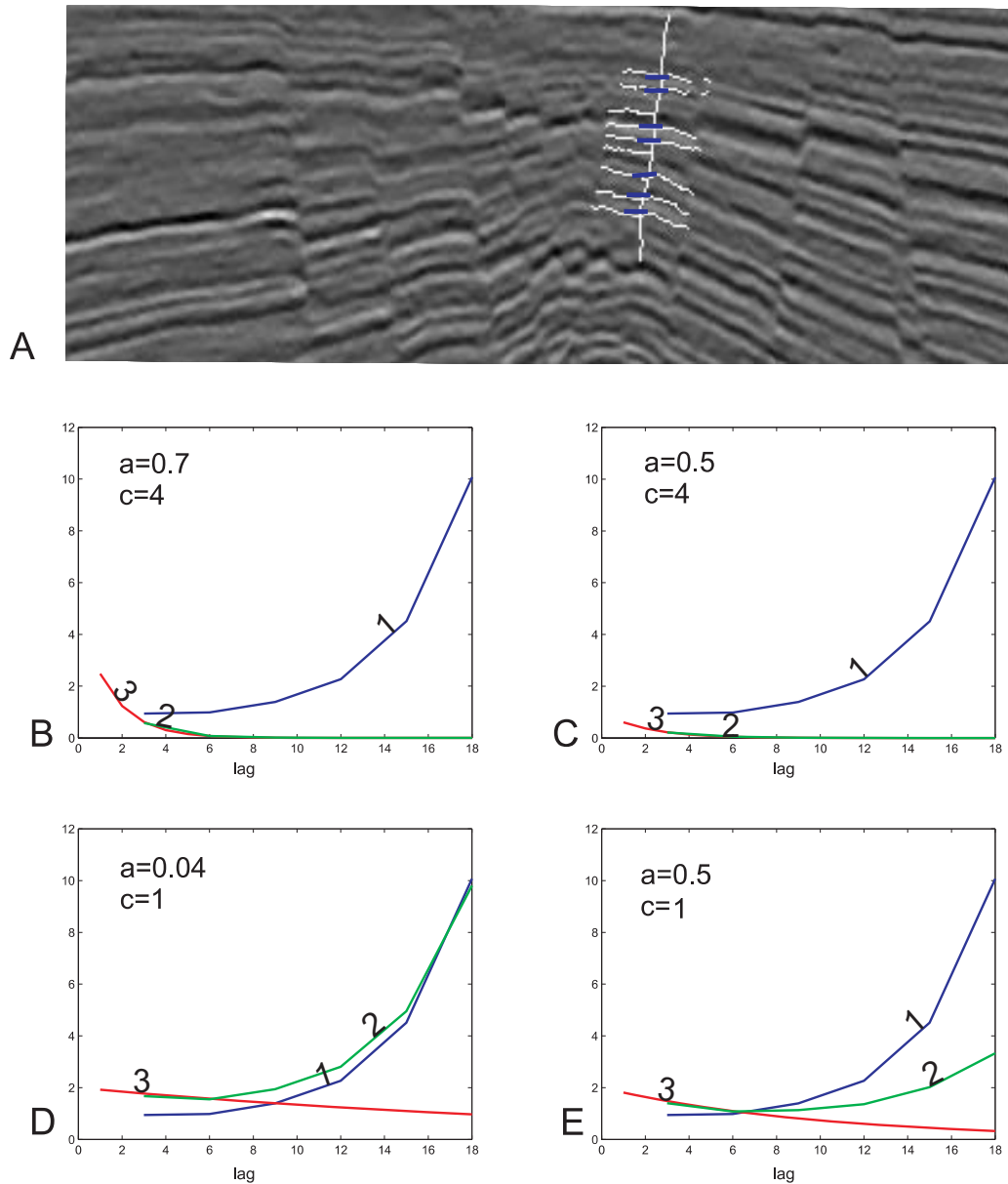


Figure 6.8: A. inline slice with a fault patch region. The white curves indicate the fault line and horizons tracked within the fault patch region. The blue (or dark) lines connect matching horizon pairs. B to E illustrate plots derived for different values of a correlation length (a) and scale (c). The blue (1) curves are plots of average variance versus lag for seismic attributes associated with the matching solution shown in A. They are independent of the parameters and so remain the same. The red (3) curves are plots of the exponential correlation function versus lag distance for the different values of a and c . The green (2) curves represent the product of the blue (1) and the red (3) curves.

6.5 Optimal Matching Solution

In the previous sections, a set of matching pairs is modeled as a marked point process configuration whose density serves as the matching function. The density function attains its maximum at the optimal matching solution. The horizon matching problem is then a maximization problem to find \tilde{m} such that

$$\tilde{m} = \arg \max_{m \in S} f(m), \quad (6.20)$$

where S is the search space that contains all possible sets of matching pairs. It is constructed by permutations and combinations of the set $C = \{(H_{fi}, H_{hj}) | H_{fi} \in H_f, H_{hj} \in H_h\}$, respectively. Recall that H_f and H_h represent horizons from the foot- and hanging wall side of the fault. The construction involves defining MPP configuration and computing the mark attributes.

The problem of computing Equation 6.20 is the large number of possible solutions for $f(m)$. The search space S is too big for a direct search. Its size is estimated as $|S| \simeq \sum_{d=1}^N \binom{N}{d}$, such that $N = |H_f| \times |H_h|$, where $|S|$ denotes the number of elements in the set, S . The size of S grows exponentially as the number of horizons increases. Simple search strategies, such as gradient descent, are not appropriate because of the non-linearity existing in the search. Solutions exist that are locally satisfying, but not globally optimal.

The next chapter defines a Markov Chain Monte Carlo sampler, and develops a stochastic annealing framework which gives a global maximum of the density $f(m)$.

6.6 Concluding Remarks

This chapter deals with representation and modelling issues. A horizon matching model integrates seismic observations and geological knowledge under a stochastic framework. It operates in the 3D space of the seismic scene while the human interpreters are restricted to the 2D view. By explicitly modeling the seismic features as Gaussian random process, we get more flexibility and a way to impose the a-priori smoothness constraint. The stochastic nature of the model provides a means for quality measure so that the decision over the model will be optimal in the real world. The next chapter explains an efficient search strategy to find the optimal matching solution.

7 Automated Horizon Matching: Solution Searching

In the previous chapter, a density function is defined to map a set of matching pairs (or a configuration) to a likelihood value. The configuration which maximizes the density function is stated as the optimal horizon matching solution. This chapter explains a suitable search strategy to find the global maximum of the density function.

7.1 Global Search Optimization Methods

Searching for the optimal horizon matching solution is a global optimization problem. Various global search methods (see [88] [138] [172]) have been introduced for global optimization problems. They can be categorized into two groups: numerical methods and Monte Carlo methods. The numerical methods search for the global solution by randomization of the search space without any explicit probability distribution. Genetic algorithms [12] [70] [63] and ant-clustering [52] [164]) are members of this group. Monte Carlo techniques [147] solve optimization problems by pseudo-randomly generating a large collection of models according to the posterior probability distribution. In order to exploit the probabilistic framework under which the matching problem is defined, Monte Carlo techniques are chosen.

7.2 Stochastic Annealing

A stochastic annealing algorithm is a Monte Carlo global search method. It is a variant of simulated annealing [99], [34] and consists of successive simulation of the point process probability distribution specified by density f_T

$$f_T(m) = \{f(m)\}^{\frac{1}{T}}, \quad (7.1)$$

where T is the temperature of the process. The steps for the stochastic annealing algorithm are

1. Initialization step: set current configuration, initial temperature and final temperature.
2. Sampling step: generate a new configuration from the current configuration using a sampling method.
3. Acceptance step: accept the new configuration as current configuration based on the acceptance criteria.
4. Scheduling step: update the temperature according to the scheduling method.
5. If the temperature is above the final temperature go to step 2.
6. Output the current configuration as the optimal configuration.

After sufficient iterations for logarithmic temperature changes, this algorithm converges to the maximum of the density $f(m)$. The proof of its convergence is given in [74], [123]. At lower temperature (T), it favors only higher densities. While at higher temperature, it possibly jumps to lower densities. In addition to the temperature schedule, the sampling and the acceptance steps determine the convergence of the stochastic annealing.

The stochastic annealing algorithm is adopted to search for an optimal matching solution. Samples of matching pairs are obtained by a reversible Jump Markov Chain Monte Carlo (RJ-MCMC) sampling method [73]. As we do not know a priori the total number of matching pairs in the optimal solution, searches should be conducted by jumping between the dimensions of the configuration. The RJMCMC sampling method allows to perform such jumping. It generates artificial Markov chains that transit between states of different dimensions. Suppose m is the current state or a sample space containing matching pairs, then the transition from this state to another state is possible in either of the following two moves.

- **Birth move:** where a new matching pair m_{k+1} is selected uniformly from C , and added to the current state such that the next state is $m' = m \cup \{m_{k+1}\}$.
- **Death move:** where a matching pair m_p is selected uniformly from m , and removed such that the next state is $m' = m / \{m_p\}$.

The acceptance step also needs a criterion to accept or reject a new configuration. The acceptance criterion influences the convergence of the stochastic annealing algorithm. According to [73], a new configuration m' is accepted with probability

$$\alpha(m, m') = \min\{1, R(m, m')\}. \quad (7.2)$$

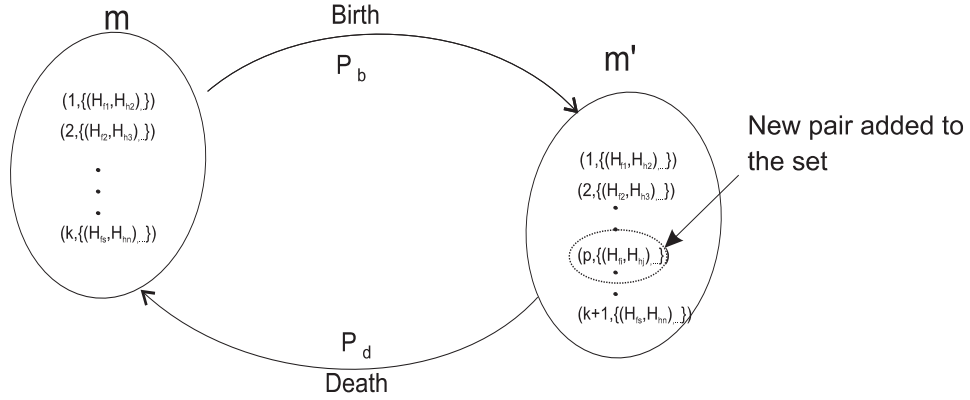


Figure 7.1: Birth and death moves. The birth move adds a matching pair while a death move removes a matching pair. The transitions are shown with arrows connecting two sets. The probabilities of the transitions (P_b and P_d) are also indicated.

The function $R(m, m')$ is a ratio function defined as

$$R(m, m') = \frac{f_T(m')q(m \rightarrow m')}{f_T(m)q(m' \rightarrow m)}, \quad (7.3)$$

where $q(x \rightarrow x')$ is the transition kernel of the Markov chain. The transition kernel depends on the move utilized to get the new state, and for the convergence of the stochastic annealing algorithm it is necessary that $q(m \rightarrow m') = q(m' \rightarrow m)$ [73]. For details of the convergence issues refer to [123, 85, 74, 176]. If the new configuration is obtained through birth move, the ratio function is written as

$$R(m, m') = \frac{f_T(m') P_d \lambda |C|}{f_T(m) P_b |m| + 1}, \quad (7.4)$$

or if it is obtained through death move, then it is

$$R(m, m') = \frac{f_T(m') P_b |m|}{f_T(m) P_d \lambda |C|}, \quad (7.5)$$

where λ is a scalar constant, $|C| = |H_f| + |H_h|$, and the symbols P_b and P_d respectively are probabilities for birth and death moves. In the experiments λ is set 0.5 and $P_b = P_d$. Higher values of λ favor the birth moves, and lower values favor the death moves.

7.2.1 Acceleration of Convergence

One of the major arguments against using the stochastic annealing algorithms is that they can be extremely slow as the number of points (in this case, horizons) increases. In order to accelerate the convergence of the annealing, the matching method uses the following three strategies.

1. Geometrical constraints

Geometrically, horizons do not cross each other (see Figure 7.2). This constrains the state transition moves, thus rather than selecting uniformly for the birth move, a matching pair is selected non uniformly only from those which do not violate this constraint. This avoids further computations.

2. **Additional state transition moves:** Two additional moves are utilized. Suppose m is a current state or a sample space containing matching pairs, then transition from this state to another state is possible with the following two new moves.

- **Footwall change move** where two matching pairs $m_{p1} = (H_{fp1}, H_{hp1})$ and $m_{p2} = (H_{fp2}, H_{hp2})$ are selected uniformly from m and their first coordinates are swapped, such that $m' = (m \setminus \{m_{p1}, m_{p2}\}) \cup \{(H_{fp2}, H_{hp1})\}$.
- **Hanging-wall change move** where two matching pairs $m_{p1} = (H_{fp1}, H_{hp1})$ and $m_{p2} = (H_{fp2}, H_{hp2})$ are selected uniformly from m and their second coordinates are swapped such that $m' = (m \setminus \{m_{p1}, m_{p2}\}) \cup \{(H_{fp1}, H_{hp2})\}$.

Correspondingly, the ratio function is defined for footwall change move as

$$R(m, m') = \frac{f_T(m') P_{hc}}{f_T(m) P_{fc}} \frac{2}{|m|} \quad (7.6)$$

and for hanging-wall change move as

$$R(m, m') = \frac{f_T(m') P_{fc}}{f_T(m) P_{hc}} \frac{2}{|m|}, \quad (7.7)$$

where P_{fc} and P_{hc} are probabilities of footwall and hanging-wall change moves respectively. These additional moves avoid waiting for a death move followed by a birth move to interchange the components of a matching pair. The state transition moves are made uniformly distributed, such that $P_b = P_d = P_{hc} = P_{fc}$.

3. A multi-resolution search

Under a multi-resolution horizon matching strategy, strong horizons are matched at a coarser level and their matchings are utilized as a priori information for matching at a finer level. The terms strong horizons and weaker horizons refer to a multi-scale representation from both sides of the fault. This is similar to standard practices for speeding up the simulated annealing by selecting results from some previous runs as initialization. More detailed explanations about the hierarchical representation of horizons and the multi-resolution search are given in a separate section below.

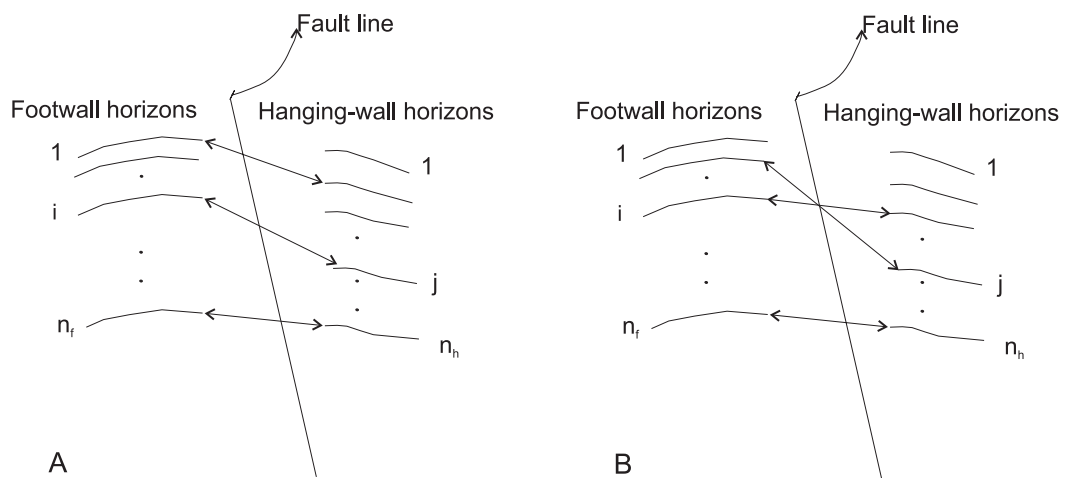


Figure 7.2: Horizons should not cross each other. Therefore, the matching configuration on B is not acceptable.

7.2.2 Multi-resolution Representation and Search

Different multi scale representations, such as wavelet analysis [112] and scale space analysis [105], have been proposed in literature. The wavelet analysis procedure adopts a wavelet prototype function, and expresses the original signal as linear combination of the wavelet function. The multi-resolution representation of the signal can then be obtained by truncating the coefficients of the wavelet expansion at different thresholds. The scale space analysis represents signals from coarse to fine levels of detail by convolving it with a Gaussian kernel whose standard deviation plays the role of scale.

The potential of the wavelet based analysis for multi-scale horizon representation was investigated in previous work of the author [3]. A fault surface was approximated as a plane, and the local seismic features were averaged in 10 pixels size along local edge directions. The average features from each side of the fault were mapped to the fault plane resulting in two 2D feature

planes (see Figure 7.3A and B). Multi-resolution behavior was obtained from the wavelet decomposition of the two fault features images using Daubechies wavelets [50]. Figure 7.3 shows the result of the continuous 1D wavelet coefficients using Daubechies wavelet on features images.

According to [3], a multi-resolution strategy was necessary to come to an adequate resolution. For example, the correspondence analysis between Figure 7.3A and Figure 7.3B became faster when the analysis was started from the coarser level and go to the finer level. This strategy works without defining a procedure for computing levels of perceptual resolution. It is also computationally expensive and not sufficiently robust with respect to noise and artifacts in seismic data [9].

In this thesis, the conceptual basis of the multi-scale horizon analysis is made in the semantic scale space, ‘strong’ and ‘weak’. This avoids errors in estimating proper levels of the perceptual space in the wavelet based scale analysis. A multi-scale function that maps a semantic scale into a likelihood value is developed. The function calculates the likelihood which determines if horizon seismic features are Gaussian processes with an exponential weighting function (see Equation 6.16).

Suppose Ω_{H_f} is a scale space function for a set of horizons from the footwall side (H_f), then

$$\Omega_{H_f}(\delta) = \{H_{fi} | H_{fi} \in H_f, u(s_{fp}(v), s_{fp}(v)) \geq \alpha(\delta), \} \quad (7.8)$$

where δ is a scale parameter and $\alpha(\delta)$ is a threshold value associated with the scale parameter. The function u is same as the one in Equation 6.16 in Chapter 6. It estimates the maximum likelihood

$$u(H_{fi}) = u(s_{fp}(v), s_{fp}(v)) \simeq \exp\left(-\sum_{l=l_{min}}^{l_{max}} Var_{avg}(l)\rho(l)\right), \quad (7.9)$$

where the likelihood estimate is for a single horizon H_{fi} . Also by definition,

- $\Omega_{H_f}(1) = H_f$ and
- $\delta_2 \geq \delta_1$ follows that $\Omega_{H_f}(\delta_2) \subseteq \Omega_{H_f}(\delta_1)$.

The hierarchical representation of a set of horizons is then obtained by varying the likelihood value of the Gaussian process. At a coarser level, few horizons with higher likelihoods are considered. At a finer level, the threshold for the likelihood decreases and more horizons are considered. Figure 7.4 illustrates the multi-scale representations of horizons from the footwall

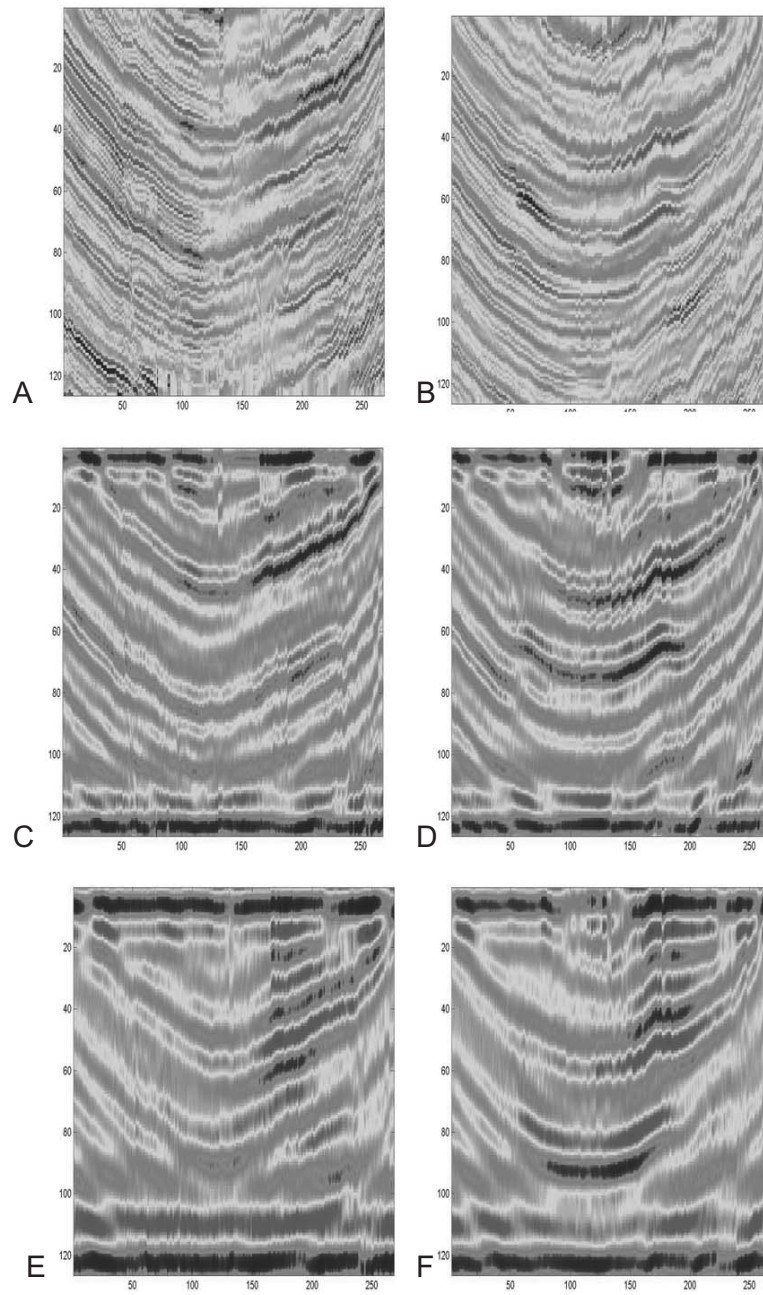


Figure 7.3: Wavelet decomposition: A and B show the footwall and the hanging-wall side-side fault feature images. C and D respectively are decompositions of A and B at coarse level. E and F respectively are decompositions of A and B at coarser level. Taken from [3].

side. In this figure, three multi-resolution levels are defined with thresholds of $\alpha(\sigma) = 0.8$, $\alpha(\sigma) = 0.6$, and $\alpha(\sigma) = 0.43$. As threshold decreases, more horizons are added.

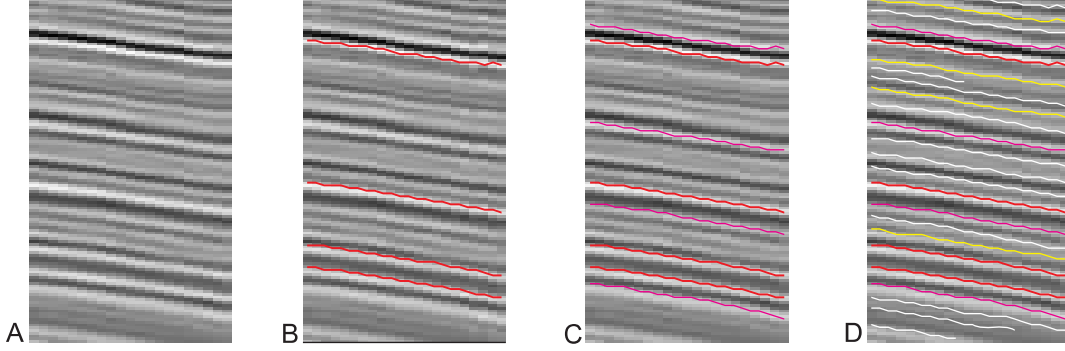


Figure 7.4: Multi-resolution representation of horizons. A. A slices taken from the foot wall side of the fault. B. A coarse resolution level for parameter $\sigma = 3$. At this level only the highlighted horizon geometries are considered. C. Next resolution level for parameter $\sigma = 2$. More horizons are added as the likelihood threshold goes down. D. Finer level for parameter $\sigma = 1$. Less strong or subtle horizons are added, as the likelihood threshold is low.

A hierarchical representation of horizons facilitates the stochastic annealing search algorithm. Suppose, the maximum resolution levels is σ_{max} , then the search for the global maxima of the density function $f(m)$ proceeds as follows. First, the stochastic annealing finds \tilde{s}_1 that maximizes the function $f(m)$ with respect to a state space S_1 . The state space S_1 is obtained by permutations and combinations of the set $C_1 = \{(H_{fi}, H_{hj}) | H_{fi} \in \Omega_{H_f}(\sigma_{max}), H_{hi} \in H_h\}$. Note that H_f and H_h respectively represent horizons from the foot- and hanging-wall side of the fault. Therefore,

$$\tilde{s}_1 = \arg \max_{s_1 \in S_1} f(s_1). \quad (7.10)$$

The multi-resolution representation is made only for H_f , whilst $\Omega_{H_f}(\sigma_{max})$ contains only horizons that are at the highest point of the hierarchy. At the next resolution level, S_2 is obtained by permutations and combinations of the set C_2 , which is

$$C_2 = \{(H_{fi}, H_{hj}) | H_{fi} \in \Omega_{H_f}(\sigma_{max} - 1), H_{hi} \in H_h\}$$

Then, starting from the solution \tilde{s}_1 , the solution for

$$\tilde{s}_2 = \arg \max_{s_2 \in S_2} f(s_2)$$

is searched. At this level, the state transition moves do not change the pairs which have already been matched in the previous resolution level. This continues until $\sigma_{max} = 1$.

7.3 Concluding Remarks

This chapter has described the stochastic annealing algorithm to find the optimal matching solution. The algorithm uses the stochastic framework of the marked point process and decides to transit from a solution to another solution in probabilistic terms. Additional strategies, such as multi-resolution frameworks, are introduced in order to facilitate the stochastic search. More efficiency of the search method can be achieved by pre-computing matching pair attributes before starting the annealing procedure. This reduces the computation time significantly.

The next chapter presents and discusses validation results obtained from applying the search algorithm to real 3D seismic data.

8 Automated Horizon Matching: Validations

This chapter reports experiments conducted to validate the method for automated horizon matching across a fault. Experiments were carried out to find the appropriate settings for the method's parameters, to measure the performance of the method, and to test the components of the matching model. Parameters were set by using manually obtained reference matching solutions. Acceptable solutions were defined as solutions which agree at least 80% with the reference manual solutions and do not contain any incorrect matches. The method performance was measured in terms of the definition of the acceptable solution. Additional experiments were also performed to compare the new method with previous ones.

This chapter is arranged in such way that the experimental setup is explained first followed by the parameter estimations. Results obtained from various tests are presented and discussed. Finally, concluding remarks and future works are given.

8.1 Experimental Setup

8.1.1 Experimental Workflow

Experiments were conducted with a prototype software implementing the workflow shown in Figure 8.1. The input to the work flow is a 3D seismic data volume and the output is a display of horizons matched across a fault. The fault tracking module implements the fault tracking algorithm explained in Chapter 5. After the fault tracking, a fault patch volume can be extracted. The fault patch contains the fault surface and seismic sections within specified distances from the fault surface. The horizon auto-tracking module implements the semi-automated horizon tracking procedure explained in Section 6.1. Tests reported in this chapter mainly concern the automated horizon matching method which comprises the feature computation and the stochastic annealing modules. It should be possible to use any other commercially available auto-tracker

tools to define the necessary fault and horizon geometries. The workflow was implemented in Matlab. Appendix A provides details of the work flow with screenshots of the prototype software.

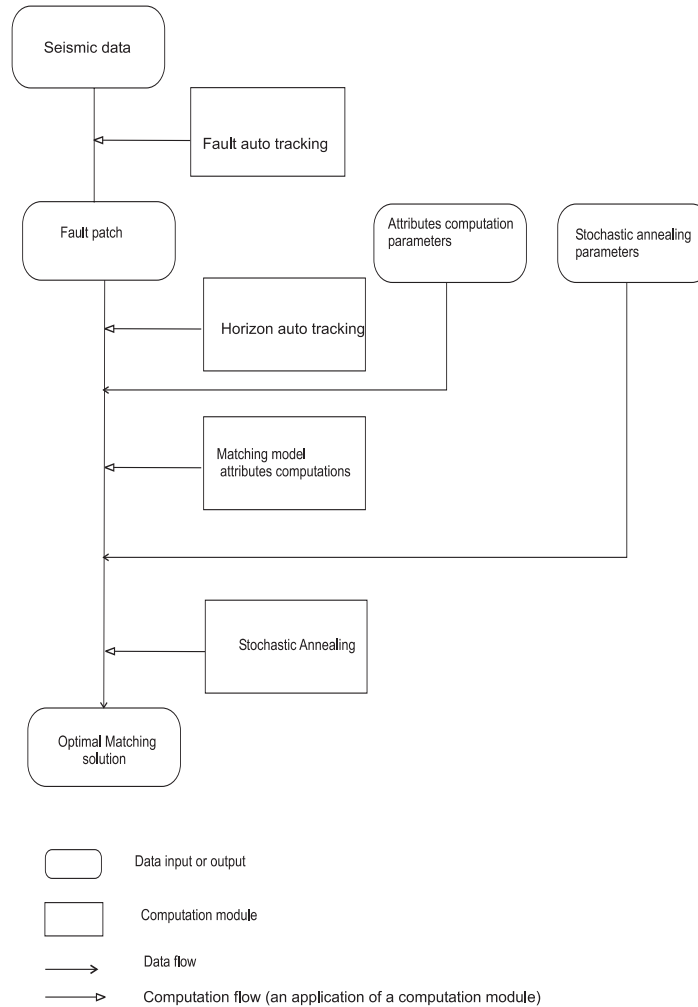


Figure 8.1: Workflow for automated horizons matching across a fault. The input for the a workflow is a 3D seismic data volume and the output is the display of matched horizons resulting from the application of the stochastic annealing algorithm. The fault auto-tracking is applied directly to the seismic volume to define a fault surface, and then the associated fault patch is extracted. The horizon auto-tracking procedure is applied to define horizon surfaces within the fault patch. Seismic features are computed for each horizon surface and passed to the stochastic annealing algorithm.

8.1.2 Test Data

The validation was conducted on four seismic data sets provided from SHELL for research purposes. These data sets are subsets of bigger surveys and their characteristics are given in Table 8.1. Each data set corresponds to a specific geographical location. The data sets have different resolutions and scales as specified in the table. Each data set is time-migrated and consists of several faults and fault systems. Previews of these data sets are shown in Figure 8.2 and 8.3.

Table 8.1: Characteristics of test data sets. The symbols s and m, respectively, stand for seconds and meters.

Dataset name	Voxel resolution			Voxel scale			Bit/voxel
	zsize	xsize	ysize	zscale(s)	xscale(m)	yscale(m)	
Ma_seis	376	101	601	4	25	25	8
Forcados	626	401	401	4	12.5	12.5	8
Swamp	126	401	401	4	25	25	8
Sbar	151	401	51	3	12.5	12.5	8

Totally, twenty-eight faults were selected from these data sets. Eight faults from Ma_seis, seven faults from Forcados, nine faults from Sbar, and four faults from Swamp data sets. These faults were vertically oriented (above 45 degree) and were extracted approximately in the range 1 to 3.5 TWT seconds. The faults were considered as normal faults. Thus, matchings were done with the assumption that sediment layers from one side of the fault moves downward, relative to the other side. Examples of selected faults from Swamp and Forcados datasets are shown in Figure 8.4. Each data set volume is fed to the workflow shown in Figure 8.1. Fault surface coordinates were defined for each selected fault within the data volumes, and associated 3D fault patch were isolated from the data sets. Details of the extracted fault patches are listed in Table 8.2. The extent of the fault patch varies and it was specified in order to avoid any nearby faulted sections. Horizon surfaces were defined semi-automatically at each side of the fault. The last column in Table 8.2 specifies the number of horizons defined from each side of the fault. In subsequent sections, in order to illustrate both automated and reference matching results, inline slices, taken from the 3D fault patches, are utilized. An example of such inline slices is shown in Figure 8.5.

8.1.3 Solution Definition

Reference manual horizon matching solutions are defined for each fault patch. Each reference solution specifies the optimal matching solution only based on the information available within the fault patch. The reference solutions were used to estimate parameters and evaluate automatically obtained solutions.

Table 8.2: List of test fault patches.

Name of fault patches	Source data set	Voxel size (Z×Y×X)	Number of horizons defined	
			Footwall	Hanging-wall
Fault 1	Ma_seis	230x50x57	27	30
Fault 2	Ma_seis	230x50x51	20	18
Fault 3	Ma_seis	214x50x78	18	18
Fault 4	Ma_seis	233x50x70	28	26
Fault 5	Ma_seis	212x50x56	22	28
Fault 6	Ma_seis	164x30x70	23	25
Fault 7	Ma_seis	262x50x65	23	26
Fault 8	Ma_seis	242x50x80	19	19
Fault 9	Forcados	198x50x35	29	28
Fault 10	Forcados	104x50x25	13	15
Fault 11	Forcados	97x50x22	12	15
Fault 12	Forcados	151x30x27	21	19
Fault 13	Forcados	120x40x41	15	13
Fault 14	Forcados	119x35x50	19	18
Fault 15	Forcados	147x50x65	11	11
Fault 16	Sbar	151x40x50	15	15
Fault 17	Sbar	151x35x50	13	12
Fault 18	Sbar	151x25x40	14	14
Fault 19	Sbar	120x25x40	14	12
Fault 20	Sbar	123x20x40	14	12
Fault 21	Sbar	120x25x40	12	14
Fault 22	Sbar	120x30x50	15	14
Fault 23	Sbar	140x30x50	12	12
Fault 24	Sbar	150x40x50	13	14
Fault 25	swamp	113x25x60	16	16
Fault 26	swamp	108x24x70	16	15
Fault 27	swamp	126x50x60	12	13
Fault 28	swamp	122x24x126	10	16

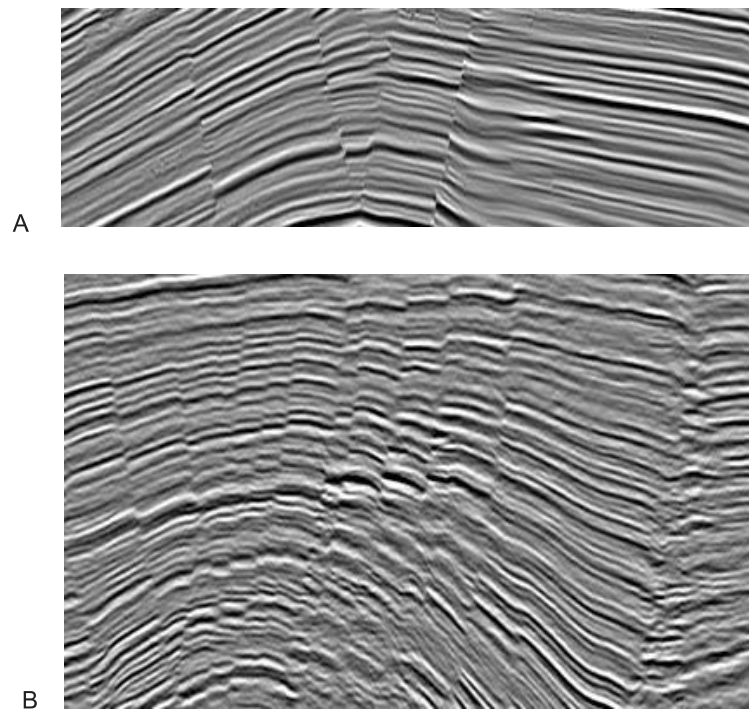


Figure 8.2: Preview of inline slices taken from A. Swamp and B. Forcados data sets.

Automated matching results from the matching work flow are evaluated as acceptable solutions, when they have at least 80% matched pairs which correspond with the matched pairs of the reference solutions, and have no incorrectly matched pairs. Therefore, the major requirement is that the automated method should not mislead the user by performing mismatches.

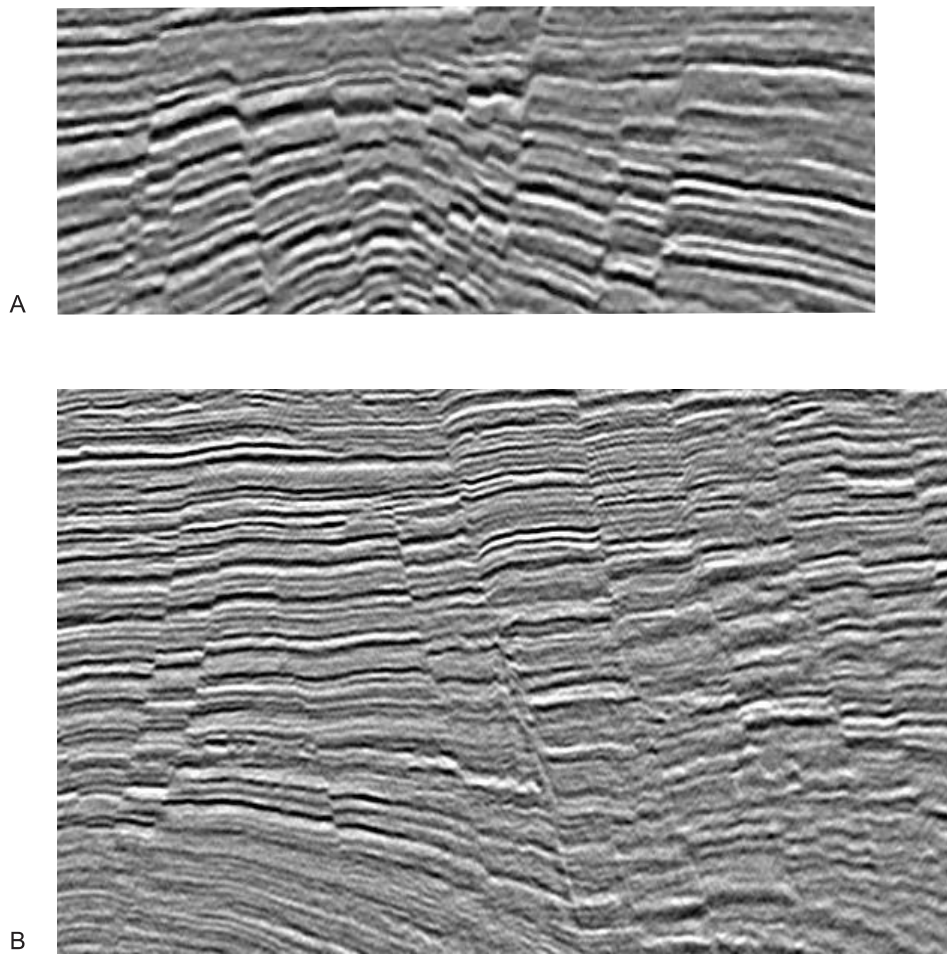


Figure 8.3: Preview of inline slices taken from A. Sbar and B. Ma_sesis data sets.

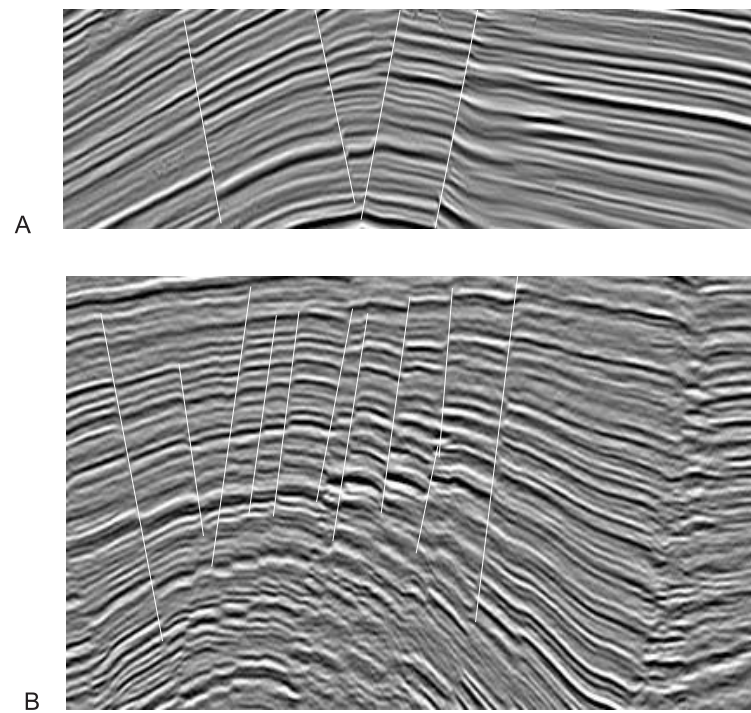


Figure 8.4: Preview of inline slices with seed fault lines A. Swamp data set and B. Forcados data set inline slices. The white lines are manually drawn seed lines for fault auto-tracking.

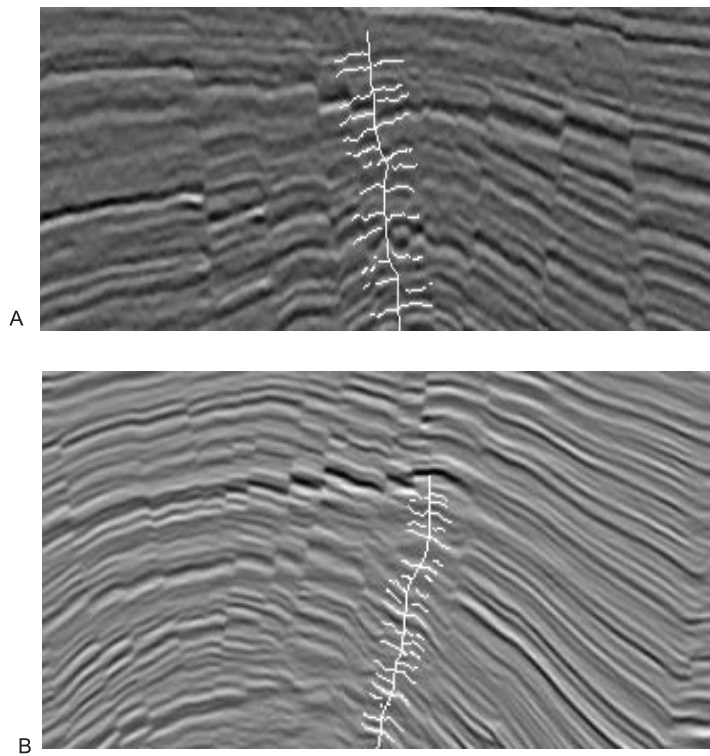


Figure 8.5: A. inline slice showing localized fault patch regions from Sbar data set. B. inline slice showing localized fault patch regions from Forcados data set. The vertical white curves indicate fault surfaces, while horizontal white curves indicate horizon surfaces crossing these inline slices.

8.2 Parameter Estimations

The horizon matching method was implemented in two stages (Figure 8.1). The first was the computation stage of matching pair attributes. This is to avoid re-computations in the annealing iterations. The second stage was the stochastic annealing where the optimal matchings of horizons are searched.

The method requires seven groups of parameters :

1. Distance of projection to compute the fault throw and seismic attributes
2. The standard deviation σ of the fault throw energy measure
3. Seismic energy measure parameters
4. Normalization constant N_F and weighting factors
5. Number of resolution level
6. Matching threshold value
7. Stochastic annealing parameters.

The first three parameters are required to compute the matching model attributes while the last four are solution searching parameters required to find the optimal matching solutions. Settings for the parameters were found using selected training faults, which were Fault 2, Fault 5, Fault 11, Fault 12, Fault 18, Fault 21, Fault 23 and Fault 27 in Table 8.2. Details of the parameters are explained below with strategies to find the appropriate settings.

1. Distance from the fault surface to compute the fault throw and seismic features

Seismic information are distorted at locations close to the fault because of the geological process of fault creation. To correct this fault distortion, feature computation should be started at some distance from the fault surface. This distance should also be close enough to the fault as not to affect the fault throw calculations. Various estimations of this distance are given in previous publications. For example, the work in [15] suggests this distance as 3 to 10 voxels from the fault line, and in previous investigations of the author [5, 3, 7], the distances were between 4 to 10 voxels from the fault surface.

In order to measure the data distortion, an experiment was conducted by using the seismic energy measure. The seismic energy of the reference solutions varies depending on the seismic features. For very smooth or similar features the seismic energy is low. Thus, in areas of data distortion, a high seismic energy is expected.

Table 8.3: Distance from the fault surface to compute attributes.

Fault length in voxels (Z)	Rule	Used in the experiments
below 100	3-4	4
between 100 to 150	5-6	5
above 200	6-8	6

In the experiment, the following seismic energy measure was utilized.

$$A(m) = \sum_{p=1}^k \sum_{l=l_{min}}^{l_{max}} Var_{avg}(l) \frac{1}{c} e^{-|l|a}. \quad (8.1)$$

This equation is similar to Equation 6.4.4, but without the weight factors. The parameters were set as $a = 0.1$, $c = 2$, $l_{min} = 1$ and $l_{max} = 6$. Starting from one voxel distance from the fault surface, the seismic energies of the reference solutions were computed. This was to determine appropriate distances from the fault surface, at which the seismic energies of the reference solutions are minimized. The appropriate distances were found to be 3 to 8 voxels from the fault surface.

In later experiments, the distance was set according to the rules in Table 8.3. For faults whose maximum length was below 100 voxels, the distance was set 4 voxels from the fault surface, and for those with 100 to 150 voxels length, the distance was set to 5 voxels distance. For larger faults with lengths above 200 voxels, the distance was set to 6. Distances closer than 3 voxels were too close to the fault regions where the seismic features are distorted. Projecting horizon surfaces at distances further than 8 voxels was too far from the fault surface and may lead to miscalculations of fault throws. For example, it may turn a normal fault throw to a reverse fault throw.

2. The standard deviation σ of the fault throw energy measure

The standard deviation σ of the fault throw energy represents the expected deviation between theoretical fault throw values and the computed fault throw (see Equation 6.14). Experiments were conducted by first estimating the theoretical fault throw function for each training fault patch. The Marquard Levenburg optimization algorithm [165] is used to find the optimal parameters for the function. Then, average differences were calculated between actually computed fault throws and the values obtained from the theoretical fault throw function.

Averages of the absolute differences between theoretical and computed fault values were found to be between 0.5 and 4. From this range, the value 1.5 was chosen in the following

experiments. Values above 4 diminish the impacts of the fault throw energy measure, while values below 0.5 impose a smoothness constraint, which is too strong.

Figure 8.6 illustrates the averaged difference estimation procedure from a reference manual matching solution. Figure 8.6 B illustrates the plot of fault throws versus fault length. The length is measured as distant from the tip of the fault line. Curve (c) is the plot of the absolute differences between the computed fault throw (Curve a) and the theoretical fault (Curve b). Since we are dealing with horizon surfaces, the fault throws are computed for each horizon trace resulting in a 3D plot as shown in Figure 8.6 C, where the computation is done for each footwall horizon trace. Curve a indicates the computed fault throws for matching pairs in A, and Curve b are plots of theoretically estimated fault throws. Curve c plots are absolute differences between Curve a and Curve b.

3. Seismic energy measure parameters

The seismic energy characterizes seismic features of candidate matching pairs. The seismic energy was calculated as in Equation 6.4.4. The correlation length (a) and scale (c) were fixed to 0.1 and 2 respectively. The minimum lag distance was always 1, and the maximum lag distance was varied to get the minimum seismic energies for the reference matching solutions of the training fault patches. It was observed that when the maximum lag was set to 6, the minimum seismic energies belong to the reference matching solutions (for the training fault patches only). Consequently, in the following experiments $l_{max} = 6$. Higher values could provide a more robust measure; however, they are computationally expensive.

4. Normalization factor N_F and weighting factors

The normalization factor N_F is required to weigh the sum of the fault throw and seismic energy measures. It correlates positively with the number of horizons, and was set to $\kappa \times C_p$, where κ is a positive constant, and C_p is the number of horizon pairs in the solution. In the experiments, κ was set to equal to the width of the fault surface. This weights the sum of the energies by the total number of horizon voxels projected to the fault surface, and thus avoids favoring small numbers of horizons.

The weighting factors ω_s and ω_a are used to balance the fault throw and the seismic energy measures. Experiments were done by setting $\omega_a = 1$, and varying only ω_s . The optimal values of ω_s , at which energies of the reference solutions were minimized, were between 0.3 and 0.6. In subsequent tests ω_s was set to 0.5.

Table 8.4 summarizes the setting rules for energy parameters, and the normalization constant.

Table 8.4: Summary of setting rules for energy parameters and the normalization constant.

Parameter	Rule	Used in the Experiments
σ of the fault throw energy	1-3	1.5
ω_s of the fault throw energy	0.3-0.6	0.5
ω_a of seismic energy	1	1
a of seismic energy	0.1-0.4	0.1
c of seismic energy	1-3	2
l_{min} of seismic energy	1	1
l_{max} of seismic energy	> 3	6
N_F	$\kappa \times C_p$	κ =Fault surface width

5. Number of resolution level

In the experiments, for each fault patch a multi-resolution pyramid was built for the foot-wall block side only. The maximum number of levels in the pyramid was set to 3 for all fault patches, except for faults from the Sbar data set, which had 2 resolution levels.

6. Matching threshold

The matching threshold is the threshold value to accept or reject a matching pair at a specific resolution level. It was set as the median of the seismic energies at the resolution. Setting a higher matching threshold value, which is above the median seismic energy, rejects correct matching pairs and leads to many unmatched pairs. A matching threshold lower than the median seismic energy may recover correct matching pairs; however, it also increases incorrect matches.

7. Stochastic annealing parameters

The stochastic annealing parameters consist of :

- a) Initial temperature (T_0)
- b) Inner loop (N_{loop}) is the number of iteration for constant temperature
- c) Change in temperature (T_{rate}) is the rate of change of temperature after each iteration loop
- d) Final temperature T_{final} is the temperature at which the annealing stops.

These parameters were fine-tuned for converging to optimal matching solutions of training faults. They were related to the computation time and fitness of the solution. The fitness

Table 8.5: Tuning rules for stochastic annealing parameters.

SA parameters	Fine tune rule	Used in the experiments
Initial temperature, T_0	> 1000	Highest seismic energy + 1000
Change in temperature, T_{rate}	$> 92\%$	97%
Final temperature, T_{final}	$= 0$	0.005
Inner loop, N_{loop}	≥ 10	$N_{loop} = \max\{n_f, n_h\}$

was measured in terms of the percentage of correct matches. Assuming some unmatched pairs could be recovered at the next finer resolution level, these parameters were set with some tolerances allowing few horizons unmatched. For each resolution level, the initial temperature was set to allow jumping from the possible highest energy to the lowest. Since the highest energy cannot be known ahead, its estimation was made by adding 1000 to the highest seismic energy. An estimate of the highest seismic energy was made by computing the seismic energy for every possible matching pair and summing the first n_f highest seismic energies. Here n_f is the the number of horizons from the footwall block.

The final temperature should be close to zero and in the experiment it was set to 0.005. The rate of temperature decrement was 97%. The inner loop was set to $\max\{n_f, n_h\}$, where n_f and n_h respectively are the number of horizons from the footwall and hanging-wall block. This allowed for sufficient iterations to sample possible candidates. Table 8.5 provides the fine-tuning rules for the stochastic annealing parameters. Figure 8.7 shows an example of a stochastic annealing run (A) which converges to the solution shown (B). The temperature decreases as the iteration number increases, and the optimal matching solution was found at the lowest energy level.

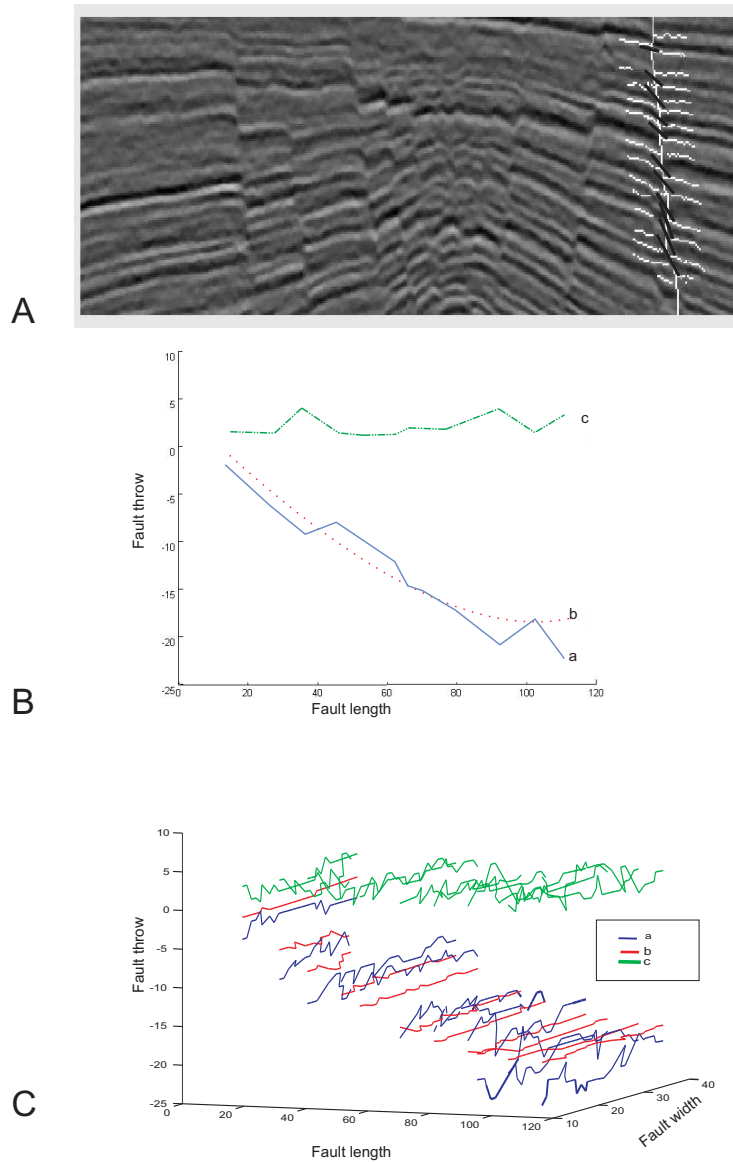


Figure 8.6: A. display of horizons matched across a fault on a seismic inline slice. B. a plot of fault throw versus fault length (distance from the tip of the fault). Curve a is the computed fault throw value, whilst curve b is the theoretical fault throw. Curve c is the absolute difference between curve a and curve b. C. 3D plots of fault throws versus fault length. Here the plot is made for each footwall horizon trace. Curve a indicates the computed fault throws over traces of horizons matched in A, and Curve b are plots of theoretically estimated fault throws at the corresponding horizon traces. Curve c plots are absolute differences between Curve a and Curve b.

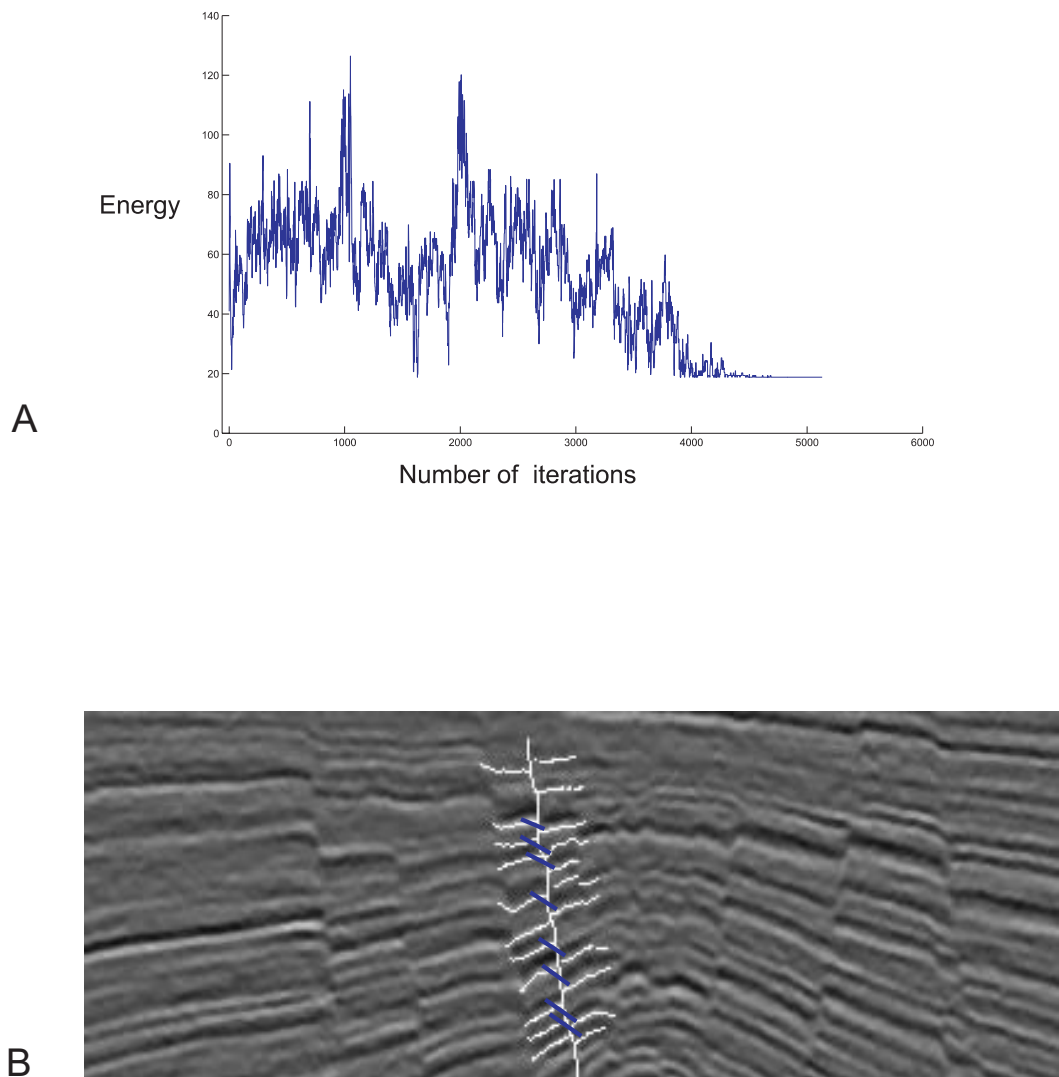


Figure 8.7: A. a plot showing a stochastic annealing run. The temperature decreases as the iteration number increases. The optimal matching solution is found at lowest energy level. B. automated matching results at the end of the simulation. The white curves indicate the fault line and horizons tracked within the fault patch region. Matching horizon pairs are connected across the fault line by dark (or blue) lines.

8.3 Results and Discussions

Tests were conducted for the following points:

1. The performance of the automated matching algorithm is evaluated. Its performance was measured for different data qualities in terms of the definition of an acceptable solution.
2. It is claimed that considering the three-dimensionality of the data directly during matching instead of relying on 2D slices improves automatic matching results. This claim was validated in terms of differences between automated results under the matching model with and without consideration of 3D spatial relationships in the data.
3. The horizon matching method employs a multi-level search strategy, where matchings on unambiguous parts of the data are made at the first level that influence decisions on later levels. This impact of the multi-level search is validated in terms of differences between automated results under a single level and a multi-resolution level stochastic annealing.
4. Additional tests were made to compare the new method with two previously published methods. The first introduces a matching method, which uses only the seismic intensity similarity to decide matching pairs. Experiment tests are conducted to show the significance of using the fault throw energy measure. The second method evaluates matching pairs by solely using the information available on 2D seismic slices. Tests were conducted to show the impact of considering more than one slice for matching decisions.

The following subsections report the results from the tests.

8.3.1 Performance of Automated Horizon Matching across a Fault

The new multi-resolution horizon matching method was applied to the fault patches in Table 8.2. The parameters were set according to the discussion given in Section 8.2. The automated matching results for each fault patch are listed in Table 8.6. The percentage of correct matches means matching pairs which are also found in the reference matching solutions. The percentage of unmatched pairs are matchings which are in the reference solutions, but are not found in the automatic matching solutions. Incorrect matches are matching pairs which are rejected in the reference solutions. The experiments were conducted on a Pentium IV PC (2GHz, 1 gigabytes RAM) running windows XP. The time necessary to match horizons of the maximum fault patch size (which was Fault 9) was 4 minutes.

Table 8.6: Automated matching results. The symbols CM, UM, and IM respectively stand for correctly matched pair, un-matched pairs, and incorrectly matched pairs.

Fault name	Percentage of CM	Percentage of UM	Percentage of IM	Acceptable
Fault 1	85	15	0	Yes
Fault 2	92	8	0	Yes
Fault 3	80	20	0	Yes
Fault 4	84	16	0	Yes
Fault 5	91	9	0	Yes
Fault 6	80	20	0	Yes
Fault 7	92	8	0	Yes
Fault 8	80	12	0	Yes
Fault 9	92	8	0	Yes
Fault 10	34	37	29	No
Fault 11	90	10	0	Yes
Fault 12	100	0	0	Yes
Fault 13	100	0	0	Yes
Fault 14	40	20	40	No
Fault 15	83	17	0	Yes
Fault 16	90	10	0	Yes
Fault 17	85	15	0	Yes
Fault 18	90	10	0	Yes
Fault 19	84	16	0	Yes
Fault 20	66	0	34	No
Fault 21	100	0	0	Yes
Fault 22	100	0	0	Yes
Fault 23	100	0	0	Yes
Fault 24	88	12	0	Yes
Fault 25	93	7	0	Yes
Fault 26	100	0	0	Yes
Fault 27	100	0	0	Yes
Fault 28	57	43	0	No

In Table 8.6, the automated matching results for 24 (out of 28) fault patches are acceptable solutions. Removing the training 8 fault patches, this reduces to 16 (out of 20). Each of the acceptable matching solution does not contain incorrect matches, and contains at least 80% of the matching pairs of the reference solutions. The average percentage of correct matching pairs of the acceptable solutions is 90%, and for un-matched pairs it is 10%. Automated matching results on 4 fault patches are not acceptable, because they contain mismatched pairs or more than 20% disagreement with reference solutions. The reasons of the failures appear to be due to a low data quality and nearby faults interactions.

The matching algorithm works well for planar faults. For example, 100% acceptable solutions were found for fault patches taken from the Ma_seis data set. The planar nature of the Ma_seis data set faults compared to faults from other data sets suits well to the fault throw model (see Figure 8.8).

Figure 8.9 illustrates horizon matching results of the horizon matching algorithm when applied to fault patches with differing data qualities. Figure 8.9A represents a relatively good data quality and the automated matching results are considered acceptable. Figure 8.9B represents a medium data quality (some distortions of horizons are visible). The matching results are considered acceptable, though there is an unmatched pair in the middle. Figure 8.9C represents a poor data quality and the matching result in this figure is not acceptable due the incorrect matchings at the bottom. Additional results showing unacceptable matching solutions are given in Figure 8.10. The automated matching solution in Figure 8.10A is not acceptable due to large number of unmatched horizons while the one in Figure 8.10B contains incorrectly matched pairs.

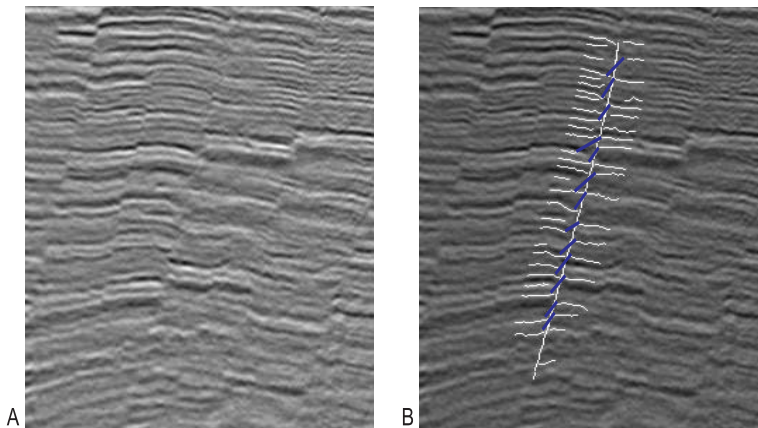


Figure 8.8: A. Inline slice showing fault patch location taken from Ma_seimi data set. B. Automated matching results for this fault patch. The white curves indicate the fault line and horizons tracked within the fault patch region. Matching horizon pairs are connected across the fault line by dark (or blue) lines.

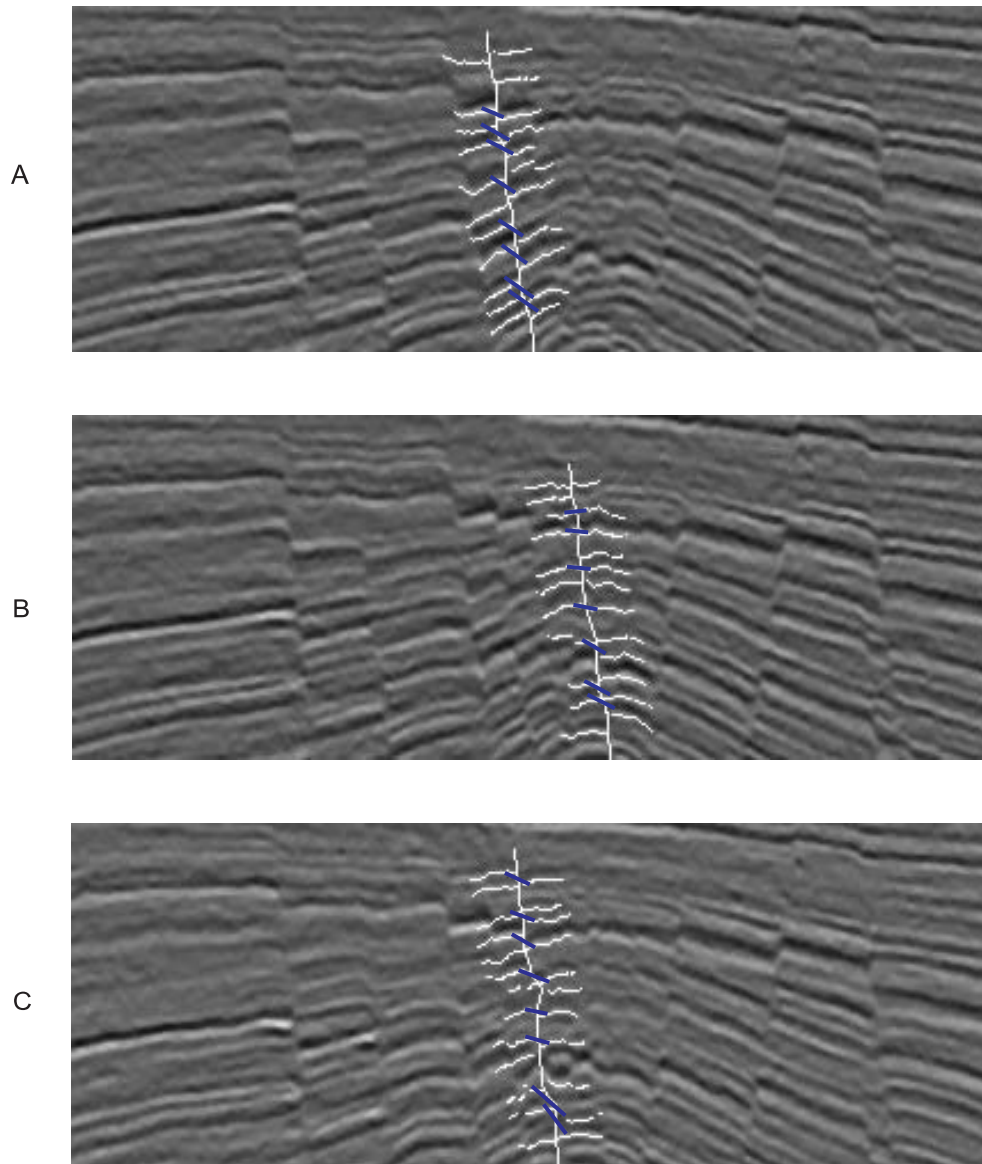


Figure 8.9: Results of the automated horizon matching with inputs of different data quality. The white curves indicate the fault line and horizons tracked within the fault patch region. The dark (blue) lines connect matching horizon pairs. A. Acceptable automatic matching results. B. Acceptable automatic matching results though horizons at the middle should be matched. C. Automatic matching results showing an unacceptable solution. Two matching pairs at the bottom are incorrect.

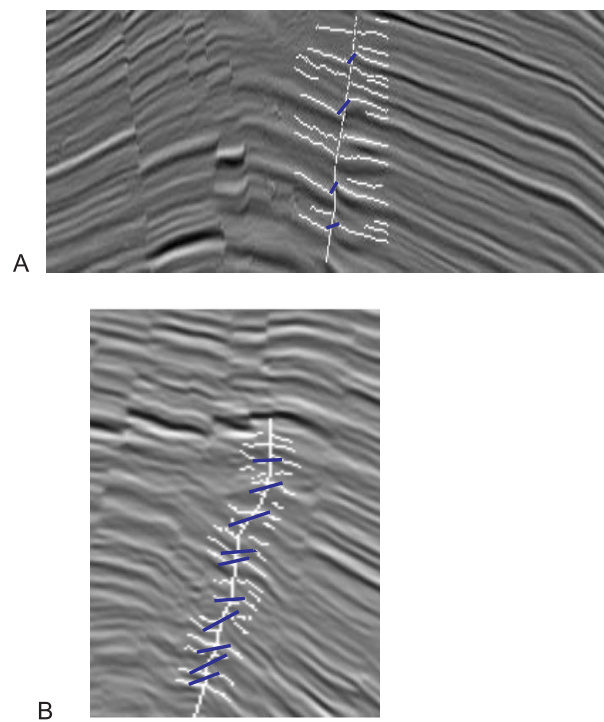


Figure 8.10: A. Automatic matching results showing an unacceptable solution. The horizons at the middle should be matched as well. B. Automatic matching results showing an unacceptable solution. The first 5 matchings from the bottom are incorrect.

8.3.2 Impact of considering 3D Spatial Relationship

Experiments were conducted to show differences between computer-assisted solutions under the same model with and without consideration of 3D spatial relationships in the data. This was done by varying the number of inline fault patch slices considered for the matching decision.

The results of this experiment are sketched on the graph shown in Figure 8.11. In this graph, the percentage was calculated over the total number of horizons defined in the test fault patches. The Correct matches plot shows that, generally, as the number of slices increases, the percentage of correct matches increases. The Un-matched plot shows two behaviors. First the percentage of unmatched pairs increases for few slices increment. Later, as the number of slices gets more, it declines. The initial increment is due to the rejection of incorrectly matched horizons. The Incorrect matches plot shows that with an increasing number of slices, the percentage of incorrect matches decreases. The big jump in percentage of the correct matches after using 10 slices is due to the rejection of incorrectly matched pairs, which opened space to recover more correct matching pairs.

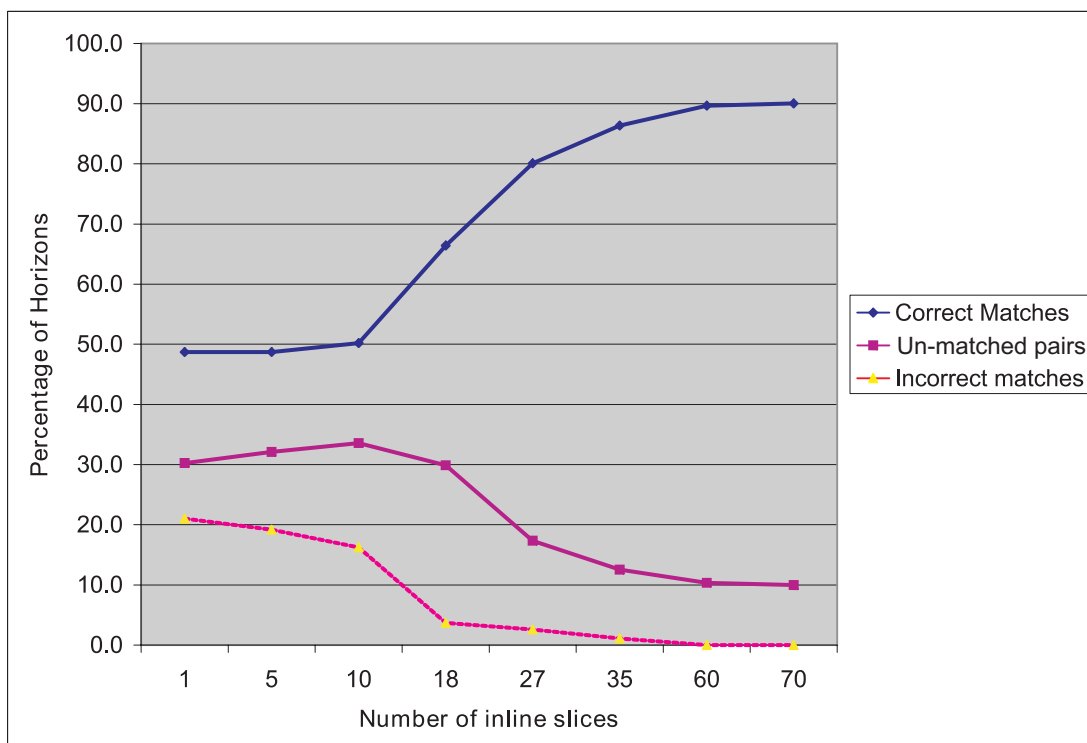


Figure 8.11: Automated matching results versus number of fault patch inline slices.

Figure 8.12 demonstrates one of the results from the experiment. In this figure, A shows an automated matching solution utilizing only the information available on the displayed inline slice. The matching solution contains mismatches and some horizons are left unmatched. In Figure 8.12B improved acceptable matching results are obtained when several slices (20) within the fault patch were considered.

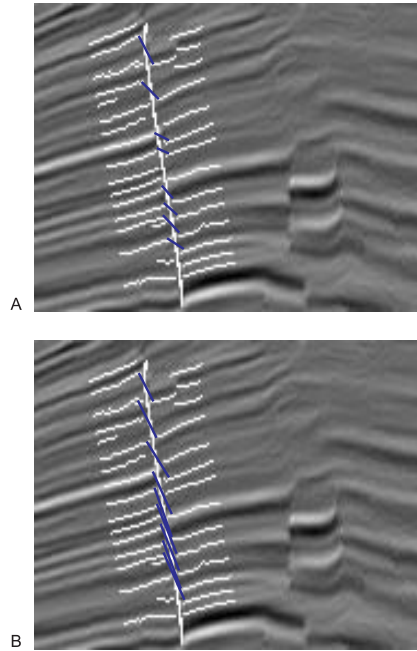


Figure 8.12: A. Automated horizon matching results obtained based on the information available in the shown 2D slice. This solution is not acceptable. The white curves indicate the fault line and horizons tracked within the fault patch region. The black (blue) lines connect matching horizons across the fault. B. Automated horizon matching results obtained when using 20 slices within the fault patch. This solution is acceptable.

8.3.3 Impacts of the Multi-resolution Search

The impacts of the multi-resolution search are measured by conducting experiments using a single resolution level stochastic annealing. This means without the multi-resolution pyramid. The results of such experiments are shown in Table 8.7. The table lists the results for the test fault patches only, and contains the results of the multi-resolution search for side-by-side comparison.

The table tells that without the multi-resolution strategy, the matching algorithm produced 12 acceptable matching solutions out of the 20 tests cases. Matching results for Fault 1, Fault 4, Fault 6, Fault 9 and Fault 13 look much better while using the multi-resolution stochastic annealing. Though there are some improvements in the percentage of correct matches, both the single level and the multi-resolution matching strategy produced the same number of acceptable matching solutions for fault patches of Sbar (Faults 25-28) data sets. This appears to be due to the lack of significant differences between the resolution levels. The fault patches from the Sbar data set had only 2 resolution levels compared to 3 in other data sets (see Section 8.2).

Figure 8.13 illustrates the impact of the multi-resolution stochastic annealing. In this figure, C shows automated matching results obtained by using a single level stochastic annealing. This solution is not acceptable because it contains mismatches. For the same fault patch, three level multi-resolution pyramid were produced, and the multi-resolution stochastic annealing algorithm was applied. Figure 8.13D, E, and F respectively show the matching results at the first level, at the second level, and at the third level of the pyramid. The matching solution at the third level is acceptable. It was also observed that the single resolution stochastic annealing took more computation time compared to the multi-resolution annealing. The maximum computation time was 7 minutes for Fault 7, but for the same fault the multi-resolution annealing took 200 seconds.

The multi-resolution search strategy was tested for potential to carry out a continuous scale matching of horizons. For each voxel from the footwall the continuous scale matching attempts to find its corresponding match on the hanging wall. In order to make such a continuous matching of horizons, first the horizon geometries were nearest neighborhood interpolated to fill every location on the fault surface. The multi-resolution pyramid of horizons was then obtained in the semantic scale space, and fed to the multi-resolution stochastic annealing. Figure 8.14 shows the result of such continuous scale matching. A direct comparison of this result with manual references was not made, because of the difficulty to do such matchings manually.

Table 8.7: Results for single level and multi-level horizon matchings. The symbols CM, UM, and IM respectively stand for correctly matched pair, unmatched pairs, and incorrectly matched pairs.

Fault	single resolution				multi-resolution			
	CM %	UM %	IM %	Acceptable	CM %	UM %	IM %	Acceptable
Fault 1	65	25	10	No	85	15	0	Yes
Fault 3	80	20	0	Yes	80	20	0	Yes
Fault 4	40	44	16	No	84	16	0	Yes
Fault 6	30	54	16	No	80	20	0	Yes
Fault 7	88	12	0	Yes	92	8	0	Yes
Fault 8	80	20	0	Yes	80	12	0	Yes
Fault 9	51	35	14	No	92	8	0	Yes
Fault 10	36	26	38	No	34	37	29	No
Fault 13	80	20	0	Yes	100	0	0	Yes
Fault 14	33	50	17	No	40	20	40	No
Fault 15	80	20	0	Yes	83	17	0	Yes
Fault 16	85	15	0	Yes	90	10	0	Yes
Fault 17	85	15	0	Yes	85	15	0	Yes
Fault 19	84	16	0	Yes	84	16	0	Yes
Fault 20	66	0	34	No	66	0	34	No
Fault 22	84	16	0	Yes	100	0	0	Yes
Fault 24	88	12	0	Yes	88	12	0	Yes
Fault 25	88	12	0	Yes	93	7	0	Yes
Fault 26	100	0	0	Yes	100	0	0	Yes
Fault 28	57	43	0	No	57	43	0	No

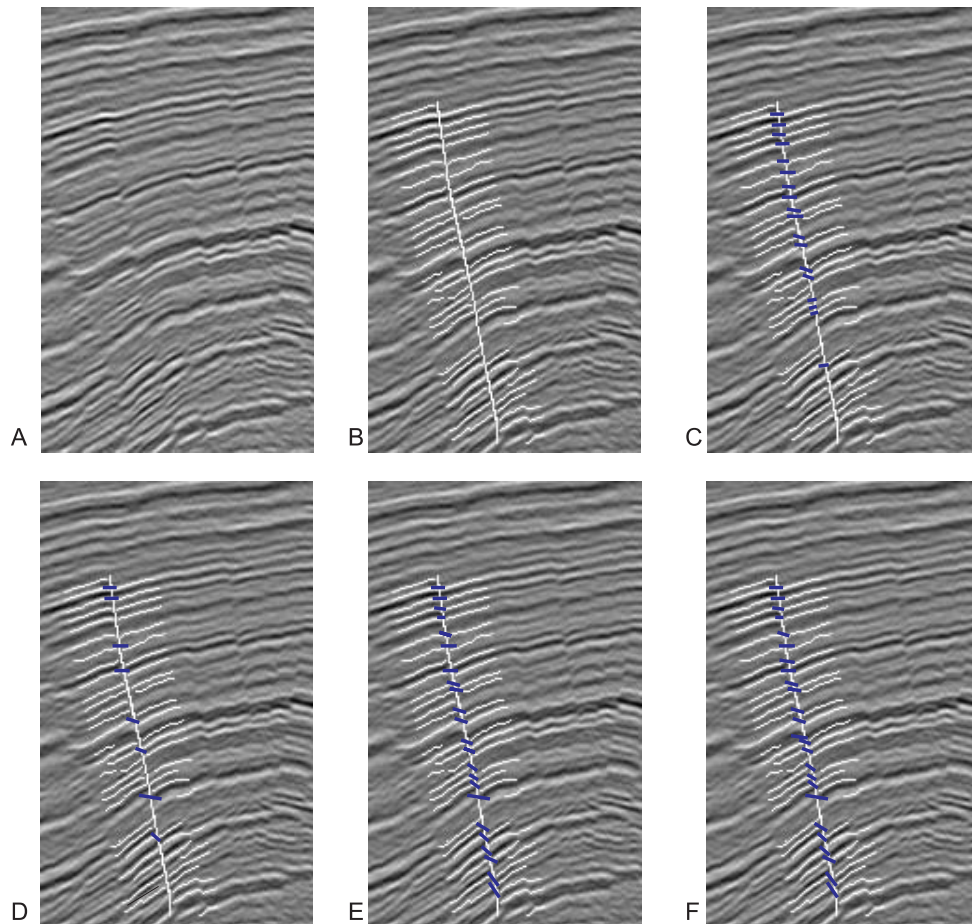


Figure 8.13: A. inline slices showing a fault patch region. B. definition of fault and horizon geometries. The white curves indicate the fault line and horizons tracked within the fault patch region. C. Automated horizon matching result obtained from a stochastic annealing without the multi-resolution strategy. This result is not an acceptable solution. The last 4 matches at the bottom are incorrect. Results of the application of the multi-resolution horizon matching at first resolution (coarse) level (D), second resolution level (E), and at third and final resolution level (F). The automated matching result at F is an acceptable solution.

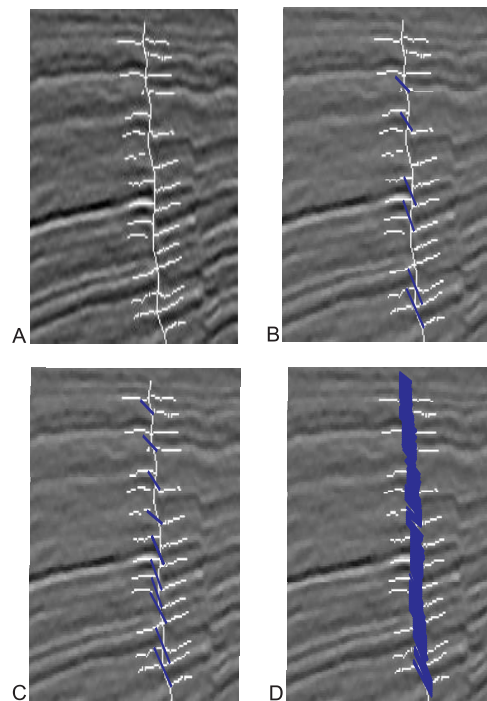


Figure 8.14: A. Inline slices showing a fault patch region. The white curves indicate the fault line and horizons within the fault patch region. B. Automated horizon matching results obtained at a coarse resolution level. C. Automated horizon matching results obtained at a finer resolution level. D. Continuous scale matching of horizons, obtained by nearest neighborhood interpolation of the horizons at C.

8.3.4 Comparisons with Previous Methods

Comparisons were done with two previous methods exclusively dealing with the matching of horizons across faults.

The first method is from [13] and it uses the seismic intensity similarity measure to match horizons across discontinuities. The method attempts to classify matching horizons by using a trained artificial neural network. The application of the method was shown with only three selected horizons.

In order to show the necessity of non-seismic information for the matching task, experiment tests were conducted by performing an automated matching without considering the fault throw energy. The tests produced 7 acceptable matching solutions for 20 test fault patches. These acceptable matching solutions were mainly obtained for faults which have relatively small offsets (for example Figure 8.15A). The number of acceptable solutions was raised to 16 when the fault throw energy was used in the matching criteria (see Table 8.6).

Figure 8.15B shows an unacceptable matching solution which was the result of the experiment conducted without incorporating the fault throw energy in the matching decision. All matchings, except the one at the top, are incorrect. An acceptable matching result was obtained when fault throw energy was incorporated into the matching (see Figure 8.16A).

An additional example showing the significance of the fault throw energy is shown in Figure 8.16B and C. In this figure, B shows an automated matching solution without the fault throw energy measure. This matching solution is not acceptable due incorrect matches at the bottom. The acceptable matching solution was achieved after incorporating the fault throw energy measure (Figure 8.16C).

The second method from [14] is a model-based scheme for the correlation of horizons at normal faults in 2D seismic images. This method exclusively uses the information in the 2D seismic slice to evaluate the geological constraints. The 2D method works only if there is enough information on a 2D seismic section and also leaves a large number of horizons unmatched. As demonstrated in Section 8.3.2, considering more than one adjacent seismic slice leads to a more robust similarity measure. The percentage of correct matches has increased from 50% to 90%, when the number of slices was increased from 1 to 70 (see Figure 8.11). Figure 8.17 compares the result of the 2D horizon matching method from [14] with the new horizon matching method of the thesis.

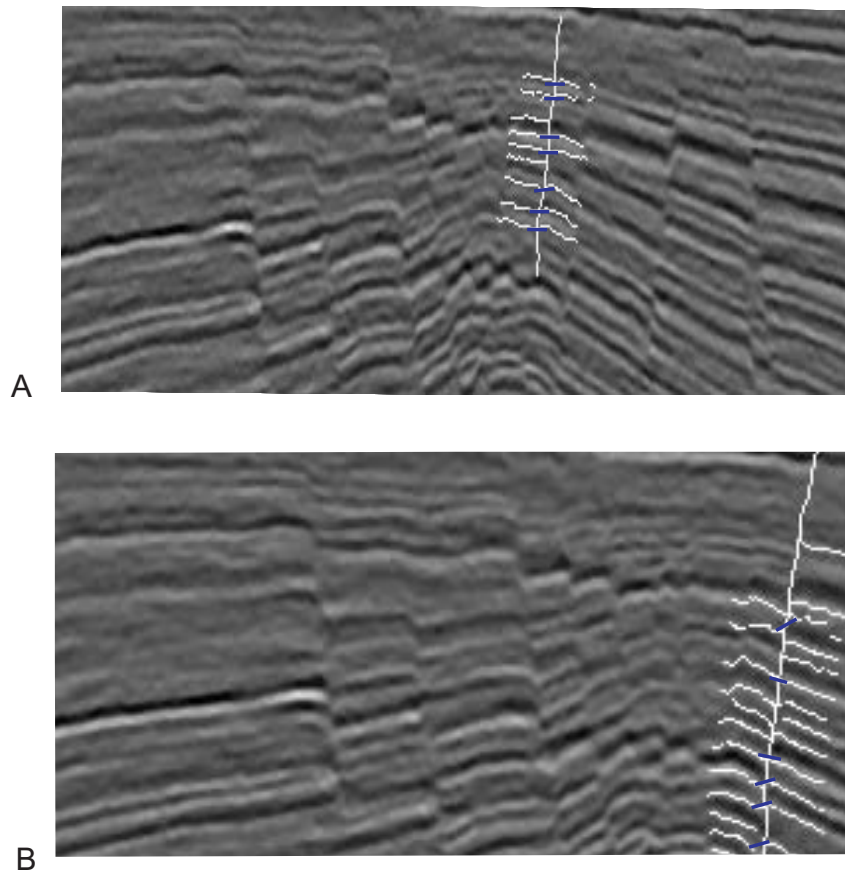


Figure 8.15: Automated horizon matching results without considering the fault throw energy in the matching criteria. A. acceptable matching solution. B. not acceptable matching solution. All matchings, except the one at the top, are incorrect.

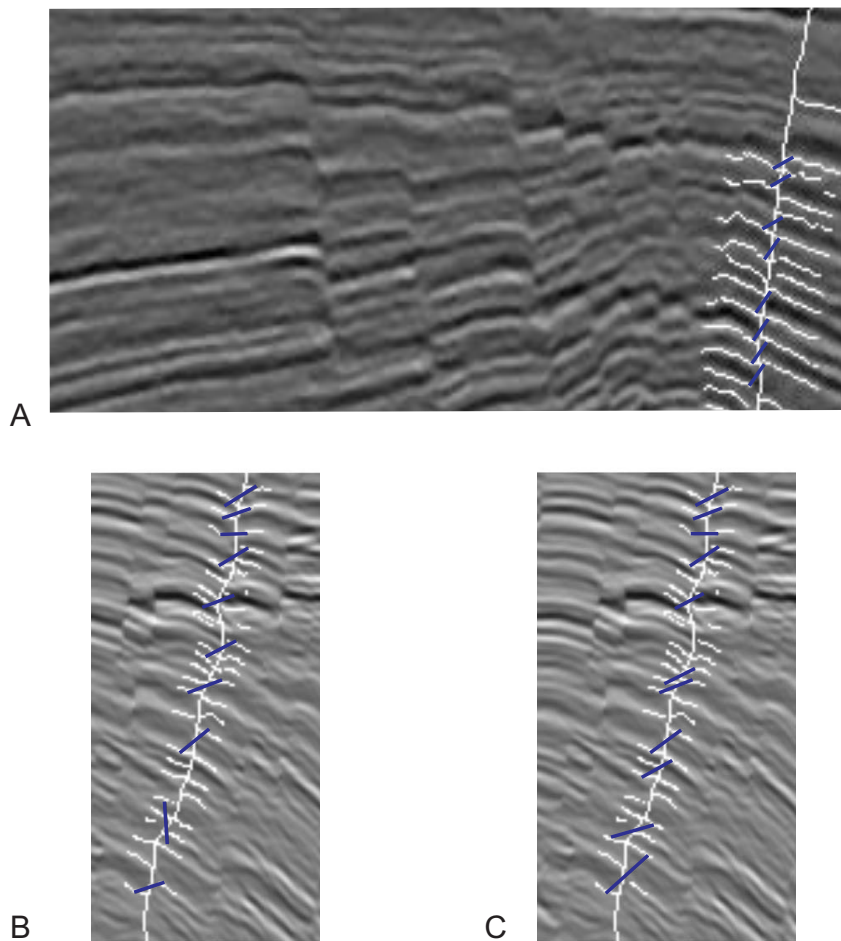


Figure 8.16: Illustration of the significance of the fault throw energy measure. A. Automated horizon matching results when the fault throw energy measure is included in the matching criteria. This is an improvement from Figure 8.15B.

B. Automated horizon matching results without considering the fault throw energy measure in the matching criteria. The two matching pairs at the bottom are incorrect.

C. Automated horizon matching results when the fault throw energy measure is included in the matching criteria. The incorrect matches from B are now corrected.

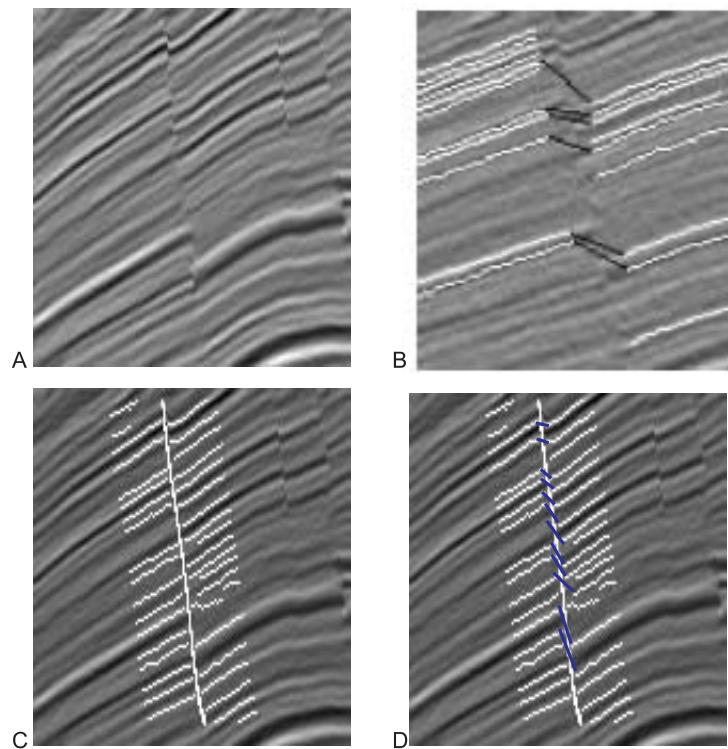


Figure 8.17: A. inline slice showing a fault patch region. B. Automated horizon matching results using the 2D matching algorithm from [14]. C. inline slice showing a fault patch region, which is the same as A, but with definitions of a fault and horizons. D. Automated horizon matching results using the new multi-resolution horizon matching algorithm. The matchings have been improved and represents an acceptable solution.

8.4 Concluding Remarks

An interpretation framework has been introduced in order to validate the automated horizon matching method. The framework, in addition to the matching method, includes auto-tracking methods for faults and horizons. The auto-tracking methods are semi-automatic while the horizon matching is fully automatic. The main focus of the validation was on the matching.

The matching process took 5 to 10 minutes starting from the fault surface extraction until the optimal matching result. This was faster compared to several hours required for manual interpretations. The automated matching results on 16 fault patches out of 20 were considered acceptable. This is a success rate of 80%. The average percentage of correct matches for acceptable solutions was 90% and for un-matched pairs it was 10% (Table 8.6).

The matching method relies on the correct definition of fault and horizon geometries. The failures for 4 fault patches were attributed to the poor data quality and interactions from nearby faults (Figure 8.10). The poor data quality affects horizon definitions, while the fault interactions distort the fault throw energy measure, which is derived from the assumption of an isolated fault. Though the method fails in such areas, it helps to bring the attention of the interpreter to these regions and saves time as the interpreter will give more attention for such areas than spending time in routine fault regions. Further, the erroneous results could also point to the incorrect fault or horizon definition, hence pointing to misinterpretations at previous stages.

The success of the horizon matching method stems from the combined effects of the fault throw energy, the integration of 3D seismic information, and the application of the multi-resolution search.

Fault throw energy : The fault throw energy measure was found to be necessary and appropriate for the matching problem. The success rate of the matching algorithm has increased from 35% to 80%, when the fault throw energy was incorporated in the matching decision. Automated matchings without the fault throw energy measure were able to recover matchings at simple discontinuities, such as those caused by noise or small fault offsets (Figure 8.15A). Though a direct comparison was not made, the results demonstrated that the new horizon matching method is more robust than the method in [13], which attempts to classify matching horizons using solely the seismic information (see Section 8.3.4).

The fault throw energy measure has worked best for isolated planar faults (see Figure 8.8), but was distorted in areas where faults were very close to each other (Figure 8.9C and Figure 8.10).

Another useful application of the fault throw energy is its use to evaluate manual interpretations. Differences between theoretical fault throw values and fault throw values from the manual interpretation could be computed and plotted for a visual analysis, for example as shown in Figure 8.6. The interpreter should use additional fault models, for example [35] [77], if it is necessary to include other fault types or fault systems.

Seismic energy: By imposing a priori smoothness over seismic features, the seismic energy allowed us to estimate the area of data distortions (see Section 8.2).

The seismic energy was evaluated based on features computed from the 3D horizon surface. The advantage of 3D is that it makes more information available for the matching decisions, compared to relying on 2D slice information. With more information, the matching method matches horizons which would not be matched, if only 2D information had been utilized (Figure 8.12).

Comparison tests were arranged with the 2D matching method from [14]. The 2D matching method extracts well-defined horizon segments on both sides of the fault and matches them based on the local cross-correlation of seismic intensity and geological knowledge. It relies on the information available in the 2D slice.

Results showed that the percentage of correct matching pairs has improved from 50% to 90%, when the number of slices was increased from 1 to 70 (Figure 8.11). The 2D method also leaves a large number of horizons unmatched compared to the 3D approach adopted in this thesis (Figure 8.17).

Multi-resolution approach: The multi-resolution search strategy achieved a success rate of 80% compared to a success rate 60% reached in a single-level horizon matching (Table 8.7). Multi-resolution representations of horizons were obtained in the new semantic scale space.

In the multi-resolution strategy, the converging to the optimal matching solution necessitates a very low number of iterations in the stochastic annealing algorithm, and a reduced amount of computation time.

The impacts of the multi-resolution approach was more significant for big faults. This was noticeable on matching results for fault patches from Forcados and Ma_seis data sets, which have bigger faults compared to Swamp and Sbar data sets. The total number of acceptable solutions for fault patches taken from Ma_seimi (Faults 1-9) and Forcados (Faults 9-16) data sets were improved after the application of the multi-resolution strategy (Table 8.7).

The multi-resolution stochastic annealing parameters were set to produce sufficiently large iterations and it was assumed that unmatched pairs can be recovered at a finer resolution. This

could result in unnecessary iterations even after hitting the lowest energy. For example, in Figure 8.7 the lowest energy was found before the final temperature was reached. This indicates some spaces to improve the computation time of the stochastic annealing by optimization of the temperature schedule. Optimal temperature schedules, such as those in [41], should be investigated to improve the efficiency of the matching algorithm.

The semantic scale space approach also provides flexibility to obtain various levels of perceptual resolution and matchings at a continuous scale (see Figure 8.14). Such continuous level matchings are difficult to do manually, and reveal additional geological information such as extents of compression and erosions of sediment layers after faulting [18].

Repeatability : Since the ultimate goal is production, seismic interpretation is done iteratively to get good reliable and consistent measures of the interpretation. The new method, based on a quantitative model, provides a repeatable and fast data analysis tool. The interpreter can easily experiment with the modeling parameters in order to make hypothesis tests.

Finding a way of building the geometric aspects of geological models, so that they can be easily modified by automated tools, is still an open problem [59][151]. This thesis matching model is not complete, but an important step ahead for the structural interpretation of seismic data based on 3D geometric primitives.

8.4.1 Future Work

Four research directions for improving the matching algorithm are envisaged. These are:

1. Prior Fault Model Extension

The current fault throw energy measure is modeled under the assumption that faults are planar. Though this assumption holds well for shallow regions, at deeper locations, it does not. Big faults with larger throw also tend to be curved.

In order to tackle the matching at such locations, the fault throw energy measure should be modified. A possible modification can be achieved by including the local structural variation into the energy measure so that the linear portion of the fault is treated differently from its curved portions. Another possibility is to divide the fault into several linear parts and do the horizon matchings by using different density functions defined at each part. The strategy to model the interactions among the different parts should be investigated.

2. Fault Interaction Model

The matching method fails in areas of fault interactions and fault systems. As fault interactions are quite common, the matching model should be extended to include them. The first possible extension with regard to this is to use fault interaction models for the fault throw energy measure. Fault interaction models, such as [160] [135] [134], are good starting points. Unlike the matching method of this thesis, which is localized to a single fault patch, human eyes are not restricted to local fault information. Interpreters use the relation between faults to make an interpretation decision. Thus, another possible extension is to extend the existing multi-resolution strategy where results from more reliable fault patches guide the interpretation of fault patches at less reliable locations. This should be defined on the entire fault patch, in addition to the multi-resolution representation at the horizon level.

3. Multi-Source Data Fusion

Different data sources are utilized for reliable subsurface interpretations. Well-log data are major additional observations assisting horizon matching. Such additional sources should be included into the matching model to calibrate or evaluate matching results. Data fusion strategies, such as the Kalman filter [96] and Bayesian networks [93], should be investigated.

4. Feedback Mechanism for the Interpretation Framework

The horizon matching work-flow introduced here (Figure 8.1) should be benefited from a feedback mechanism, where the fault tracking and horizon matching are connected in a feedback loop. In such feedback mechanism, the fault throw estimations obtained from horizon matching would provide information to identify faults in areas of low fault probability. The necessary feedback mechanism and the relationships among fault size, shape and throw distributions should be investigated.

It should be possible to adapt the stochastic modelling strategy employed in this thesis to other image processing problems, in particular for the texture segmentation [145] [174] [111] where modeling of higher order geometric interactions is required. The modification would be to use an appropriate smoothness model instead of the theoretical fault throw model.

9 Conclusions

3D seismic data have been used for hypothesizing sub-surface structures. The interpretation of seismic data is a highly time-consuming task that requires the interpreter to manually ‘pick’ hundreds of fault surfaces, track horizons and match horizons across faults. The correctness of an interpretation can not be ascertained, because the actual geology is rarely known in enough detail. Instead, the test of a good interpretation is consistency with all of the available data.

The thesis investigated and developed a model-based image analysis algorithm for finding the optimal horizon matchings across faults. Within the scope of the thesis work, a semi-automatic fault tracking method was developed.

The major aim of the thesis was to show that the consideration of 3D spatial continuity in the data and a multi-resolution matching approach provide a means for a robust data analysis.

In the thesis, the following six major components have been developed.

1. Fault auto-tracking method
2. Fault throw energy measure
3. Seismic energy measure
4. A semantic scale space for the multi-resolution representation of horizons
5. A stochastic method for automated matching of horizons across faults
6. A framework for automated 3D interpretations at faults.

Each of these components had supported the horizon matching task, and they were combined to achieve the major aim of the thesis. Reviews of the components are given below.

1. **Fault auto-tracking method**

Previous approaches for the automatic fault-surface extraction from 3D seismic data often follow a data-driven strategy with potential fault locations being combined using local continuity constraints. The thesis has developed a semi-automatic fault-tracking approach

which complements these approaches by 1) using a computationally inexpensive alternative to routine fault highlighters (e.g. coherency, semblance) through the use of log-Gabor filters, and 2) applying an active contour to fault tracking that is capable of searching for smooth fault curves in noisy seismic data with partially missing signals. A user interaction was solely required for an approximate fault pick on the first inline, and in cases where the fault line was lost due to an insufficient signal.

The application of the auto-tracker prototype demonstrated that the auto-tracking method provides a fast solution for the mapping of complete 3D fault surfaces of constant orientation.

2. Fault throw energy measure

Fault throw energy encourages matched horizons to have offsets, which agree with a theoretical fault throw function. The theoretical fault throw function assumes an elliptical fault shape and its parameters were estimated empirically from the offsets.

Results showed the appropriateness and the necessity of the fault throw energy measure for robust matching decisions.

3. Seismic energy measure

The seismic energy measures seismic similarities between matching horizons. It was designed with the aim of utilizing the 3D spatial relationship in seismic data. The seismic data was represented as a 3D real-valued field of seismic amplitudes. Horizon geometries were then defined as surfaces through the 3D space, corresponding to ridges of strong local seismic similarities. Seismic features were computed at fault patch locations, and the computation was guided by horizons geometries.

The similarity between horizons was derived as a likelihood measure, which determined if the seismic features of horizons form a Gaussian process with an exponential weighting function. An a-priori smoothness constraint was specified by the exponential weighting function.

The application of the seismic energy was shown for evaluating the reliability of the seismic features. The results of the matching algorithm improved, as the number of slices considered in the matching decisions increased. This showed that seismic energy is capable of exploiting the 3D spatial continuity in the data, and proved that the 3D modeling aspect of the data lead to a more robust data analysis.

4. **A semantic scale space for multi-resolution representation of horizon**

The thesis has introduced a new multi-resolution representation of horizons under a semantic framework. This was done by using a multi-scale function that maps a semantic scale into a likelihood value. The semantic was understood in terms of the likelihood of seismic features observed on horizon surfaces.

Results showed that the multi-resolution extension has improved and facilitated the matching algorithm. They also indicated the potential to perform matchings at a continuous scale (i.e at voxel level).

5. **A stochastic method for automated horizon matching across faults**

The thesis has developed a stochastic horizon matching model and adopted a stochastic annealing scheme to find the optimal matching solution. The stochastic horizon matching model was used to quantify a given matching solution with respect to a density function defined over a marked point process. The density function comprised the fault throw and the seismic energy measures. The optimal matching solution was then selected as the sample that maximizes the density of the stochastic matching model.

Matching samples were generated by using a reversible jump Markov Chain Monte Carlo (RJMC) algorithm. Two additional RJMC state transition moves were introduced in order to facilitate the stochastic annealing algorithm. The stochastic annealing scheme was also extended to handle the multi-scale search.

Results showed that the automated method is capable of performing matchings which compare well with manually obtained matching references. This proved the appropriateness of the stochastic horizon matching model and the stochastic annealing.

6. **A framework for automated 3D interpretation at faults**

This thesis had developed a framework for automated 3D interpretations at fault patch locations. The framework provides the means to extract 3D geometric primitives from seismic data and to manipulate them. The manipulation involves a multi-scale analysis and the construction of geological models. The geological models attempt to describe either the data continuity or the geological continuity (for example, matching across faults). The framework also provides tools to enhance geological attributes of the seismic image, to measure the reliability of data, and to evaluate manual interpretations.

Automated results were obtained in fraction of time, which is necessary for manual interpretations. Therefore, the major objective to facilitate the routine matching task has been

met. The framework tools do not aim to replace the interpreter, rather to reproduce the intuitive work performed by the interpreter. Moreover, the framework provides flexibility for continuously improving interpretation models.

A Extension to Experiment Setup

A prototype software is implemented to demonstrate the application of the thesis interpretation framework. The software has two graphical interfaces: a feature computation interface and a horizon matching interface. The feature computation is used for data loading, fault tracking, horizon tracking and the computation of horizon features. The horizon matching interface is used to load horizon features from each side of the fault, to set stochastic annealing parameters, and to run the annealing algorithm. This appendix explains how the software was utilized to conduct the experiment tests.

A.1 Data Loading and Display

A data set is loaded and displayed in the feature computation GUI (Figure A.1A). By using entries under the file menu, the seismic data set can be loaded and displayed. Three display options are available: inline, cross-line, and time section. Figure A.1B shows the time section view of the Swamp data set loaded in the framework. Fault labels, which are tracked in the data set, are loaded with the data set and displayed in the fault label column. Each label represents a particular fault.

A.2 Fault Tracking and Fault Patch Extraction

The fault tracking procedure can be applied after loading the data set. The fault tracking menu provides entries to specify a seed line, and to start the fault tracking procedure. It also has entries to label, save, and edit tracking results (see Figure A.2A). The tracking procedure navigates through the sequence of fault attribute slices to extract the fault surface. The fault attribute slices should be pre-computed in order to facilitate the tracking procedure. After tracking, faults are given labels and are stored. Later, they can be loaded, edited, or deleted. Separately tracked faults can also be merged. A further smoothing to the fault tracking results can be made by using the FastRBF interpolation tool box, which is available under the Fault surface menu. For

each fault label, a fault patch can be isolated using the options under the Fault patch menu. Every fault patch has two separate volumes for the hanging- and foot-wall blocks.

A.3 Horizon Tracking and Features Computations

A fault patch is loaded by specifying its fault label and block side. Figure A.3A shows a display of inline slice from the footwall block (here it is called left side) of a fault patch. The segments on the lower window are ridge segments identified from the slice shown in the upper window. Figure A.3B shows a cross line display for the same footwall block loaded in Figure A.3A. The display is facing the fault surface, and more appropriately, it is called a fault slice view.

The horizon tracking procedure under the Horizon menu allows to track ridge segments and build horizon surfaces. Ridge segments forming a single horizon surface are given an identical label and are stored (or exported in a separate file). Exported horizons are listed under the Horizon exported column (see Figure A.3B). For each exported horizon, its 3D surface coordinates and associated seismic values are stored. An additional entry in the Horizon Feature menu allows to compute horizon traces, which involve projecting horizon surfaces and computing intersections with the fault surface.

A.4 Horizon Matching

In the horizon matching interface (see Figure A.4), the Horizon menu allows to load horizon features from both fault blocks. The original seismic data set and previously saved experimental data can also be loaded. After loading all horizons, the parameters for the stochastic annealing should be specified in the text boxes on the right side of the window. Then, the stochastic annealing can be run from the Optimization menu. In order to select the appropriate parameters or to conduct additional tests the various entries in the menus can be utilized. The Continuous match menu contains entries to make a continuous scale matching.

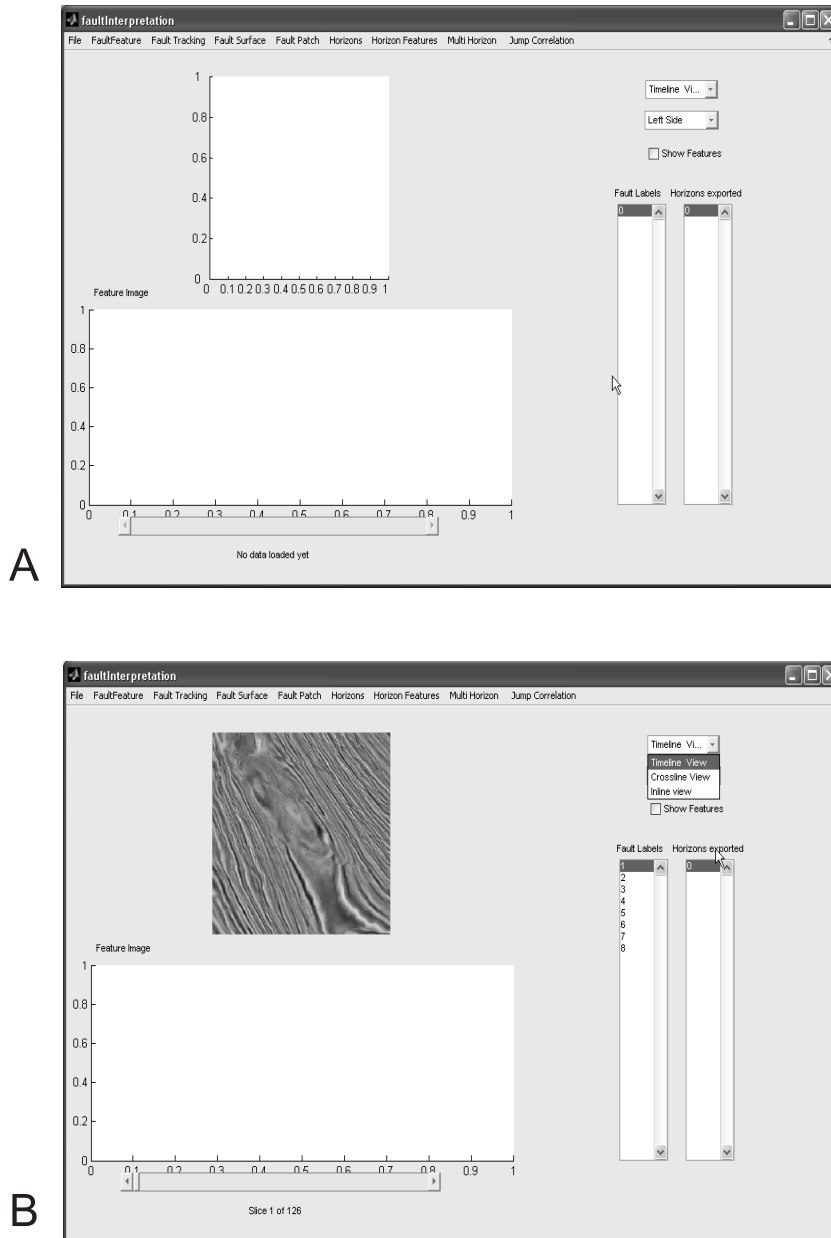


Figure A.1: A. screen shots of the prototype software interface for feature computation. B. seismic data is loaded and displayed in the time section.

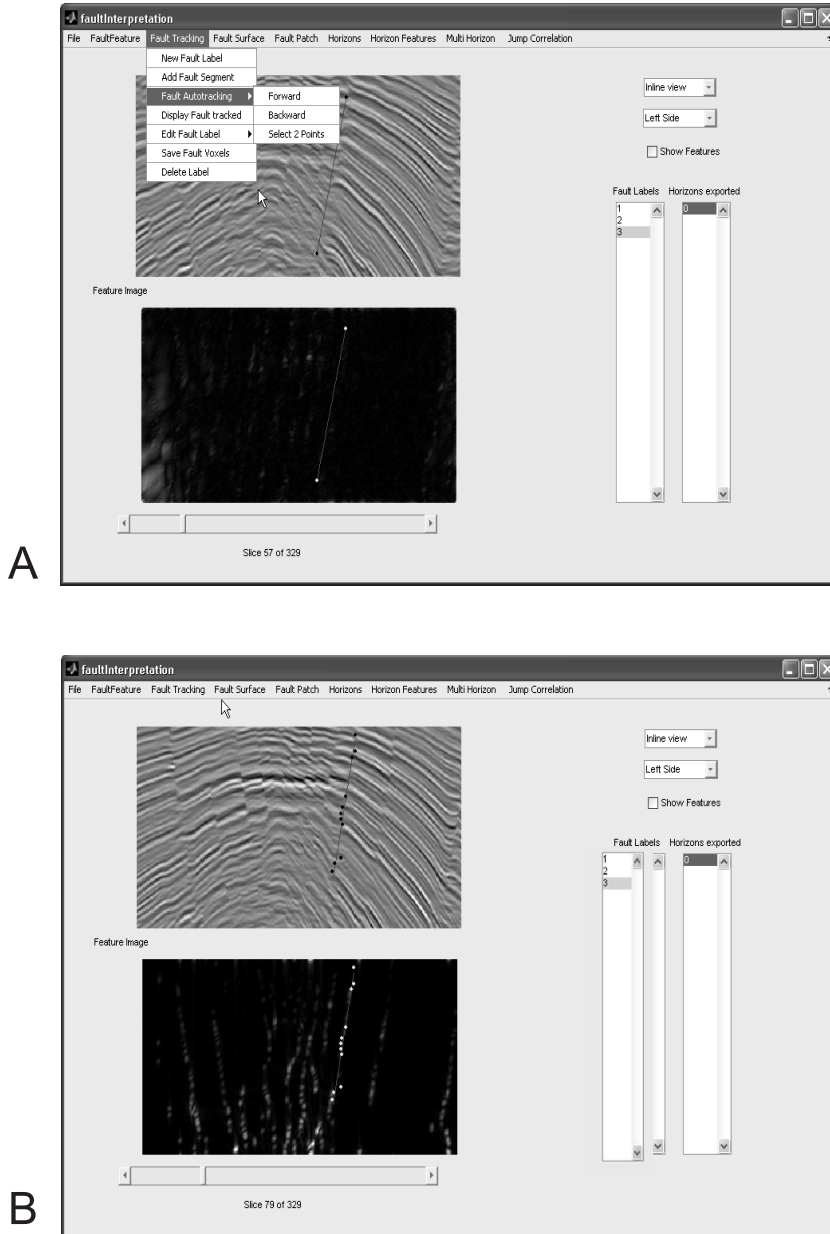


Figure A.2: A. inline slices showing a manually drawn fault line on seismic section (top) and fault attribute (bottom). B. inline slices showing the fault auto-tracking result on seismic section (top) and fault attribute (bottom).

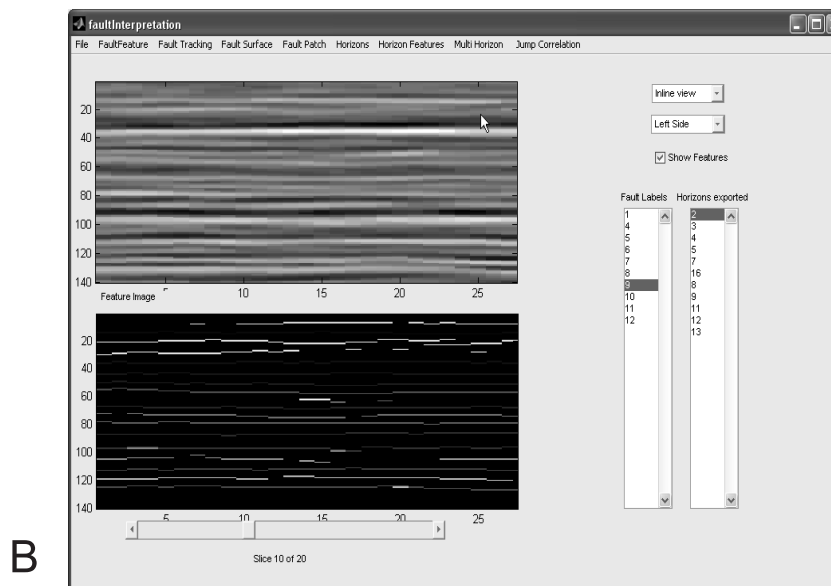
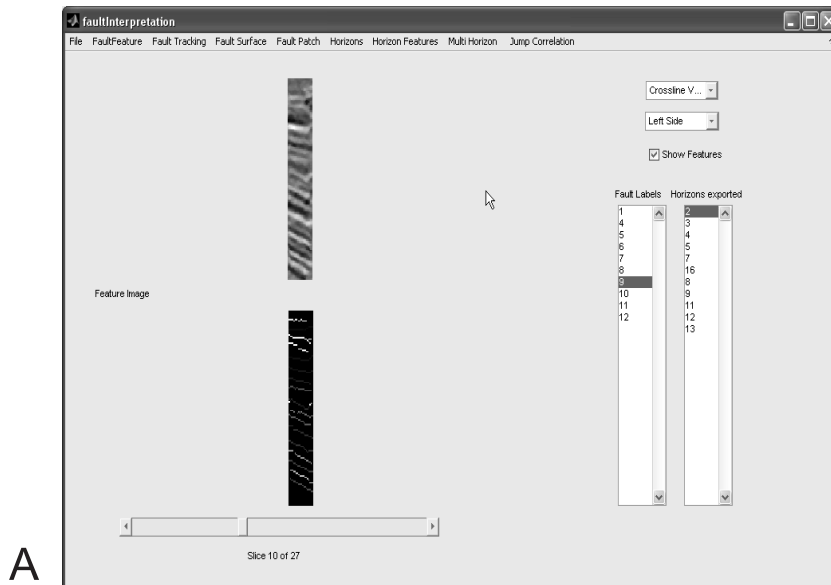


Figure A.3: A. inline slices showing the fault patch seismic section (top) and horizon segments (bottom). The displayed inline seismic section is from the footwall side of the fault. B. cross-line (Fault slice view) slices showing the fault patch seismic section and corresponding horizon segments (bottom).

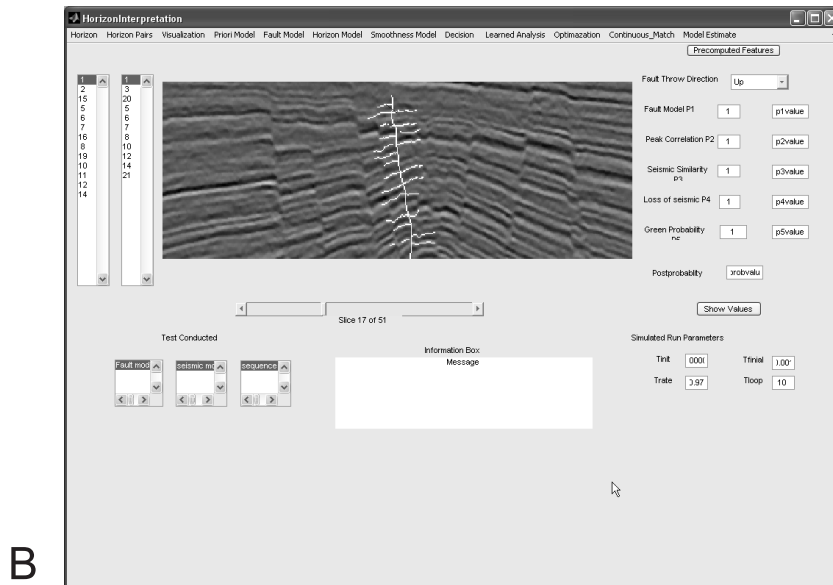
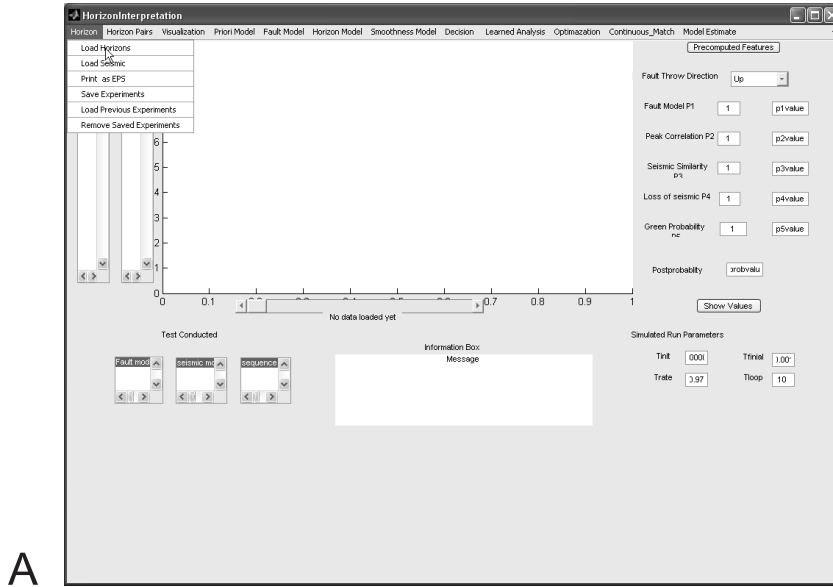


Figure A.4: A. GUI interfaces for horizon matchings. B. display of horizon matching solution.

Bibliography

- [1] P. Abrahamsen, “A review of gaussian random fields and correlation function,” Norwegian Computing Center, Oslo, Norway, Tech. Rep. 917, 1997.
- [2] F. Admasu, S. Back, and K. Toennies, “Auto-tracking of faults on 3d seismic data,” *Journal of Geophysics*, vol. 71, no. 6, pp. A49–A53, 2006.
- [3] F. Admasu and K. Toennies, “Automatic method for correlating horizons across faults in 3d seismic data,” in *Proceedings of the IEEE Computer Society Conference on Computer Vision and Pattern Recognition*, Washington DC, USA, 2004, pp. 114–119.
- [4] —, “A model-based approach to automatic 3d seismic horizons correlations across faults,” in *Simulation und Visualisierung*, 2004, pp. 239–250.
- [5] —, “Anisotropic 3d seismic features for robust horizons correlation across faults,” in *IEEE International Conference on Image Processing (ICIP2005)*, 2005, pp. 225–228.
- [6] —, “An approach towards automated fault interpretations in seismic data,” in *Simulation und Visualisierung*, 2005, pp. 207–220.
- [7] —, “Bayesian based horizon matching across faults in 3d seismic data,” Computer vision group, University of Magdeburg, Tech. Rep. TR-ISGBV-06-01, 2006.
- [8] —, “Exploiting 3d spatial continuity for robust automatic horizon matching across faults,” in *IEEE Third International Symposium on 3D Processing, Visualization and Transmission (3DPVT 2006)*, Chapel Hill, USA, Chapel Hill, USA, 2006, pp. 695–702.
- [9] —, “Multi-scale bayesian based horizon matching across faults in 3d seismic data,” in *28th Annual Symposium of the German Association for Pattern Recognition (DAGM 2006)*, Berlin, Germany, 2006, pp. 384–393.
- [10] F. Admasu, S. Al-Zubi, K. Toennies, N. Bodammer, and H. Hinrichs, “Segmentation of multiple sclerosis lesions from mr brain images using the principles of fuzzy-connectedness and artificial neuron networks,” in *International Conference on Image Processing (ICIP)*, vol. 2, 2003, pp. 1081–1084.

-
- [11] K. Aki and P. Richards, *Quantitative Seismology*. W. H. Freeman and Co., 1980.
- [12] J. Alander, "Indexed bibliography of genetic algorithms in signal and image processing," University of Vaasa, Department of Information Technology and Production Economics, Report 94-1-SIGNAL, 1995.
- [13] E. Alberts, "Horizon mapping in exploration seismology using artificial intelligence," Ph.D. dissertation, Department of Earth Science and Engineering Imperial College of Science, Technology and Medicine University of London, 2002.
- [14] M. Aurnhammer, "Model-based image analysis for automated horizon correlation across faults in seismic data," Ph.D. dissertation, University of Magdeburg, 2003.
- [15] M. Aurnhammer and K. Toennies, "A genetic algorithm for automated horizon correlation across faults in seismic images," *IEEE Transactions on Evolutionary Computation*, vol. 9, no. 2, pp. 201–210, 2005.
- [16] R. Avila-Carrera and F. Sanchez-Sesma, "P- and s-waves modeling for 3d objects by a classical analytic solution," in *73rd SEG Annual International Meeting*. SEG, 2003, pp. 2289–2292.
- [17] S. Back, Institute of Geology, Aachen University, Personal Communication, 2003.
- [18] ———, Institute of Geology, Aachen University, Personal Communication, 2005.
- [19] A. Baddeley and M. V. Lieshout, "Stochastic geometry models in highlevel vision," *Statistics and Images*, vol. 20, pp. 235–256, 1993.
- [20] A. Baddeley, M. Lieshout, and J. Møller, "Markov properties of cluster processes," *Advanced Applied Probability*, vol. 28, pp. 346–355, 1996.
- [21] M. Bahorich and S. Farmer, "3-d seismic discontinuity for faults and stratigraphic features: the coherence cube," *Leading Edge*, vol. 14, no. 10, pp. 1053–1058, October 1995.
- [22] ———, "3d seismic discontinuity for faults and stratigraphic features," *The Leading Edge*, vol. 14, pp. 1053–1058, 1995.
- [23] P. Bakker, "Image structure analysis for seismic interpretation," Ph.D. dissertation, Technical University of Delft, 2002.
- [24] S. Beauchemin and J. Barron, "Computation of optical flow," *ACM Computing Surveys*, vol. 27, no. 3, pp. 433–467, 1995.

- [25] A. Bekkhout, "The seismic method in the search for oil and gas: Current techniques and future developments," *AAPG Explorer:Geophysical Corner*, vol. 74, no. 8, pp. 1133–1159, 1986.
- [26] A. Berkhout, L. Ongkiehong, A. Volker, and G. Blacquire, "Comprehensive assessment of seismic acquisition geometries by focal beams part i and ii," *Geophysics*, vol. 66, pp. 911–917, 2001.
- [27] D. Bevc, "Review over 3d seismic interpretation," *The Leading Edge*, vol. 24, no. 02, p. 211, 2005.
- [28] F. Bosquet and J. Dulac, "Advanced volume visualization new ways to explore, analyze, and interpret seismic data," *The Leading Edge*, vol. 19, no. 5, pp. 535–537, 2000.
- [29] A. Brown, *Interpretation of Three-Dimensional Seismic Data*. American Association of Petroleum Geologists, 1999.
- [30] —, "Pitfalls in 3d seismic interpretation," *The Leading Edge*, vol. 24, no. 7, pp. 716–717, 2005.
- [31] L. Brown, "A survey of image registration techniques," *ACM Computing Surveys*, vol. 24, pp. 325–376, 1992.
- [32] J. Canny, "A computational approach to edge detection," *IEEE Trans. Pattern Analysis and Machine Intelligence*, vol. 8, pp. 679–714, 1986.
- [33] M. Carcassoni and E. Hancock, "A hierarchical framework for modal correspondence matching," in *Proceedings of the 11th International Conference on Image Analysis and Processing (ICIAP 01)*, 2001, pp. 327–332.
- [34] V. Cerny, "Thermodynamical approach to the traveling salesman problem: an efficient simulation algorithm," *Journal of Optimization Theory and Applications*, vol. 45, pp. 41–51, 1985.
- [35] J. Champion, K. Mueller, A. Tate, and M. Guccione, "Geometry, numerical models and revised stiprate for the reelfoot fault and trishear fault propagation fault, new madrid seismic zone," *Engineering Geology*, pp. 31–49, 2001.
- [36] S. Chopra, "Integrating coherence cube imaging and seismic inversion," *The Leading Edge*, vol. 20, pp. 354–362, 2001.
- [37] —, "Coherence cube and beyond," *First break*, vol. 20, no. 1, pp. 27–33, 2002.

- [38] S. Chopra and V. Alexeev, "Application of texture attribute analysis to 3d seismic data," *The Leading Edge*, vol. 25, no. 8, pp. 934–940, 2006.
- [39] S. Chopra, V. Sudhakar, G. Larsen, and H. Leong, "Azimuth based coherence for detecting faults and fractures," *World Oil*, vol. 64, pp. 57–62, 2000.
- [40] J. Claerbout, *Imaging the Earth's Interior*. Oxford, England: Blackwell Scientific Publications, 1985.
- [41] H. Cohn and M. Fielding, "Simulated annealing: searching for an optimal temperature schedule," *Journal of Optimization*, vol. 9, no. 3, pp. 779–802, 1999.
- [42] J. Cook, C. McCool, V. Chandran, and S. Sridharan, "Combined 2d and 3d face recognition using log-gabor templates," in *Proc. of IEEE International Conference on Video and Signal Based Surveillance*, 2006, p. 83.
- [43] N. Cooper, "Acquisition/processing a world of reality - designing land 3d programs for signal, noise, and prestack migration," *The Leading Edge*, vol. 23, no. 12, pp. 1230–1235, 2004.
- [44] A. Cordsen, M. Galibraith, and J. Peirce, *Planning land 3-D Seismic Surveys*. Soc. Expl. Geophysics, 2000.
- [45] T. Cormen, C. Leiserson, R. Rivest, and C. Stein, *Introduction to Algorithms*. MIT Press and McGraw-Hill, 2001.
- [46] L. G. Corporation, "Interpret 2000," <http://www.lgc.com>.
- [47] P. Cowie, R. Knipe, and I. Main, "Scaling laws for fault and fracture populations - analyses and applications," *Journal of Structural Geology special issue, Editors*, vol. 18, no. 2-3, 1996.
- [48] X. Dai and S. Khorram, "A feature-based image registration algorithm using improved chain-code representation combined with invariant moments," *IEEE Transactions on Geoscience and Remote Sensing*, vol. 37, no. 5, pp. 2351–2362, 1999.
- [49] R. Dalley, E. Gevers, G. Stampfli, D. Davies, C. Gastaldi, P. Ruijtenberg, and G. Vermeer, "Dip and azimuth displays for 3d seismic interpretation," *First Break*, vol. 7, no. 3, pp. 86–95, 1989.
- [50] I. Daubechies, *Ten lectures on wavelets*. Society for Industrial and Applied Mathematics, 1992.

- [51] N. Dawers, M. Anders, and C. Schols, "Growth of normal faults: Displacement-length scaling," *Geology*, vol. 21, no. 12, pp. 1107–1110, 1993.
- [52] M. Dorigo, G. Caro, and L. Gambardella, "Ant algorithms for discrete optimization," *Artificial Life*, vol. 5, no. 3, pp. 137–172, 1999.
- [53] G. Dorn, "Modern 3d seismic interpretation," *The Leading Edge*, vol. 17, no. 9, pp. 1262–1273, 1998.
- [54] G. Dorn and H. James, "Automatic extraction of faults and a salt body in a 3-d survey from the eugene island area, gulf of mexico," in *AAPG International Conference and Exhibition Expanded Abstracts*, 2005.
- [55] J. du Buf, "Ramp edges, mach bands, and the functional significance of the simple cell assembly," *Biological Cybernetics*, pp. 449–461, 1994.
- [56] J. du Buf and Heitkamper, "Texture features based on gabor phase," *Signal Processing*, vol. 23, pp. 227–244, 1991.
- [57] J. Eidsvik, P. Avseth, H. Omre, T. Mukerji, and G. Mavko, "Stochastic reservoir characterization using pre-stack seismic data," *Geophysics*, vol. 69, no. 4, pp. 978–993, 2004.
- [58] M. Faraklioti and M. Petrou, "Horizon picking in 3d seismic data volumes," *Machine Vision and Applications*, vol. 15, no. 4, pp. 216–219, 2004.
- [59] C. Farmer, "Geological modelling and reservoir simulation," in *Mathematical Methods and Modeling in Hydrocarbon Exploration and Production*, ser. Mathematics in Industry, A. Iske and T. Randen, Eds. New York, USA: Springer-Verlag, 2005, vol. 7, pp. 119–212.
- [60] ffa Technology, "Svi pro," www.ffa.co.uk, 2007.
- [61] D. Field, "Relations between the statistics of natural images and the response properties of cortical cells," *Journal of the Optical Society of America*, vol. 4, pp. 2379–2394, 1987.
- [62] O. Firschein, "Defense applications of image understanding," *IEEE Expert: Intelligent Systems and Their Applications*, vol. 10, no. 5, pp. 11–17, October 1995.
- [63] S. Forrest, "Genetic algorithms: Principles of natural selection applied to computation," *Science*, pp. 872–878, 1993.
- [64] L.-Y. Fu, "On seismic migration efficiency," *SEG Expanded Abstracts*, vol. 22, p. 1071, 2003.

- [65] A. Gersztenkorn and K. Marfurt, "Eigenstructure-based coherence computations as an aid to 3d structural and stratigraphic mapping," *Geophysics*, vol. 64, pp. 1468–1479, 1999.
- [66] D. Gibson, M. Spann, and J. Turner, "Automatic fault detection for 3d seismic data," in *Proceedings of Digital Image Computing - Techniques and Applications Conference (DICTA 2003) Expanded Abstracts*, 2003, pp. 821–830.
- [67] J. Gibson, *The Perception of the Visual World*. Houghton Mifflin, 1955.
- [68] R. Godfrey, F. Muir, and F. Rocca, "Modelling seismic impedance with markov chains," *Geophysics*, vol. 45, no. 8, pp. 1351–1372, 1980.
- [69] J. Goff and T. Jordan, "Stochastic modeling of seafloor morphology: Inversion of sea beam data for second-order statistics," *Journal of Geophysical Research*, vol. 93, no. 13, pp. 589–608, 1988.
- [70] D. Goldberg, *Genetic Algorithms in Search, Optimization, and Machine Learning*. Addison-Wesley, 1989.
- [71] R. Gonzalez and R. Safabakhsh, "Computer vision techniques for industrial applications and robot control," *Computer*, vol. 15, no. 12, pp. 17–33, December 1982.
- [72] J. Grandell, "Point processes and random measures," *Advances in Applied Probability*, vol. 9, no. 3, pp. 502–526, 1977.
- [73] P. Green, "Reversible jump markov chain monte carlo computation and bayesian model determination," *Biometrika*, vol. 57, no. 82, pp. 97–109, 1995.
- [74] P. Green, N. Hjort, and S. Richardson, *Highly Structured Stochastic Systems*. Oxford University Press, 2003.
- [75] S. Grigorescu, N. Petkov, and P. Kruizinga, "Comparison of texture features based on gabor filters," *IEEE Transactions On Image Processing*, vol. 11, no. 10, pp. 1160–1167, 2002.
- [76] A. Guerreroa and L. Smith, "A maximum likelihood estimator for long-range persistence," *Physica A*, vol. 355, no. 1, pp. 619–632, 2005.
- [77] A. Gupta and C. Scholz, "A model of normal fault interaction based on observations and theory," *Journal of Structural Geology*, vol. 22, pp. 865–879, 2000.
- [78] M. Hargrave, A. Deighan, and J. Haynes, "What are interpreters for? -the impact of faster and more objective interpretation systems," Presentation at PESGB Geophysical Technology Conference, London, December 2003.

- [79] M. Hayat and J. Gubner, "A two-step markov point process," in *IEEE International Symposium on Information Theory*, September 1995, pp. 421–.
- [80] D. Herron, "Horizon autopicking," *Journal of Geophysical Research*, vol. 19, pp. 491–492, 2000.
- [81] A. Hill, C. Taylor, and A. Brett, "A framework for automatic landmark identification using a new method of nonrigid correspondence," *IEEE Transactions on Pattern Analysis and Machine Intelligence*, vol. 22, no. 3, pp. 241–251, 2000.
- [82] D. Hill and D. Hawkes, "Medical image registration using knowledge of adjacency of anatomical structures," *Image and Vision Computing*, vol. 12, no. 3, pp. 173–178, April 1994.
- [83] C. Hocker, SHELL, Personal Communication, 2003.
- [84] C. Hocker and G. Fehmers, "Fast structural interpretation with srtructure-oriented filtering," *The Leading Edge*, vol. 21, no. 1, pp. 238–243, 2002.
- [85] K. Hoffmann and P. Salamon, "The optimal simulated annealing schedule for a simple model," *J. Phys. A: Math. Gen.*, vol. 23, no. 7, pp. 3511–3523, 1990.
- [86] N. Honda and S. Aida, "Analysis of multivariate medical data by face method," *Pattern Recognition*, vol. 15, no. 3, pp. 231–242, 1982.
- [87] B. Horn and B. Schunck, "Determining optical flow: A retrospective," *Artificial Intelligence*, vol. 59, no. 1-2, pp. 81–87, 1993.
- [88] R. Horst and P. Pardalos, *Handbook of Global Optimization*. Editors, Kluwer, 1995, vol. I and II.
- [89] S. Houlding, *Practical Geostatistics. Modeling and Spatial Analysis*. Springer Verlag, 2000.
- [90] T. Ian, "Quantitative microscopy," *IEEE Engineering in Medicine and Biology*, vol. 15, no. 1, pp. 59–66, 1996.
- [91] S. M.-T. Inc., "The kingdom suite," <http://www.seismicmicro.com>.
- [92] H. Inoue, "Vision-based robotics: A challenge to real-world artificial-intelligence," *Advanced Robotics*, vol. 9, no. 4, pp. 351–366, 1995.
- [93] F. Jensen, *Bayesian Networks and Decision Graphs*. Springer, 2001.

- [94] J. Jensen, *Digital Image Processing: a Remote Sensing Perspective*, 3rd ed. Prentice Hall, 2005.
- [95] J. Robertson and D. Fisher, "Complex seismic trace attributes," *The Leading Edge*, vol. 7, no. 6, pp. 22–26, 1988.
- [96] R. Kalman, "A new approach to linear filtering and prediction problems," *Transactions of the ASME - Journal of Basic Engineering*, vol. 82, pp. 35–45, 1960.
- [97] M. Kass, A. Witkin, and D. Terzopolous, "Snakes: Active contour models," *International Journal of Computer Vision*, vol. 1, pp. 321–331, 1987.
- [98] Y. Kim, D. Peacock, and D. Sanderson, "Fault damage zones." *Journal of Structural Geology*, vol. 26, no. 3, pp. 503–517, 2004.
- [99] S. Kirkpatrick, C. Gelatt, and M. Vecchi, "Optimization by simulated annealing," *Science*, vol. 220, pp. 671–681, 1983.
- [100] P. Kovesi, "Image features from phase congruency," *Journal of Computer Vision Research. MIT Press.*, vol. 1, no. 1, 1999.
- [101] J. Lachaud and A. Montanvert, "Digital surfaces as a basis for building isosurfaces," in *Proceedings of International Conference on Image Processing*, vol. 2, 1998, pp. 977–97.
- [102] C. Lacoste, X. Descombes, and J. Zerubia, "Point processes for unsupervised line network extraction in remote sensing," *IEEE Trans. Pattern Analysis and Machine Intelligence*, vol. 27, no. 10, pp. 1568–1579, 2005.
- [103] M. Lane, "An implementation of 3-d seismic binning," *CREWES Research Report*, vol. 6, no. 24, pp. 1–5, 1994.
- [104] H. Lester and S. Arridge, "A survey of hierarchical non-linear medical image registration," *Pattern Recognition*, vol. 32, pp. 129–149, 1999.
- [105] T. Lindeberg, *Scale-Space Theory In Computer Vision*. Kluwer Academic Publishers, 1994.
- [106] X. Liu, P. Yue, and L. Li, "Self organising neural networks for picking seismic horizons," *SEG Technical Program Expanded Abstracts*, vol. 9, no. 1, p. 313, 1990.
- [107] B. Lucas and T. Kanade, "An iterative image registration technique with an application to stereo vision," in *Proceedings of Imaging Understanding Workshop*, 1981, pp. 121–130.

- [108] Y. Luo, S. al Dossary, and M. Alfaraj, "Edge preserving smoothing and applications," *The Leading Edge*, vol. 21, pp. 136–158, 2002.
- [109] Y. Luo, W. Higgs, and W. Kowalik, "Edge detection and stratigraphic analysis using 3-d seismic data," *66th Annual International Meetings, SEG Expanded Abstract*, pp. 324–327, 1996.
- [110] Y. Luo, Y. Wang, N. AlBinHassan, and M. Alfaraj, "Computation of dips and azimuths with weighted structural tensor approach," *Geophysics*, vol. 71, no. 5, pp. 119–121, 2006.
- [111] J. Malik, S. Belongie, T. Leung, and J. Shi, "Contour and texture analysis for image segmentation," *International Journal of Computer Vision*, vol. 43, no. 1, pp. 7–27, 2001.
- [112] S. Mallat, "A theory for multiresolution signal decomposition: the wavelet representation," *IEEE Transactions on Pattern Analysis and Machine Intelligence*, vol. 2, no. 7, pp. 606–615, 1989.
- [113] C. Mancas-Thillou and B. Gosselin, "Character segmentation-by-recognition using log-gabor filters," in *Proc. of IAPR International conference on Pattern Recognition*, vol. 2, 2006, pp. 901–904.
- [114] K. Marfurt, "Robust estimates of 3d reflector dip and azimuth," *Geophysics*, vol. 71, no. 4, pp. 29–40, 2006.
- [115] K. Marfurt, R. Kirlin, S. Farmer, and M. Bahorich, "3d seismic attributes using a semblance-based coherency algorithm," *Geophysics*, vol. 63, pp. 1150–1165, 1998.
- [116] K. Marfurt, V. Sudhakar, N. Gersztenkorn, K. Crawford, and S. Nissen, "Coherency calculations in the presence of structural dip," *Geophysics*, vol. 64, pp. 104–111, 1999.
- [117] G. Markovich, M. Skolnick, and M. Core, "A new methodology for isolating and diagnosing inconsistencies in image matching, as applied to the analysis of 2-d electrophoretic gels," in *Proceedings IEEE Workshop on Applications of Computer Vision*, 1992, pp. 197–204.
- [118] R. Martinez, "Reflection on seismic exploration," *CSEG Recorder*, vol. 45, pp. 42–45, 2006.
- [119] E. McAllister, R. Smallshire, R. Knipe, and P. Kaufman, "Geometry of fault damage zones from high resolution mapping of the moab fault zone," in *Quantitative Outcrop Data for Reservoir Simulation Applications. Annual Meeting AAPG*, 2000.

- [120] M. McCormack, "Seismic trace editing and firstbreak picking," in *Expanded Abstracts of the 60th SEG Annual Meetings*. SEG, 1990, p. 321–324.
- [121] R. Mcquillin, M. Bacon, and W. Barclay, *An Introduction to Seismic Interpretation: Reflection Seismics in Petroleum Exploration*. Butterworth-Heinemann, 1985.
- [122] D. A. Michael Fehler, Lianjie Huang and H. Sun, "Earth imaging using seismic migration," *The Journal of the Acoustical Society of America*, vol. 112, no. 5, pp. 2389–2389, 2002.
- [123] J. Møller, "On the rate of convergence of spatial birth-and-death processes," *Journal Annals of the Institute of Statistical Mathematics*, vol. 41, no. 3, pp. 565–581, 1989.
- [124] J. Møller and R. Waagepetersen, *Statistical Inference and Simulation for Spatial Point Processes*. CRC Press, 2003.
- [125] E. Monser, T. Randen, L. Sonneland, and J. Odegard, "Geological model building: A hierarchical segmentation approach," in *Mathematical Methods and Modeling in Hydrocarbon Exploration and Production*, ser. Mathematics in Industry, A. Iske and T. Randen, Eds. New York, NY, USA: Springer-Verlag, 2005, vol. 7, pp. 213–246.
- [126] I. Mufti, "Seismic migration; basic concepts and popular methods, part 2," *Geophysics: The Leading Edge of Exploration*, vol. 4, no. 9, pp. 54–58, 1985.
- [127] V. Murino and A. Trucco, "Underwater computer vision and pattern recognition," *Computer Vision and Image Understanding*, vol. 79, no. 1, pp. 1–3, July 2000.
- [128] J. Musser, "3d seismic survey design: a solution," *First break*, vol. 18, pp. 166–171, 2000.
- [129] I. Ng, J. Kittler, M. Petrou, and E. Hancock, "Robust approach to seismic horizon picking," *International Conference on Image Processing and its Applications*, vol. 1, no. 1, pp. 506–509, 1992.
- [130] C. Oddy and A. Rye, "Segmentation of sar images using a local similarity rule," *Pattern Recognition Letters*, vol. 1, pp. 443–449, 1983.
- [131] F. Odone, E. Trucco, and A. Verr, "A flexible algorithm for image matching," in *Proceedings of the 11th International Conference on Image Analysis and Processing (ICIAP 01)*, 2001, pp. 290–295.
- [132] M. Ortner, X. Descombes, and J. Zerubia, "A gibbs point process for road extraction from remotely sensed images," *International Journal of Computer Vision*, vol. 57, no. 2, pp. 121–136, 2004.

- [133] ———, “Building outline extraction from digital elevation models using marked point processes,” *International Journal of Computer Vision*, vol. 72, no. 2, pp. 107–132, 2007.
- [134] D. Peacock, “Propagation, interaction and linkage in normal fault system,” *Earth-Science Review*, vol. 58, pp. 121–142, 2002.
- [135] D. Peacock and D. Sanderson, “Effects of propagation rate on displacement variations along faults,” *Journal of structural geology*, vol. 18, no. 2/3, pp. 311–320, 1996.
- [136] S. Pedersen, T. Randen, L. Sonneland, and O. Steen, “Automatic fault extraction using artificial ants,” *72nd Annual International Meeting, SEG, Expanded Abstracts*, vol. 21, pp. 512–515, 2002.
- [137] S. Pedersen, T. Skov, A. Hetlelid, P. Fayemendy, T. Randen, and L. Sonneland, “New paradigm of fault interpretation,” *SEG Technical Program Expanded Abstracts*, vol. 22, pp. 350–353, 2003.
- [138] J. Pinter, *Global Optimization in Action*. Kluwer, 1995.
- [139] M. Porsania and B. Ursinb, “Deconvolution and wavelet estimation by using a genetic algorithm,” *SEG Technical Program Expanded Abstracts*, vol. 19, no. 1, pp. 2185–2188, 2000.
- [140] ———, “Mixed-phase deconvolution and wavelet estimation,” *The Leading Edge*, vol. 19, no. 1, pp. 76–79, 2000.
- [141] R. Postma, “Pre-stack can avoid distortions,” *presentation Geophysical Corner, AAPG Explorer*, September 1997.
- [142] T. Randen, S. Petersen, and L. Sonneland, “Automatic extraction of fault surfaces from three-dimensional seismic data,” *71th Annual International meeting, SEG, Expanded Abstracts*, pp. 551–554, 2001.
- [143] T. Randen and L. Sonneland, “Atlas of 3d seismic texture,” in *Mathematical Methods and Modeling in Hydrocarbon Exploration and Production*, ser. Mathematics in Industry, A. Iske and T. Randen, Eds. New York, USA: Springer-Verlag, 2005, vol. 7, pp. 23–46.
- [144] C. Rasmussen and C. Williams, *Gaussian Processes for Machine Learning*. Massachusetts Institute of Technology, 2006.
- [145] T. Reed and J. du Buf, “A review of recent texture segmentation and feature extraction techniques,” *CVGIP - Image Understanding*, vol. 57, no. 3, pp. 359–372, 1993.

- [146] B. Rieger, F. Timmermans, L. van Vliet, and P. Verbeek, "On curvature estimation of iso surfaces in 3d gray-value images and the computation of shape descriptors," *IEEE Transactions on Pattern Analysis and Machine Intelligence*, vol. 26, no. 8, pp. 1088–1094, 2004.
- [147] C. Robert and G. Casella, *Monte Carlo Statistical Methods*. Springer Verlag, 1999.
- [148] H. Rue and M. Hurn, "Bayesian object identification," *Biometrika*, vol. 86, no. 3, pp. 649–660, 1999.
- [149] J. Scales, *Theory of Seismic Imaging*. Samizdat Press, 1997.
- [150] D. Scharstein, R. Szeliski, and R. Zabih, "A taxonomy and evaluation of dense two-frame stereo correspondence algorithms." in *Proceedings of the IEEE Workshop on Stereo and Multi-Baseline Vision*, 2001.
- [151] D. Schenck, "Shared earth model project," Presented at: Information Technology in Oil & Gas E&P Conference, 1998.
- [152] J. Schlaf, T. Randen, and L. Sonneland, "Introduction to seismic texture," in *Mathematical Methods and Modeling in Hydrocarbon Exploration and Production*, ser. Mathematics in Industry, A. Iske and T. Randen, Eds. New York, USA: Springer-Verlag, 2005, vol. 7, pp. 3–21.
- [153] Schlumberger, "Schlumberger oilfield glossary," <http://www.glossary.oilfield.slb.com/>, 2006.
- [154] SEG, "Journal of geophysics," Society of Exploration Geophysicists, 2006.
- [155] R. Sheriff and L. Geldart, *Exploration Seismology*, 2nd ed. Cambridge University Press, 1995.
- [156] R. Simm and T. Redshaw, *3-D Seismic Interpretation*. Cambridge University Press, 2003.
- [157] R. Singh, M. Vatsa, and A. Noore, "Textural feature based face recognition for single training images," *Electronics Letters*, vol. 41, no. 11, pp. 640–641, 2005.
- [158] R. Spitzer, F. Nitsche, A. Green, and H. Horstmeyer, "3-d high resolution surveying: Efficient acquisition concepts and advanced processing strategy," *Geophysics*, vol. 68, no. 1, pp. 1792–1806, 2003.

- [159] R. Sprengel, K. Rohr, and H. Stiehl, "Thin-plate spline approximation for image registration," in *International Conf. of the IEEE Engineering in Medicine and Biology Society*, vol. 3, 1996, pp. 1190–1191.
- [160] S. Stewart, "Displacement distributions on extensional faults: Implications for fault stretch, linkage, and seal," *AAPG Bulletin*, vol. 85, no. 4, pp. 587–599, 2001.
- [161] R. Stoica and E. Gay, "Cluster detection in spatial data using marked point processes," Unite de Biometrie Institut National de la Recherche Agronomique, Tolosan, France, Tech. Rep. 11, 2005.
- [162] D. Stone, *Designing Seismic Surveys in two and three dimensions*. Soc. Expl. Geophysics, 1994.
- [163] D. Stoyan, W. Kendall, and J. Mecke, *Stochastic Geometry and its applications*. John Wiley & Sons, 1987, vol. 2.
- [164] T. Stuetzle and H. Hoosb, "Maxmin ant system," *Journal of Future Generation Computer Systems*, vol. 16, no. 1, pp. 889–914, 2000.
- [165] C. T. T. Cootes, "Statistical models of appearance for medical image analysis and computer vision," *SPIE Proc. Medical Imaging:Image Processing*, vol. 4322, pp. 236–248, 2001.
- [166] M. Taner, F. Koehler, and R. Sheriff, "Complex seismic trace analysis," *Geophysics*, vol. 44, no. 6, pp. 1041–1063, 1979.
- [167] M. Taner and R. Sheriff, "Application of amplitude, frequency, and other attributes to stratigraphic and hydrocarbon determination," in *Applications to hydrocarbon exploration, American Association of Petroleum Geologists*, Tulsa, 1977, pp. 301–327.
- [168] J. Terken and J. Jauffred, "The "faultworld" approach: A semi-automatic fault interpretation workflow," in *AAPG International Conference and Exhibition Expanded Abstracts*, 2005.
- [169] J. Thurston and R. Stewart, "What drives innovation in the upstream hydro-carbon industry?" *The Leading Edge*, vol. 24, no. 11, pp. 1110–1116, 2005.
- [170] K. Tingdahl and M. de Rooij, "Semi-automatic detection of faults in 3d seismic data," *Geophysical Prospecting*, vol. 53, pp. 533–542, 2005.

- [171] K. Tingdahl, O. Steen, P. Meldahl, and J. Ligtenberg, "Semi-automatic detection of faults in 3d seismic signals," *71st Annual International Meeting, SEG, Expanded Abstracts*, pp. 1953–1956, 2001.
- [172] A. Toern and A. Zilinskas, *Global Optimization (Lecture Notes in Computer Science)*. Springer-Verlag, 1989.
- [173] S. Treitel and E. Robinson, "Seismic wave propagation in layered media in terms of communication theory," *Geophysics*, vol. 31, no. 1, pp. 17–32, 1966.
- [174] M. Tuceryan and A. Jain, *The Handbook of Pattern Recognition and Computer Vision*, 2nd ed. World Scientific Publishing Co., 1998, ch. Texture analysis, pp. 207–248.
- [175] R. Twiss and E. Moores, *Structural Geology*. WH Freeman, 1992.
- [176] M. van Lieshout, "Stochastic annealing for nearest-neighbour point processes with application to object recognition," Center for Mathematics and Computer Science, Amsterdam, The Netherlands, Research Report BS-R9306, 1993.
- [177] N. van Lieshout a and R. Stoica, "Markovianity in space and time," *Institute of Mathematical Statistics (IMS) Lecture Notes–Monograph Series*, vol. 48, no. 1, pp. 154–168, 2006.
- [178] E. van Veldhuizen, G. Blacquire, and A. Volker, "Analyzing the effect of seismic acquisition geometries on image quality," in *Proceedings of the Seventh European Conference on Underwater Acoustics, ECUA 2004*, no. 219, Delft, The Netherlands, 2004.
- [179] G. Vermeer, "Seismic data acquisition development in the last decade and in the next- a biased view," *Canadian Society of Exploration Geophysicists (CSEG) Recorder*, vol. 10, pp. 13–16, 2001.
- [180] ———, "3d seismic survey design optimization," *The Leading Edge*, vol. 22, pp. 934–941, 2003.
- [181] J. Walsh and J. Watterson, "Analysis of the relationship between displacements and dimensions of faults," *Journal of Structural Geology*, vol. 10, pp. 239–247, 1988.
- [182] J. Walsh and J. Watterson, "Distributions of cumulative displacement and seismic slip on a single normal fault surface," *Journal of Structural Geology*, vol. 9, no. 8, pp. 1039–1046, 1987.
- [183] Y. Wang, "Inverse q-filter for seismic resolution enhancement," *Geophysics: The Leading Edge of Exploration*, vol. 71, no. 3, pp. V51–V60, 2006.

- [184] E. Weisstein, "P-wave," 2007, [Online; accessed 15-October-2007]. [Online]. Available: <http://scienceworld.wolfram.com/physics/P-Wave.html>
- [185] T. Weldon, W. Higgins, and D. Dunn, "Gabor filter design for multiple texture segmentation," *Optical Engineering*, vol. 35, no. 10, pp. 2852–2863, 1996.
- [186] J. White and D. Ebrom, *Seismic wave propagation: collected works of J. E. White*. Editors, Society of Exploration Geophysicists (SEG), 2000.
- [187] Z. Xiao and Z. Houb, "Phase based feature detector consistent with human visual system characteristics," *Pattern Recognition Letters*, vol. 25, no. 10, pp. 1115–1121, 2004.
- [188] P. Yao, J. Li, X. Ye, Z. Zhuang, and B. Li, "Iris recognition algorithm using modified log-gabor filters," in *International Conference on Pattern Recognition (ICPR'06)*, 2006, pp. 461–464.
- [189] O. Yilmaz, "Applied seismic inversion for estimating earth models in depth," *SEG Technical Program Expanded Abstracts*, vol. 6, no. 1, p. 682, 1996.
- [190] J. Yu, J. Hu, G. Schuster, and R. Estill, "Prestack migration deconvolution," *Geophysics*, vol. 71, no. 2, pp. 53–S62, 2006.
- [191] B. Zhang, S. Shan, X. Chen, and W. Gao, "Histogram of gabor phase patterns (hgpp): A novel object representation approach for face recognition," *IEEE Transactions on Image Processing*, vol. 16, no. 1, pp. 57–68, 2007.
- [192] B. Zitova and J. Flusser, "Image registration methods: a survey." *SIAM Journal on Applied Mathematics*, vol. 21, no. 11, pp. 977–1000, 2003.